Growth of Molybdenum Disulfide (MoS_2) Nanostructures and their Applications

Thesis

Submitted to

Delhi Technological University

in partial fulfilment for the requirements for the degree of

DOCTOR OF PHILOSOPHY

in

APPLIED PHYSICS

by

Prateek Sharma

(Reg. No. 2K17/Ph.D./AP/02)

Under the Supervision

of

Dr. Mohan Singh Mehata

DEPARTMENT OF APPLIED PHYSICS
DELHI TECHNOLOGICAL UNIVERSITY
DELHI-110 042, INDIA

OCTOBER-2021

Dedicated to my beloved family

DECLARATION

I would like to declare that the Ph.D. thesis entitled **"*Growth of molybdenum disulfide (MoS_2) nanostructures and their applications*"** submitted to Delhi Technological University (DTU) for the award of the degree of **"Doctor of Philosophy"** in Applied Physics is a record of bonafide work carried out by me under the guidance and supervision of Dr. Mohan Singh Mehata at Laser-Spectroscopy Laboratory, Department of Applied Physics, DTU and has fulfilled the requirements for the submission of this thesis. The results contained in this thesis are original and have not been submitted to any other University/Institutions for the award of any degree or diploma.

Prateek Sharma
Research Scholar
(Reg. No. 2K17/Ph.D./AP/02)

Date: **18/11/2021**
Place: **Delhi**

Delhi Technological University

Formerly Delhi College of Engineering

(Under Delhi Act 6 of 2009, Govt. of NCT of Delhi)

Shahbad Daulatpur, Bawana Road, Delhi-110042

CERTIFICATE

This is to certify that the Ph.D. thesis entitled **"*Growth of molybdenum disulfide (MoS_2) nanostructures and their applications*"** submitted to Delhi Technological University (DTU) for the award of the degree of **"Doctor of Philosophy"** in Applied Physics is a record of bonafide work carried out by **Mr. Prateek Sharma** under my supervision at Laser-Spectroscopy Laboratory, Department of Applied Physics, DTU and has fulfilled the requirements for the submission of this thesis. The results contained in this thesis are original and have not been submitted to any other University/Institutions for the award of any degree or diploma.

Dr. Mohan Singh Mehata
(Supervisor)
Assistant Professor
Department of Applied Physics
Delhi Technological University
Delhi, India

Submitted Through:

Prof. Rinku Sharma
Head of the Department
Department of Applied Physics
Delhi Technological University
Delhi, India

ACKNOWLEDGEMENTS

The journey of my research is accomplished with the valuable support of many people. It is a pleasant aspect that I have now the opportunity to express my gratitude for all of them.

At the outset, I would like to my profound sense of gratitude, indebtedness and reverence to my supervisor, ***Dr. Mohan Singh Mehata****, Department of Applied Physics, Delhi Technological University, Delhi, who nurtured my research capabilities for a successful scientific career. It has been an honour to work under excellent, enthusiastic and distinguished supervisors. Their unremitting encouragement, constant help, meticulous supervision and constructive criticism throughout the course of my study for carving another milestone in my academic journey. Their immense knowledge of the subject, analytic gaze, farsightedness and perseverance were a constant source of inspiration during the course of this thesis work.*

I feel privileged to have worked under such a great supervision. I further stand ovated to ***Prof. Rinku Sharma****, Head, Department of Applied Physics, DTU, for her valuable help and suggestions. My heartfelt recognitions for* ***Prof. S.C. Sharma****, DRC Chairman, former Head Department of Applied Physics, DTU, my SRC & DRC committee members for their enduring support and appropriate propositions. I express my sincere gratitude especially to* ***Late Prof. Vinay Gupta****, University of Delhi,* ***Prof. R. K. Soni****, Indian Institute of Technology (IIT) Delhi, and* ***Dr. Amrish Panwar****, DTU for their timely advice and support as SRC members.*

I express my sincere gratitude to ***Prof. Ram Singh*** *(Applied Chemistry, DTU) for availing the lab equipment. It is my pleasure to express my sincere thanks to all the faculty members of Department of Applied Physics, DTU for their continuous encouragement and help*

during my research work. I am also grateful technical and non-technical staff for their timely support and cooperation whenever required.

I sincerely thank my dear former and present lab-mates whose support helped in accomplishing my work. It is my pleasure to thank my seniors ***Dr. Ratneshwar Kr. Ratnesh****,* ***Dr. Mrityunjay Kr. Singh*** *and present labmates* ***Mr. Vijay Singh Meena****,* ***Mr. Vineet Sharma****,* ***Ms. Aneesha, Mr. Aaryan, Ms. Namrata*** *for their support. I would also like to thank all the other research scholars of Department of Applied Physics, Delhi Technological University, Delhi for their help and advice. I wish to acknowledge the enjoyable company and suitable help rendered by my dear friends****, Mr. Mukesh Kr. Sahu, Dr. Shankar Subramanian, Ms. Suman Dahiya, Ms. Ritika Khatri, Ms. Ritika Ranga, Ms. Pooja Rohilla, Ms. Shivangi Rajput, Mr. Abhishek Bhardwaj, Mr. Mohit Tyagi, Mr. Uday Veer Singh, Ms. Poonam Dagar, Deepak Kumar (M. Tech.)*** *and other well-wishers for their help and support during this tenure.*

Finally, I thank my family for their support and motivation, every moment of my research period. With heartful gratitude and love, I express my gratefulness to my father ***Mr. Shyam Sunder Sharma****, mother* ***Mrs. Gayatri Sharma*** *for their continual love and encouragement over the entire course of my life. I am thankful to my sister* ***Madhuri Sharma*** *for the valuable suggestions, care, love and having faith in me throughout my existence. I am also thankful to my sweet loving niece* ***Tisha*** *for continuous encouragement. I am thankful to my extended maternal and paternal family for helping me maintain a positive attitude throughout my studies. I always thankful to all my beloved friends across the globe for sharing my happiness and sorrow.*

I gratefully acknowledge the financial assistance provided by Delhi Technological University in the form of Junior Research Fellowship and Senior Research Fellowship during the period of my research. I extend my gratitude to Delhi Technological University and staff in Administration, Accounts, Store & Purchase, Library and Computer Centre for their help and services.

I thank one and all for helping me accomplish the successful realization of the thesis. Thank you all!!!

Prateek Sharma

List of Publications

1. **Prateek Sharma** and Mohan Singh Mehata, Colloidal MoS_2 quantum dots based optical sensor for detection of 2,4,6-TNP explosive in an aqueous medium, ***Optical Materials, 100 (2020) 109646***.

2. **Prateek Sharma** and Mohan Singh Mehata, Rapid sensing of lead metal ions in an aqueous medium by MoS_2 quantum dots fluorescence turn-off, ***Materials Research Bulletin 131 (2020) 110978***.

3. **Prateek Sharma**, Mrityunjay Kumar Singh and Mohan Singh Mehata, Sunlight-driven MoS_2 nanosheets mediated degradation of dye (crystal violet) for the wastewater treatment, ***Journal of Molecular Structure 1249 (2022) 131651***.

4. Mohan Singh Mehata, Mrityunjay Kumar Singh, Kamlesh Awasthi, **Prateek Sharma,** Shailesh Rana and Nobuhiro Ohta, Temperature-dependent electric field induced optical transitions of 2D-molybdenum disulfide (MoS_2) thin films: temperature-dependent electroabsorption and absorption, ***The Journal of Physical Chemistry: C (2021)* (*Accepted*).**

Publications in conference/workshop proceeding

1. **Prateek Sharma** and Mohan Singh Mehata, "Facile synthesis of MoS_2 nanosheets via a sol-gel method with chelating reagent and its optical performance" presented at "DAE-BRNS National Laser Symposium (NLS-27)" held on 03-06, December, 2018, at RRCAT, Indore.

2. **Prateek Sharma** and Mohan Singh Mehata, "Facile synthesis of semiconducting MoS_2 nanosheets via chelation assisted sol-gel method: Optical and electronic properties" presented at "International Conference on Recent Advances in Interdisciplinary Sciences" held on 11-12 January 2019, Jammu.

3. **Prateek Sharma** and Mohan Singh Mehata, "Synthesis of layered MoS_2 nanosheets for enhanced photodegradation of Methyl Blue" presented at "International Conference on Atomic, molecular, optical and nano physics with applications" held on 18-20, December, 2019, DTU, Delhi.

4. **Prateek Sharma** and Mohan Singh Mehata, "Synthesis of nitrogen doped MoS_2 quantum dots and detection of H_2O_2 in water" presented at "Trombay Symposium on Radiation & Photochemistry" held on 05-09 January 2020 at BARC, Mumbai.

CONTENTS

List of figures

List of Tables

CHAPTER 1

Introduction

1.1 Nanoscience and technology

Nanoscience is a distinct division in science that deals with the nano-sized (i.e., 1 to 100 nm) particles. The importance of the nanoparticles or nanomaterials is because of the distinct properties from their bulk counterparts. The study of these extremely small particles is known as nanoscience, and it can be used in almost every scientific sector, say physics, chemistry and biology, to develop advanced technology, so-called nanotechnology.

The term nanotechnology was first used by a well-known scientist Richard Feynman during the American physical society meeting on 29 December 1959. Feynman pronounced a way to employ individual atoms and molecules to build a proportionally smaller structure through a set of specific tools. The reduction in the size of particles to the nano range abruptly changes the properties (i.e., electrical, physical, chemical, etc.) of the material. In 1974, a professor at Tokyo science university named Norio Taniguchi explained in his paper “On the basic concept of nano-technology”, he explained the steps of nanotechnology, i.e., the processing, separation, consolidation and deformation of materials from a single atom or molecule. In 1980’s Dr. Eric Drexler described the significance of the nano range technologies through books and talks like “Engine of creation: the coming era of nanotechnology and nanosystem, manufacturing and computation, and molecular machinery”.

Nanostructured materials have become the cornerstones for recent developments in science and technology because they show entirely different properties from their bulk

counterparts. The properties of the materials, which are size-dependent like quantum confinement, surface plasmon resonance, etc., are observed only in nanoscale. In contrast, the bulk counterparts possess constant physical characteristics irrespective of their size. The production of the nanomaterials had started a long time back, even before nanotechnology was emerged as an innovative scientific sector. This interest has been amplified drastically in the past few decades [1]. These nanostructured materials have revolutionized the various core sectors in scientific fields: electronics, computing, biomedicine, communication, information storage, catalysis, energy conversion, environmental protection, space exploration, and other various sectors [2–5].

1.2 Types of Nanomaterials

Nanomaterials can be categorized as organic, inorganic, biological and composite materials. The inorganic nanomaterials can further be classified into the following categories:

1) **Carbon-based nanomaterials:** These are the materials that contain carbon as their primary nano component and are structured differently, say, in the form of a hollow sphere, ellipsoids, tubes, etc. Carbon nanotubes (CNT) are the graphene sheets rolled to form tubes, whereas the spherical and ellipsoidal structures of carbon are called fullerenes. Among other carbon structures, CNT quite fascinated the scientific community because of their unique mechanical and electrical properties [6–10]. The CNT possesses great potential for applications in energy storage, hydrogen storage medium, large-area display applications, etc.
2) **Metal nanoparticles:** This category mainly involves noble metals such as gold, silver, platinum, palladium, etc. With these, the transition metals are also being formed like copper, nickel, iron, etc. These materials play a substantial role in potential applications such as

catalysts, chemosensors, biosensors, optoelectronic devices, etc., because of their controllable size, shape, composition, and architecture [11–18].

3) **Semiconductor nanoparticles:** In nano-sized semiconductors, electronic, optical, chemical, and physical properties changed abruptly compared to their bulk counterparts. The scientific community has shown great interest in semiconductor nanoparticles because of their bandgap tuning capabilities with the size of the particles required for the desired applications. These materials are further classified as shape confinement in different dimensions (D), i.e., 1D, 2D, 3D and 0D. These semiconducting nanomaterials possess high chemical stability and are of low cost. Also, their quantum dots (0D nanomaterials) have gained great attention from the scientific community due to their unique applications in chemical, biological and optoelectronic fields.
4) **Magnetic Nanomaterials:** Those nanoparticles, which consist of the elements like iron, copper, nickel, etc., alter the magnetic properties of the nanoparticles. Recently, the nanoparticles with magnetic properties had gathered a lot of attention among researchers because of the potential applications of the nanoparticles in catalysis, data storage (flexible recording media), environmental remediation, biomedicine, magnetic particles imaging, magnetic resonance imaging (MRI) and magnetic fluid hyperthermia [19–27].
5) **Ceramic nanomaterials:** This particular group possesses the silicates, various oxides and non-oxides of inorganic materials, tuff metals and their composites [28–30]. These materials are primarily insulators and have multiple applications as photovoltaic devices, photo catalysis, electro ceramics, etc.

1.3 Quantum size effects

When the particle size becomes shorter than the de Broglie wavelength, electrons and holes of the nanocrystal are confined to a spatial space, hence increases the energy. As a result, the energy levels become discrete instead of continuous as in the bulk materials, shown in Fig. 1.1. The systematic variations in the density of states occurring in the electronic energy levels because of the changes in shape and size of the material result in variations in electronic and optical properties [31].

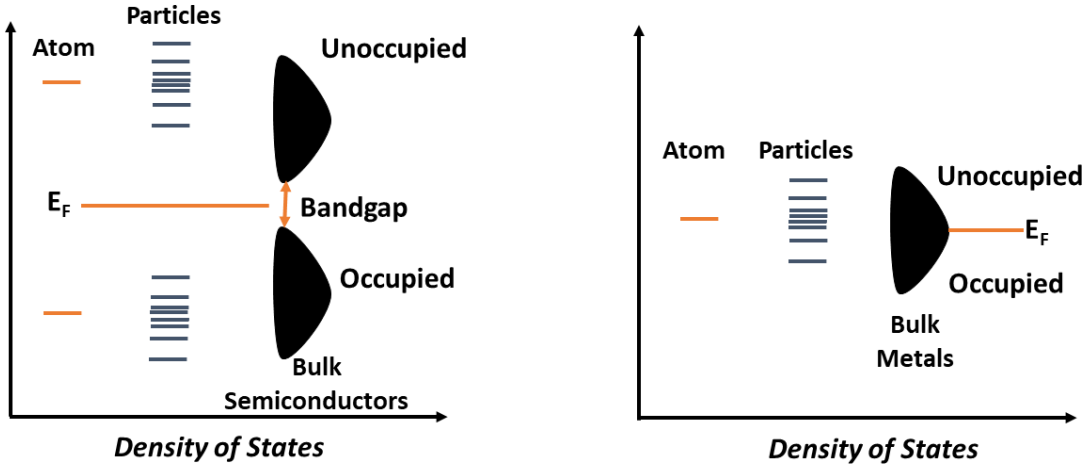

Figure 1.1 *The systematic density of states occurs in the electronic energy levels of bulk semiconductors and bulk metals.*

When the material size is reduced short to the nanoscale, an increase in their energy level spacing is noted as quantum confinement. Therefore, when the shape and size of the nanomaterials are constrained from 3-dimensional (3D) to 0-D, its confinement increases drastically and creates a lot more changes in the density of states (DOS) of the material. Fig. 1.2. shows the DOS vs. energy graph for 3, 2, 1 and 0-D materials.

1.3.1 3-D nanoparticles:

When the particles are not confined to any of the dimensions in nanoscale, the particles are popularly classified as 3-D nanoparticles. Some of the examples are metal oxides, ceramic materials, etc.

1.3.2 2-D nanomaterials:

When the nanomaterials are restricted only in one direction and form the quantum well and the plane sheet, are popularly classified as 2-D nanomaterials. In this class, the length and breadth of the plane are much bigger than its height, whose dimensions fall in the range comparable to the Bohr exciton radius of the material. Therefore, the thickness of the quantum well gets analogous to the de-Broglie wavelength of the carriers, i.e., electrons and holes, by increasing the energy levels because of the enactment of the quantum confinement effect.

1.3.3 1-D nanomaterials:

When the particles are confined in 2-D, only their length is elongated, then they are popularly classified as 1-D nanomaterials. Some examples of the 1-D nanomaterials are nanorods, nanowires, nanotubes, quantum wires, etc. Here, the quantum effect on the nanomaterial affects the electrical properties of the materials and hence increases the electrical conductivity of materials. This is because, the carriers (electrons) are bound to travel in a transverse direction of the wire, and its energy is quantized in packets of discrete values.

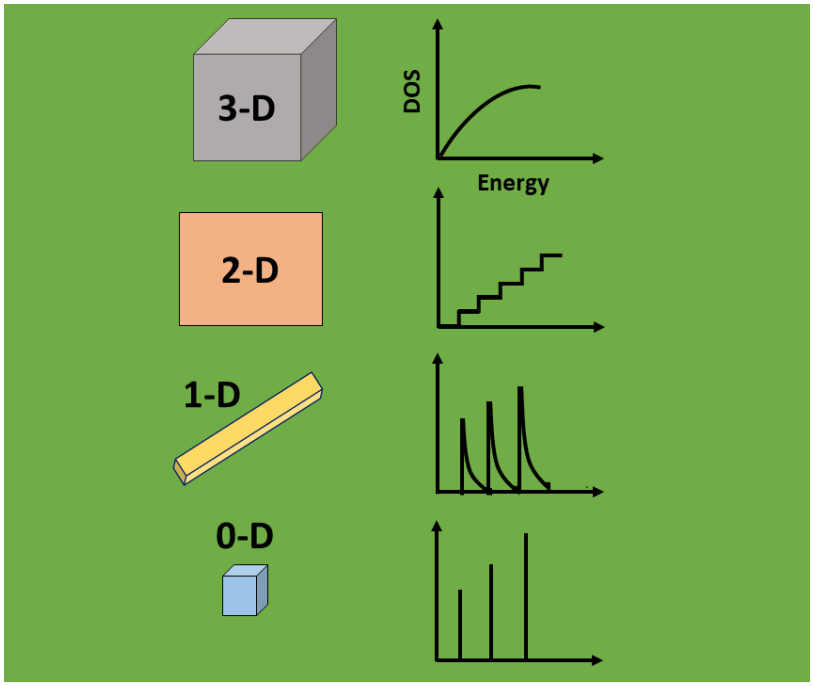

Figure 1.2 *The density of states vs. energy graph for 3, 2, 1 and 0-D materials.*

1.3.4 0-D nanoparticles:

In this class of nanomaterials, every dimension of the particle is confined in the nanoscale (<100 nm). The very famous example of 0-D nanomaterials is the quantum dots (QD), whose dimensions are shorter than the Bohr exciton radius. These tiny spheres are pretty popular because of their distinct properties and great potential applications, which we learn later in this chapter.

1.4 Synthesis of nanomaterials:

The nanomaterials are prepared through various 'physical' and 'chemical' techniques. Generally, there are two major approaches to fabricate the nanomaterials, which are as follow:

I. Top-down approach:

It has been elaborated on how to process nanomaterials from the past few decades and control the synthesis steps externally. A larger piece of material is kept and broken into numerous nanostructures through external forces acting over it. Such a kind of approach of

fabrication is known as the top-down method of synthesis. Some examples of the process are ball milling, scotch tape, electro-deposition synthesis, plasma arcing, lithographic etching techniques, etc. Many mesmerizing materials have been synthesized through these methods, but the cost of extraction was too high compared to the amount of material synthesized. Besides, it helped to get the purest form of the nanomaterials but have certain restrictions like imperfect surface structures and less control over the dimensions and the morphology of the particles.

II. Bottom-up approach:

This approach involves the self-assembly process leading to the formation of miniaturized nanoscale structures from the components, which sometimes are as low as atomic level. Whereas, to build larger structures, the physical forces at nanoscale works to keep the basic units altogether. Some examples of this synthesis approach are chemical vapor deposition (CVD), epitaxial growth synthesis, colloidal formation of particles, hydrothermal technique, etc. Both the methods have their advantages and disadvantages. Still, there is a fair chance to fabricate nanostructures in large amounts in bottom-up approaches, with fewer defects, cost-effective and better homogeneous chemical composition. The bottom-up method is treated to be a very efficient fabrication technique of the nanoparticles intended for the direct implications to the applications because the synthesis procedure involves the thermodynamic equilibrium state as long as it follows the reduction of Gibb's free energy [32]. Some commonly used synthesis techniques have been discussed as follows:

1.4.1 Plasma arcing technique

Here, the system possesses two electrodes in a discharge chamber at vacuum, and when the electric arc crosses the two electrodes, the anode vaporizes and gets stick at the cathode. This is the vital technology extensively used for the fabrication of carbon nanotubes (CNT), for which the carbon electrodes were being used.

1.4.2 Ball milling technique

This method is very similar to the mechanical crushing of the larger pieces to a small powder form. Here, the powdered material (~50 μm) has been kept inside the container with hard balls allowed to rotate inside it, press the material against the walls, and crush the solid into fine nanopowder. The cause the impart of the energy because of collisions and create smaller nanoparticles grain size.

1.4.3 Chemical vapour deposition (CVD)

This deposition technique includes the deposition of materials through the gas phase at high temperatures over a solid substrate. Here, the precursors mixed with the gas acting as a carrier to the hot substrate surface. As soon as the reactants come in contact with the substrate at a high temperature, the chemical reaction gets triggered to form a nanofilm over the surface of that substrate. This technique has revolutionized the synthesis of nanofilms in past decades due to its usability in developing the most mesmerizing materials like CNT, graphene, metal dichalcogenides, etc.

1.4.4 Sol-gel technique

As the name suggests, this method involves preparing the solution (sol) from the reactant materials followed by aging it to form a gel that later be post-treated to produce the final nanostructures in a very high amount and cost-effective manner. This technique has been used to create nanoparticles of size more than 50 nm in diameter. It is a very efficient

technique to control the size of the material because the method involves many steps like hydrolysis of reactants, poly condensations, gelation, and finally, the drying process (involves annihilation).

1.4.5 Electro-deposition technique

This is an effective method of synthesizing the material using away with fewer resources than any other technique. A fuel cell setup is used where the electrical current flows through the two electrodes and an electrolyte solution that acts as a transportation medium to the particles. The current electrically charged the reactants and allowed them to deposit over the electrode (cathode or anode) depends on the type of charge.

1.4.6 Hydrothermal technique

Hydrothermal is a chemical technique in which the reactants were kept in a closed vessel at high pressure/temperature in the water as solvent. The pressure inside the vessel reached height value with temperature and the amount of percentage of the vessel filled. The high pressure allows increasing the solubility and reactivity of the insoluble inorganic compounds even below the critical temperature of the water.

The hydrothermal method of producing nanomaterials has some of its advantages. It is a facile route to synthesize the materials and have great control over physical and chemical parameters. It makes it possible to operate the nanoparticle's growth finely, extract small size quantum structures, narrow size distribution, and require stoichiometry. By this method, metal, as well as semiconducting quantum nanostructures can be synthesized. The nanostructure growth majorly depends on the parameters like precursors used, temperature, percentage amount filled in the vessel, the surfactant type and the reaction time. The hydrothermal synthesis technique has been chosen over other approaches to

form molybdenum disulfide (MoS_2) nanostructures (2-D and 0-D) and its nanocomposites in the current work. The MoS_2 deposition could be done by many means like chemical bath deposition (CBD), metal-organic chemical vapour deposition (MOCVD), spray pyrolysis, atomic layer epitaxy and pulsed laser deposition [33–38]. This method has various other benefits, like the low-cost production of materials. Many nanoparticles can be produced quickly with small size, high crystallinity; additionally, surface modifications are possible.

1.5 Literature review

Molybdenum disulfide is a 2-D semiconductor material and considered highly for research for the last decade because of its magnificent electrical and optical properties. MoS_2 has promising applications in many sectors, gas sensors, photochemical catalysis, optoelectronic devices, solar cells, numerous luminescence devices, laser and infrared detectors, etc.[39,40]. Being MoS_2 so popular in the research community is because it is an inorganic cousin of graphene with many intriguing properties. As graphene has zero bandgap, being a semiconductor MoS_2 has a wide direct bandgap of 1.8 eV for a single layer and varies with the number of layers. This bandgap tuning with the size and number of layers makes it useful for applications discussed above according to their requirements.

1.5.1 Structure of MoS_2

The structure of MoS_2 can be best described as a layer of Mo packed between two hexagonal sulfur planes attached with strong covalent bonds, and interlayer planes were kept together by the weak Van der Waals forces. Likewise, other metals, transition metal dichalcogenides (MX_2) could also be described after replacing Mo metal atoms with other transition metals like Ti, Hr, V, Ta, W, etc., and sulfur with other chalcogenides say Se or Te. Therefore, the

single layer of these MX_2 consists of three atoms and exhibits completely different properties from their bulk counterparts [41,42].

In the 3-D structure of MoS_2, the covalent bonding and interlayer attractions have been observed. Because of this weak interlayer Van der Waals forces, the exfoliation of MoS_2 to the single layer is possible. The thickness of single-layer MoS_2 is reported to be 6.5 Å calculated by density functional theory at local density approximations [43]. They found the MoS_2 unit cell structure similar to the honeycomb lattice pattern, and layers are weakly held together with different order stacking. Generally, MoS_2 structures are polytypes, i.e., hexagonal (2H) and rhombohedral (3R) with trigonal prismatic coordination. The numbers 2 and 3 in the polytypes represent the number of layers. The 2H-MoS_2 is comparatively stable and dominant than the 3R-MoS_2. Upon heating, the 3R-MoS_2 can transform to 2H. The 2H and 3R-MoS_2 structures are majorly produced during the synthesis processes, but some exfoliation processes result in a metastable state of MoS_2. The lithium intercalation method while liquid phase exfoliation process of synthesis causes some changes in metal coordination from 2H to octahedral geometry (1T) [44]. The two different phases of MoS_2 exhibit different electronic properties as 2H is a semiconductor in nature while 1T is metallic.

1.5.2 Properties of MoS_2

The exfoliated ultrathin MoS_2 nanosheets exhibit physicochemical properties which are entirely different from their bulk counterparts because of the confinement of the charge carriers [45]. The bulk MoS_2 possesses the indirect bandgap of 1.2 eV, whereas the monolayer 2H-MoS_2 nanosheets have a direct bandgap of 1.9 eV. The increase in bandgap occurs because of the decrease in thickness [46]. Hence, strong photoluminescence is observed in monolayer MoS_2, which cannot attend its bulk counterpart [46]. The direct

bandgap of MoS_2 proves excellent potential for various applications in photonic and electronic fields like field-effect transistors (FET) sensors [47,48]. Also, the high effectivity of MoS_2 in photocatalytic reactions than other photoactive catalysts because of its lower direct bandgap. It lies in the visible range compared to others whose bandgap falls in the UV region, which is only 5% of the total solar light and makes it even more eminent for degradation of organic contaminants [49,50].

The benefits of MoS_2 over the nearest competitor of semi-metallic nature with zero bandgaps, i.e., graphene, includes direct implication in transistors, energy harvesting devices, optoelectronic devices and other environmental applications like electro/photo catalysis and sensing. Also, the 1T-MoS_2 nanosheets proved to be a promising cost-effective alternative to the electrocatalyst for the hydrogen evolution reaction (HER) because of the presence of numerous active sites over its surface [51,52]. These active sites have a higher affinity towards the thiol groups and can be adsorbed or removed easily from MoS_2 [53]. The commendably stable functionalization of MoS_2 could be obtained via chemical reactions with electrophiles like aryl diazonium or organohalide, etc., because of the electron-rich 1T phase of MoS_2 [54].

PROPERTIES OF MOS_2

PHYSICAL APPEARANCE	Black/lead-grey solid
MOLAR WEIGHT	160.07 g/mol
DENSITY	5.06 g/cm^3
WATER SOLUBILITY	Insoluble

SOLUBILITY	• Soluble in sulfuric acid, hot aqua regia, nitric acid • Does not dissolve in dilute or weak acids
MELTING TEMPERATURE	2,375 °C
STRUCTURE	• hR9, R3m, No 160 (3R) • hP6, $P6_3/mmc$, No. 194 (2H)
GEOMETRY	Trigonal prismatic (Mo^{IV}) Pyramidal (S^{-2})
LATTICE PARAMETERS	a = 0.3161 nm (2H), 0.3163 nm (3R) c = 1.2295 nm (2H), 1.837 (3R)
ENERGY BAND GAP	~1.23 eV (indirect) ~1.8 eV (direct, monolayer)

Table 1.1 *Physical properties of MoS_2.*

1.5.3 MoS_2 quantum dots

The MoS_2 quantum dots (QDs) possess entirely different electronic and optical properties than the 2-D nanostructure due to the enactment of the quantum confinement and the edge effects [55–59]. The MoS_2 QDs have attracted the research community in the last decade because of their low level of toxicity, excellent optical performance, abundance availability and high stability [60]. They exhibit an excellent surface-to-volume ratio and great in-plane electronic transportation ability than other nanostructures of MoS_2 [61]. The MoS_2 QDs have been employed because of their remarkable size tuned electronic and optical properties for the applications like hydrogen evolution reactions (HER), chemo-sensors, bio-sensors,

photodetectors and as a photocatalyst [62–67]. The increase in the bandgap of MoS_2 is because of the quantum confinement. When the particle size is restricted within 2-4 nm and the direct bandgap became 3.9 eV, which is higher than the monolayer MoS_2 [68]. When the size of MoS_2 nanosheets are reduced to their QDs, the changes occurred in the properties of the material such as, formation energy, spin and charge density of MoS_2 arises due to the quantum mechanical as reported by Gan *et al.* [69]. Also, the effect of dangling bonds over for the MoS_2 QDs was observed.

The MoS_2 QDs exhibits blue emission under the illumination of ultraviolet (UV) radiation, which arises because of the transition from the K point of Brillouin zone [70]. The fluorescent behaviour of the MoS_2 QDs, open gate for the numerous applications in the field of sensors, as some of them are sensing biomolecules (i.e., BSA, hyaluronidase, and dopamine), nitro-explosive compound (2,4,6-trinitrophenol), pesticides (methyl parathion) and other chemical compounds (such as hydrogen peroxide, glucose, hypochlorite) [71–75]. Sufficient research is needed to prove the MoS_2 QDs as an efficient sensor for metal ions like Fe^{3+}, Cu^{2+} and Al^{3+} [76–79], as the study based on MoS_2 QDs as the metal ion sensor is limited [80]. To achieve fluorescent MoS_2 QDs, both the top-down and bottom-up approaches could be employed. In comparison, the bottom-up approach is preferred over the top-down approach because the top-down method involves the use of the organic solvent, harmful reagents, and a very long process [21]. The bottom-up method involves the chemical reaction taking place between the Mo/S precursors which involves a capping reagent, the parameters of the reaction conditions could be controlled effectively for the production of high-end product.

1.6 Problem statement and objectives

The above literature review describes the significance of the material MoS_2 nanostructures due to their outstanding potential for various applications in sectors like environmental, biological, sensing, energy storage, etc. The literature described the two main nanostructures of MoS_2, i.e., the nanosheets and the quantum dots. Both of them are very different in properties instead of the same composition, though they could be employed for different jobs according to their practicality. The main objective behind the thesis work is to synthesize the MoS_2 nanostructures and exploit their properties for various applications, say sensing and photocatalytic activity.

The proposed research objectives include studying structural, morphological, electrical, compositional and optical properties of MoS_2 nanostructures and discussing their utility for sensing and photocatalytic applications. The MoS_2 nanosheets and quantum dots will be synthesized through the facile hydrothermal route, different sizes of the particles will be prepared to explore their properties comprehensively. The optical properties of MoS_2 nanostructures (like absorption, photoluminescence (PL) and PL lifetime) along with the different sensing and photocatalytic applications will also be explored in detail. The applications based on the magnificent properties of the MoS_2 nanostructures will also be discovered to prove beneficial for the environment and human beings.

References

[1] A. Mnyusiwalla, A.S. Daar, P.A. Singer, “Mind the gap”: Science and ethics in nanotechnology, Nanotechnology. 14 (2003) R9.

[2] J. Dobson, Nanoscale biogenic iron oxides and neurodegenerative disease, FEBS Lett. 496 (2001) 1–5.

[3] W.P. McConnell, J.P. Novak, L.C. Brousseau, R.R. Fuierer, R.C. Tenent, D.L. Feldheim, Electronic and optical properties of chemically modified metal nanoparticles and molecularly bridged nanoparticle arrays, J. Phys. Chem. B. 104 (2000) 8925–8930.

[4] A.A. Lizunova, E.G. Kalinina, I. V. Beketov, V. V. Ivanov, Development of Reference Materials for the Diameter of Nanoparticles of Colloidal Solutions of Aluminum Oxide and Titanium Dioxide, Meas. Tech. 57 (2014) 848–854.

[5] A. K. Cheetham and P. S. Grubstein, Nanomaterials and venture capital - Materials Today 6 (2003) 16–19.

[6] W. Xing, S. Zhuo, H. Cui, W. Si, X. Gao, Z. Yan, Enhanced electrochemical properties of polyaniline-coated multiwall carbon nanotubes, J. Porous Mater. 15 (2008) 647–651.

[7] S.A. Chesnokov, V.A. Nalimova, A.G. Rinzler, R.E. Smalley, J.E. Fischer, Mechanical Energy Storage in Carbon Nanotube Springs, Phys. Rev. Lett. 82 (1999) 343–346.

[8] A.S. Aricò, P. Bruce, B. Scrosati, J.M. Tarascon, W. Van Schalkwijk, Nanostructured materials for advanced energy conversion and storage devices, Nat. Mater. 4 (2005) 366–377.

[9] J. Shui, M. Wang, F. Du, L. Dai, N-doped carbon nanomaterials are durable catalysts for oxygen reduction reaction in acidic fuel cells, Sci. Adv. 1 (2015) e1400129.

[10] H.J. In, S. Kumar, Y. Shao-Horn, G. Barbastathis, Origami fabrication of nanostructured, three-dimensional devices: Electrochemical capacitors with carbon electrodes, Appl. Phys. Lett. 88 (2006) 083104.

[11] J. Cure, Y. Coppel, T. Dammak, P.F. Fazzini, A. Mlayah, B. Chaudret, P. Fau, Monitoring the coordination of amine ligands on silver nanoparticles using NMR and SERS, Langmuir. 31 (2015) 1362–1367.

[12] D.L. Feldheim, C.D. Keating, Self-assembly of single electron transistors and related devices, Chem. Soc. Rev. 27 (1998) 1–12.

[13] C.P. Tsangarides, A.K. Yetisen, F. Da Cruz Vasconcellos, Y. Montelongo, M.M. Qasim, T.D. Wilkinson, C.R. Lowe, H. Butt, Computational modelling and characterisation of nanoparticle-based tuneable photonic crystal sensors, RSC Adv. 4 (2014) 10454–10461.

[14] H. Sharma, P.K. Mishra, S. Talegaonkar, B. Vaidya, Metal nanoparticles: A theranostic nanotool against cancer, Drug Discov. Today. 20 (2015) 1143–1151.

[15] S.R. Emory, S. Nie, Screening and enrichment of metal nanoparticles with novel optical properties, J. Phys. Chem. B. 102 (1998) 493–497.

[16] J.M. Thomas, Colloidal metals: Past, present and future, Pure Appl. Chem. 60 (1988)

1517–1528.
[17] T.S. Ahmadi, Z.L. Wang, T.C. Green, A. Henglein, M.A. El-Sayed, Shape-controlled synthesis of colloidal platinum nanoparticles, science. 272 (1996) 1924–1926.
[18] W. Yu, H. Liu, Quantity Synthesis of Nanosized Metal Clusters, Chem. Mater. 10 (1998) 1205–1207.
[19] Q.A. Pankhurst, J. Connolly, S.K. Jones, J. Dobson, Applications of magnetic nanoparticles in biomedicine, J. Phys. D. Appl. Phys. 36 (2003) R167.
[20] Contents: (Adv. Healthcare Mater. 4/2015), Adv. Healthc. Mater. 4 (2015) 481–486.
[21] S.V. Gopal, R. Mini, V.B. Jothy, I.H. Joe, Synthesis and Characterization of Iron Oxide Nanoparticles using DMSO as a Stabilizer, in: Mater. Today Proc., Elsevier Ltd, 2 (2015) 1051–1055.
[22] A.K. Gupta, M. Gupta, Synthesis and surface engineering of iron oxide nanoparticles for biomedical applications, Biomaterials. 26 (2005) 3995–4021.
[23] Archana S., A Comparative study of iron oxide nanoparticles surface modified using carboxylic acids, Int. J. Res. Appl. Sci. Biotechnol. 8 (2021) 116–125.
[24] H. Nemala, J.S. Thakur, V.M. Naik, P.P. Vaishnava, G. Lawes, R. Naik, Investigation of magnetic properties of Fe_3O_4 nanoparticles using temperature dependent magnetic hyperthermia in ferrofluids, J. Appl. Phys. 116 (2014) 034309.
[25] D.W. Elliott, W.X. Zhang, Field assessment of nanoscale bimetallic particles for groundwater treatment, Environ. Sci. Technol. 35 (2001) 4922–4926.
[26] T. Hyeon, Chemical synthesis of magnetic nanoparticles, Chem. Commun. 3 (2003) 927–934.
[27] S.I. Thakore, P.S. Rathore, Nanoparticle-assisted organic transformations, In: Aliofkhazraei M. (eds) Handbook of Nanoparticles, Springer International Publishing, (2015) 769–801.
[28] Ceramic matrix composites : microstructure, properties and applications, Woodhead Pub. and Maney Pub. on behalf of the Institute of Materials, Minerals & Mining, Cambridge, England (2006).
[29] Ceramic Nanomaterials and Nanotechnology IV: Proceedings of the 107th annual meeting of the american ceramic society, Baltimore, Maryland, USA (2005).
[30] P. Newman, Z. Lu, S.I. R. Esfahani, T.L. Church, M. Biro, B. Davies, A. King, K. Mackenzie, A.I. Minett, H. Zreiqat, Porous and strong three-dimensional carbon nanotube coated ceramic scaffolds for tissue engineering, J. Mater. Chem. B. 3 (2015).
[31] R. Rossetti, S. Nakahara, L.E. Brus, Quantum size effects in the redox potentials, resonance Raman spectra, and electronic spectra of CdS crystallites in aqueous solution, J. Chem. Phys. 79 (1983) 1086–1088.
[32] M. Ge, C. Cao, J. Huang, S. Li, Z. Chen, K.-Q. Zhang, S.S. Al-Deyab, Y. Lai, A review of one-dimensional TiO_2 nanostructured materials for environmental and energy applications, J. Mater. Chem. A 4 (2016) 6772-6801.
[33] R. Dingle, W. Wiegmann, C.H. Henry, Quantum states of confined carriers in very thin

$Al_xGa_{1-x}As$-GaAs-$Al_xGa_{1-x}As$ heterostructures, Phys. Rev. Lett. 33 (1974) 827–830.
[34] A.P. Alivisatos, Semiconductor clusters, nanocrystals, and quantum dots, science. 271 (1996) 933–937.
[35] N.I. Fainer, Y.M. Rumyantsev, E.G. Salman, M.L. Kosinova, G.S. Yurjev, N.P. Sysoeva, E.A. Maximovskii, S. V. Sysoev, A.N. Golubenko, Plasma-deposited CdS layers from (o-phen)bis(diethyldithiocarbamate) cadmium, Thin Solid Films. 286 (1996) 122–126.
[36] B. Ullrich, H. Sakai, Y. Segawa, Optoelectronic properties of thin film CdS formed by ultraviolet and infrared pulsed-laser deposition, Thin Solid Films. 385 (2001) 220–224.
[37] D.B. Holt, The growth and structure of epitaxial films and heterojunctions of II-VI compounds, Thin Solid Films. 24 (1974) 1–53.
[38] Y. Luo, M. Han, D.A. Slater, R.M. Osgood, Studies of heteroepitaxial growth of thin II–VI semiconductor layers by sequential ultrahigh vacuum dosing, J. Vac. Sci. Technol. A Vacuum, Surfaces, Film. 18 (2000) 438–449.
[39] K.P. Acharya Rony S Khnayzer Timothy O, C. Geoffrey Diederich Maria Kirsanova, The Role of Hole Localization in Sacrificial Hydrogen Production by Semiconductor–Metal Heterostructured Nanocrystals, Nano Lett. 11 (2011) 2919–2926.
[40] V. Singh, P. Chauhan, Synthesis and structural properties of wurtzite type cds nanoparticles, Chalcogenide Letters 6 (2009) 421 – 426.
[41] Q.H. Wang, K. Kalantar-Zadeh, A. Kis, J.N. Coleman, M.S. Strano, Electronics and optoelectronics of two-dimensional transition metal dichalcogenides, Nat. Nanotechnol. 7 (2012) 699–712.
[42] Y. Ding, Y. Wang, J. Ni, L. Shi, S. Shi, W. Tang, First principles study of structural, vibrational and electronic properties of graphene-like MX_2 (M=Mo, Nb, W, Ta; X=S, Se, Te) monolayers, Phys. B Condens. Matter. 406 (2011) 2254–2260.
[43] T. Cao, G. Wang, W. Han, H. Ye, C. Zhu, J. Shi, Q. Niu, P. Tan, E. Wang, B. Liu, J. Feng, Valley-selective circular dichroism of monolayer molybdenum disulphide, Nat. Commun. 3 (2012) 1–5.
[44] G. Eda, T. Fujita, H. Yamaguchi, D. Voiry, M. Chen, M. Chhowalla, Coherent atomic and electronic heterostructures of single-layer MoS_2, ACS Nano. 6 (2012) 7311–7317.
[45] M. Chhowalla, H.S. Shin, G. Eda, L.J. Li, K.P. Loh, H. Zhang, The chemistry of two-dimensional layered transition metal dichalcogenide nanosheets, Nat. Chem. 5 (2013) 263–275.
[46] A. Splendiani, L. Sun, Y. Zhang, T. Li, J. Kim, C.Y. Chim, G. Galli, F. Wang, Emerging photoluminescence in monolayer MoS_2, Nano Lett. 10 (2010) 1271–1275.
[47] D.J. Late, Y.K. Huang, B. Liu, J. Acharya, S.N. Shirodkar, J. Luo, A. Yan, D. Charles, U. V. Waghmare, V.P. Dravid, C.N.R. Rao, Sensing behavior of atomically thin-layered MoS_2 transistors, ACS Nano. 7 (2013) 4879–4891.
[48] H. Li, Z. Yin, Q. He, H. Li, X. Huang, G. Lu, D.W.H. Fam, A.I.Y. Tok, Q. Zhang, H. Zhang, Fabrication of single- and multilayer MoS_2 film-based field-effect transistors for

sensing NO at room temperature, Small. 8 (2012) 63–67.
[49] A. Midya, A. Ghorai, S. Mukherjee, R. Maiti, S.K. Ray, Hydrothermal growth of few layer 2H-MoS_2 for heterojunction photodetector and visible light induced photocatalytic applications, J. Mater. Chem. A. 4 (2016) 4534–4543.
[50] C. Liu, D. Kong, P.C. Hsu, H. Yuan, H.W. Lee, Y. Liu, H. Wang, S. Wang, K. Yan, D. Lin, P.A. Maraccini, K.M. Parker, A.B. Boehm, Y. Cui, Rapid water disinfection using vertically aligned MoS_2 nanofilms and visible light, Nat. Nanotechnol. 11 (2016) 1098–1104.
[51] G. Eda, T. Fujita, H. Yamaguchi, D. Voiry, M. Chen, M. Chhowalla, Coherent atomic and electronic heterostructures of single-layer MoS_2, ACS Nano. 6 (2012) 7311–7317.
[52] M.A. Lukowski, A.S. Daniel, F. Meng, A. Forticaux, L. Li, S. Jin, Enhanced hydrogen evolution catalysis from chemically exfoliated metallic MoS_2 nanosheets, J. Am. Chem. Soc. 135 (2013) 10274–10277.
[53] X. Chen, N.C. Berner, C. Backes, G.S. Duesberg, A.R. McDonald, Functionalization of two-dimensional MoS_2 : On the reaction between MoS_2 and organic thiols, Angew. Chemie Int. Ed. 55 (2016) 5803–5808.
[54] D. Voiry, A. Goswami, R. Kappera, C.D.C.C.E. Silva, D. Kaplan, T. Fujita, M. Chen, T. Asefa, M. Chhowalla, Covalent functionalization of monolayered transition metal dichalcogenides by phase engineering, Nat. Chem. 7 (2015) 45–49.
[55] J. Li, J.J. Zhu, Quantum dots for fluorescent biosensing and bio-imaging applications, Analyst. 138 (2013) 2506–2515.
[56] H.D. Ha, D.J. Han, J.S. Choi, M. Park, T.S. Seo, Dual role of blue luminescent MoS_2 quantum dots in fluorescence resonance energy transfer phenomenon, Small. 10 (2014) 3858–3862.
[57] G.U. Siddiqui, J. Ali, K.H. Choi, Y. Jang, K. Lee, Fabrication of blue luminescent MoS_2 quantum dots by wet grinding assisted co-solvent sonication, J. Lumin. 169 (2016) 342–347.
[58] P. Sharma, M.S. Mehata, Colloidal MoS_2 quantum dots based optical sensor for detection of 2,4,6-TNP explosive in an aqueous medium, Opt. Mater. (Amst). 100 (2020) 109646.
[59] P. Sharma, M.S. Mehata, Rapid sensing of lead metal ions in an aqueous medium by MoS_2 quantum dots fluorescence turn-off, Mater. Res. Bull. 131 (2020) 110978.
[60] X. Ren, L. Pang, Y. Zhang, X. Ren, H. Fan, S. Liu, One-step hydrothermal synthesis of monolayer MoS_2 quantum dots for highly efficient electrocatalytic hydrogen evolution, J. Mater. Chem. A. 3 (2015) 10693–10697.
[61] J. Kibsgaard, Z. Chen, B.N. Reinecke, T.F. Jaramillo, Engineering the surface structure of MoS_2 to preferentially expose active edge sites for electrocatalysis, Nat. Mater. 11 (2012) 963–969.
[62] W. Gao, M. Wang, C. Ran, L. Li, Facile one-pot synthesis of MoS_2 quantum dots-graphene-TiO_2 composites for highly enhanced photocatalytic properties, Chem.

Commun. 51 (2015) 1709–1712.
[63] D. Kufer, I. Nikitskiy, T. Lasanta, G. Navickaite, F.H.L. Koppens, G. Konstantatos, Hybrid 2D-0D MoS_2 -PbS quantum dot photodetectors, Adv. Mater. 27 (2015) 176–180.
[64] Y. Wang, Y. Ni, Molybdenum disulfide quantum dots as a photoluminescence sensing platform for 2,4,6-trinitrophenol detection, Anal. Chem. 86 (2014) 7463–7470.
[65] S. Xu, D. Li, P. Wu, One-pot, facile, and versatile synthesis of monolayer MoS_2 /WS_2 quantum dots as bioimaging probes and efficient electrocatalysts for hydrogen evolution reaction, Adv. Funct. Mater. 25 (2015) 1127–1136.
[66] H. Lin, C. Wang, J. Wu, Z. Xu, Y. Huang, C. Zhang, Colloidal synthesis of MoS_2 quantum dots: Size-dependent tunable photoluminescence and bioimaging, New J. Chem. 39 (2015) 8492–8497.
[67] W. Qiao, S. Yan, X. Song, X. Zhang, Y. Sun, X. Chen, W. Zhong, Y. Du, Monolayer MoS_2 quantum dots as catalysts for efficient hydrogen evolution, RSC Adv. 5 (2015) 97696–97701.
[68] H. Huang, C. Du, H. Shi, X. Feng, J. Li, Y. Tan, W. Song, Water-soluble monolayer molybdenum disulfide quantum dots with upconversion fluorescence, Part. Part. Syst. Charact. 32 (2015) 72–79.
[69] Z.X. Gan, L.Z. Liu, H.Y. Wu, Y.L. Hao, Y. Shan, X.L. Wu, P.K. Chu, Quantum confinement effects across two-dimensional planes in MoS_2 quantum dots, Appl. Phys. Lett. 106 (2015) 233113.
[70] H.D. Ha, D.J. Han, J.S. Choi, M. Park, T.S. Seo, Dual role of blue luminescent MoS_2 quantum dots in fluorescence resonance energy transfer phenomenon, Small. 10 (2014) 3858–3862.
[71] R. Feyisa Bogale, J. Ye, Y. Sun, T. Sun, S. Zhang, A. Rauf, C. Hang, P. Tian, G. Ning, Highly selective and sensitive detection of metal ions and nitroaromatic compounds by an anionic europium (III) coordination polymer, Dalt. Trans. 45 (2016) 11137–11144.
[72] W. Gu, Y. Yan, C. Zhang, C. Ding, Y. Xian, One-step synthesis of water-soluble MoS_2 quantum dots via a hydrothermal method as a fluorescent probe for hyaluronidase detection, ACS Appl. Mater. Interfaces. 8 (2016) 11272–11279.
[73] D.R. Hang, D.Y. Sun, C.H. Chen, H.F. Wu, M.M.C. Chou, S.E. Islam, K.H. Sharma, Facile bottom-up preparation of WS_2-based water-soluble quantum dots as luminescent probes for hydrogen peroxide and glucose, Nanoscale Res. Lett. 14 (2019) 271.
[74] H. Swaminathan, K. Balasubramanian, Förster resonance energy transfer between MoS_2 quantum dots and polyaniline for turn-on bovine serum albumin sensing, Sensors Actuators, B Chem. 264 (2018) 337–343.
[75] X. Liu, W. Zhang, L. Huang, N. Hu, W. Liu, Y. Liu, S. Li, C. Yang, Y. Suo, J. Wang, Fluorometric determination of dopamine by using molybdenum disulfide quantum dots, Microchim. Acta. 185 (2018) 1–8.
[76] Q. Wu, X. Wang, Y. Jiang, W. Sun, C. Wang, M. Yang, C. Zhang, MoS_2-QD-based

dual-model photoluminescence sensing platform for effective determination of Al^{3+} and Fe^{3+} simultaneously in various environment, ChemistrySelect. 3 (2018) 2326–2331.

[77] X. Li, D.W. He, Y.S. Wang, Y. Hu, X. Zhao, C. Fu, J.Y. Wu, Facile and controllable synthesis of molybdenum disulfide quantum dots for highly sensitive and selective sensing of copper ions, Chinese Phys. B. 27 (2018) 056104.

[78] H. Cao, H. Wang, Y. Huang, Y. Sun, S. Shi, M. Tang, Quantification of gold (III) in solution and with a test stripe via the quenching of the fluorescence of molybdenum disulfide quantum dots, Microchim. Acta. 184 (2017) 91–100.

[79] L. Hu, Q. Zhang, X. Gan, W. Yin, W. Fu, Switchable fluorescence of MoS_2 quantum dots: a multifunctional probe for sensing of chromium (VI), ascorbic acid, and alkaline phosphatase activity, Anal. Bioanal. Chem. 410 (2018) 7551–7557.

[80] R.K. Ratnesh, M.S. Mehata, Investigation of biocompatible and protein sensitive highly luminescent quantum dots/nanocrystals of CdSe, CdSe/ZnS and CdSe/CdS, Spectrochim. Acta - Part A Mol. Biomol. Spectrosc. 179 (2017) 201–210.

CHAPTER 2

Experimental Tools and Techniques

This chapter includes the detail experimental procedures and characterization techniques used throughout the thesis work. It comprises all the basic information and parameters involved while recording the data. The chapter discusses the fundamental aspects of optimizing the methodologies acquired during experiments and the statistical approach used to analyze the obtained results. The description of structural, vibrational and morphological features for the prepared nanoparticles can be picturized with analysis tools like X-ray diffractometer, Fourier transform Infrared spectroscopy, scanning electron microscopy (SEM), high-resolution transmission electron microscopy. The optical characteristics of nanoparticles were recorded by equipment like UV-visible absorption spectrometer, photoluminescence (PL) spectrofluorometer, and time-correlated single-photon counting system. The presented ray diagrams of the characterization techniques, describes their working, device descriptions, operational controls, and features to understand the instruments better.

2.1 X-Ray diffraction (XRD)

X-ray diffraction is a well-recognized technique to gather information, like crystal structure, lattice constants, geometry, phase orientation, determination of unknown materials stress and strain of any materials. It is one of the fundamental and powerful techniques used commonly to study the any materials in nanostructures as well as in bulk form [1,2].

The diffractometer possesses an X-ray source, two movable arms for enabling motion of source and detector. The detector is formed in a circular shape, focusing the center where the

sample is placed. The source tube produces the X-ray by hitting an anode metal target (Cu, Mo, Fe, Cr) through the high voltage electron beam in a vacuum environment. The detector counts the number of photons of particular energy striking for each angle 2θ, which is directly responsible for peak intensity [3]. The schematic representation of the X-ray diffractometer is shown in Fig. (2.1).

The wave nature of X-rays best explains the diffraction process. The intensity and diffraction angles of various diffracted beams are structure-dependent. The Bravice point lattice and unit cell dimensions are responsible for variation in diffracted angles. Whereas the geometrical relationship of atoms and their respective atomic numbers are responsible for diffracted intensities.

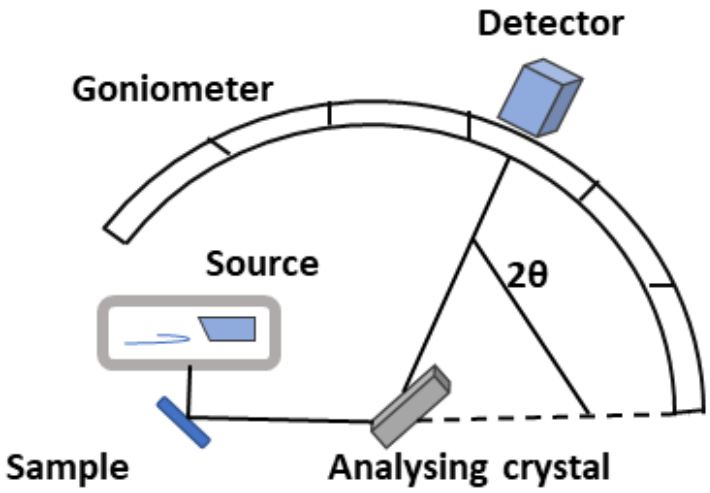

Figure 2.1. *Schematic representation of an X-ray diffractometer.*

The typical powder XRD patterns usually collect data from 5 to 80^{o} in a single scan. The fundamental principle for XRD is the wavelength of x-ray radiation incident over the crystallized sample should have comparable interatomic spacing in the lattice. Therefore, the

generalized relation for calculating angular distribution pattern derived from the crystal lattice is obtained by Bragg's Eq. (2.1) [4].

$$\mathbf{2dsin\theta = n\lambda} \qquad \textbf{(2.1)}$$

where 'd' corresponds to the distance between two atoms, 'n' is an integer, θ is the angle of incident rays and 'λ' is the wavelength. The diffracted X-ray intensity depends on the diffraction angle 2θ and the orientation of the specimen. XRD is a widely used technique as no special sample preparation is required and provides much information about the material [5]. By using the Scherer' formula (Eq. 2.2), crystallite size 'D' of the materials can be determined from the peak width, i.e.,

$$\boldsymbol{D = \frac{K\lambda}{\beta_{1/2} cos\theta_B}} \qquad \textbf{(2.2)}$$

where θ_B is the Bragg angle, $\beta_{1/2}$ is the full width at half maximum (FWHM) of the peak and 'K' is the constant depending upon the geometry of the material. The broadening of the peak indicates a reduction in the size of the sample particles.

XRD measurements were recorded in reflection mode by a Bruker diffractometer D8 advance operated at 45 kV with $CuK\alpha$ radiation ($\lambda = 1.546$Å). The Bruker D8 advance diffractometer is shown in Fig. (2.2).

Figure 2.2. Photograph of *Bruker D8 advance x-ray diffractometer*.

2.2 High-resolution transmission electron microscopy (HR-TEM)

HR-TEM is a powerful tool to gather the image of the nano-sized materials/nanoparticles to study their structure, size and compositional properties. In this technique, a high energy electron beam (~1 MeV) is to be passed through the specimen and the transmitted electrons are collected by a detector to form a magnified of the material and provides the morphology and the structural defects of the materials The transmitted beam of electrons undergoes a line of multiple lenses before hitting the phosphor screen detectors or sensors such as a charge-coupled device (CCD) camera.

Figure 2.3. *Photograph of HR-TEM system, Thermo Scientific, Talos.*

It has an arrangement of a flexible lens that offers information regarding the crystal structure of the material of interest and is called selected area electron diffraction (SAED) [6]. Here, the condenser lenses are used to defocus and direct a parallel electron beam towards the specimen and a selected area aperture is used to consider the specific area. We had used TALOS, Thermo scientific instruments for the HR-TEM

working at an accelerating voltage of 200 kV to record the high-resolution images of the nanoparticles, as shown in Fig. (2.3).

2.3 Absorption (UV/Vis/NIR spectrometer)

The absorption spectroscopy, popularly known as UV-visible absorption spectroscopy, plays a vital role to study the optical properties of the matter and feeds us with various significant parameters like optical energy bandgap, molar extinction coefficient and the size of the nanomaterials. In this measurement, the material is exposed to the light where the photons are absorbed by the electrons of the matter. Some of the energy is transmitted through it, producing an absorption spectrum based on absorbed and transmitted light. The absorbed energy causes the electronic transitions from ground states to the higher excited states of the materials. The spectrophotometer measures the absorption at each wavelength in the UV-vis range (usually 200 to 800 nm) and produces data as a spectrum between absorbance and wavelength. At a specific wavelength of light, the spectrum may follow the Beer-Lamberts law, as shown in Eq. (3):

$$\boldsymbol{A = log\frac{I_o}{I} = \varepsilon lc} \qquad \textbf{(2.3)}$$

where '*Io*' is the incident radiation intensity, '*I*' is the intensity of transmitted radiation from the specimen, c is the concentration exposed to the light (M), ε is the molar extinction coefficient ($Lmol^{-1}cm^{-1}$) and l is the path length (cuvette width).

Figure (2.4) demonstrates the ray diagram of the UV-vis/NIR spectrometer. In this system, two different sources i.e., deuterium and tungsten halogen lamps are used to measure absorption profile. The utmost part of the radiation emitted, falls in the near infrared (NIR) region. The beam of light (UV/visible) is separated into its constituent components using

diffraction grating or the prism. The produced beam of light is split into two equal intensity components with the help of half-mirror devices.

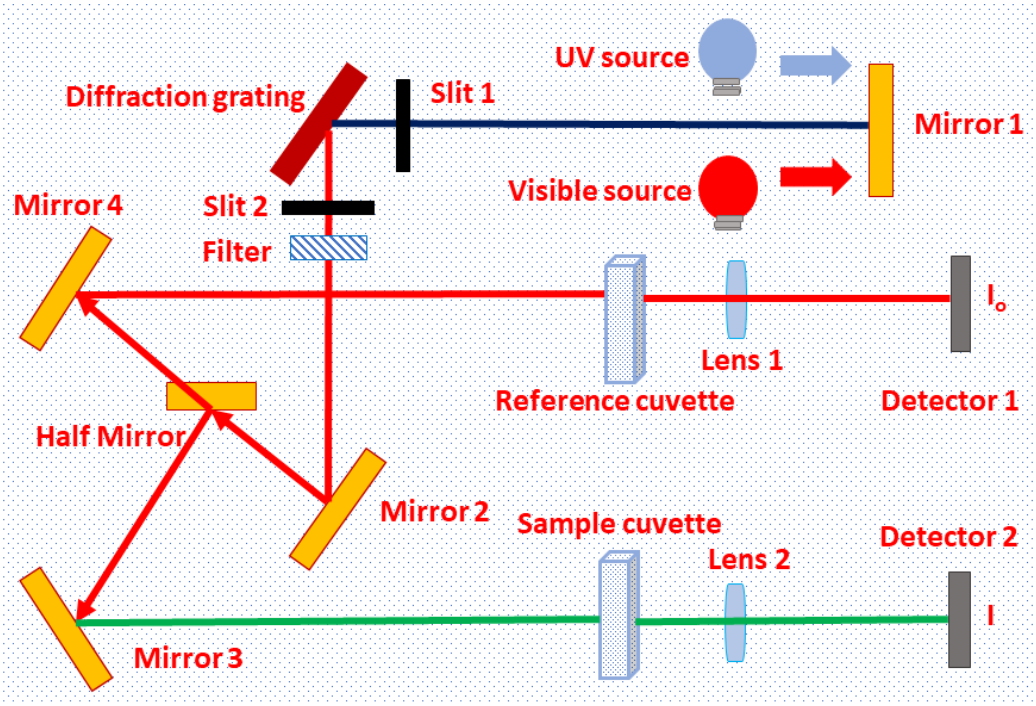

Figure 2.4. *UV/Visible absorption spectrophotometer ray diagram.*

These two components of light pass through the reference cuvette and the sample cuvette and finally, the absorption is obtained using the ratio recording method. We have used the UV/Vis/NIR spectrophotometer by Perkin Elmer, Lambda-750 (ranges 250-3300 nm) for absorption measurements (Fig. 2.5).

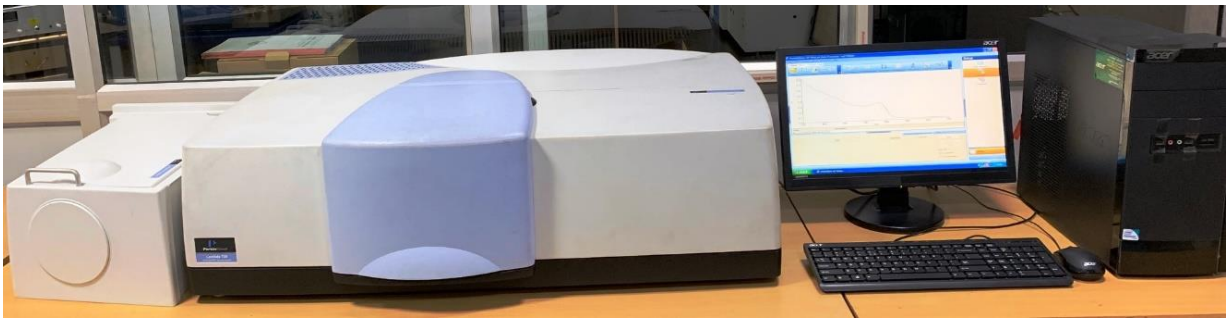

Figure 2.5. *Photograph of UV/Visible/NIR spectrometer, Lambda-750, Perkin Elmer.*

2.4 Photoluminescence (PL) (Spectrofluorometer)

PL is the phenomenon of re-emission of the absorbed light by the specimen because of the electronic transitions that occurred from a ground state to the higher excited states of the atom/molecule. The relaxation process of excited electrons to the ground state with radiative transitions is known as fluorescence/photoluminescence, which is generally completed within nanoseconds/microsecond.

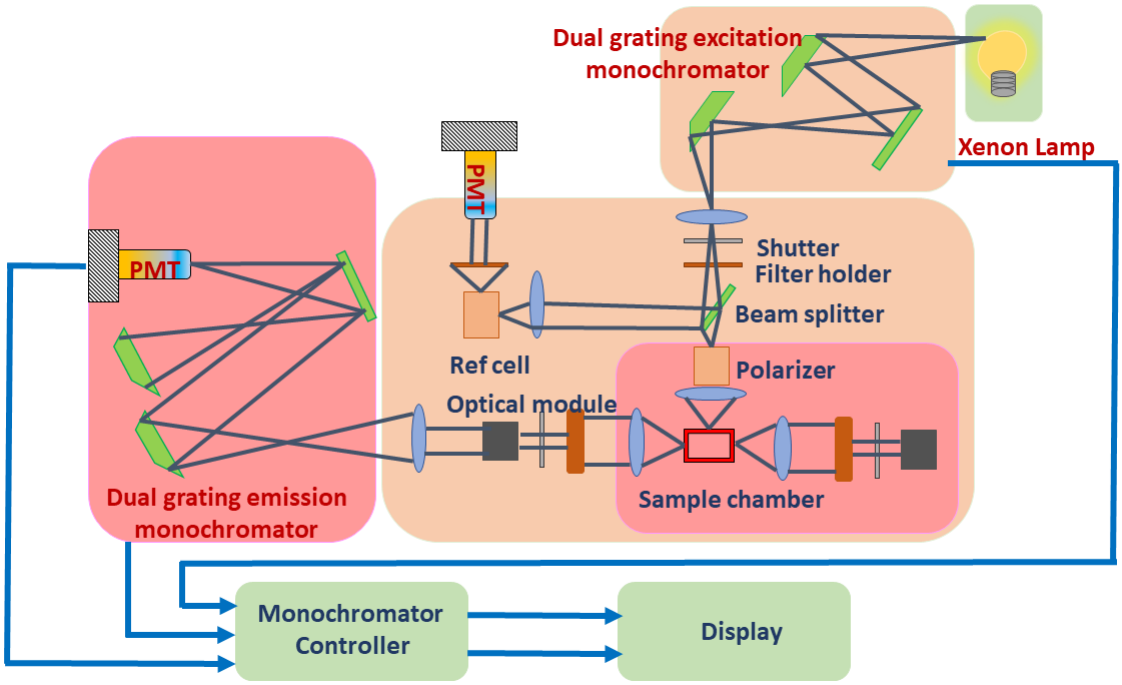

Figure 2.6. *Photoluminescence spectrofluorometer ray diagram.*

PL spectroscopy is a beneficial and sensitive technique to gather vital information about specimen compositions, mono-dispersibility of the sample, luminescence intensity, intensity quenching, quantum yield, etc. PL spectroscopy is recorded by two different approaches, i.e., by steady-state and by time-resolved PL measurement. Fig. (2.6) shows the schematic ray diagram of the spectrofluorometer, which can measure the PL. Here, the monochromatic light source of a fixed excitation wavelength strikes the specimen and the absorption process occurs.

After which, the re-emission of radiation is recorded by the photon detector through the combination of lenses. Finally, the signals are processed by the software and represented as a spectrum over the computer display. The spectrum is a plot between intensity and wavelength of the emitted radiation, which gives qualitative information about the materials.

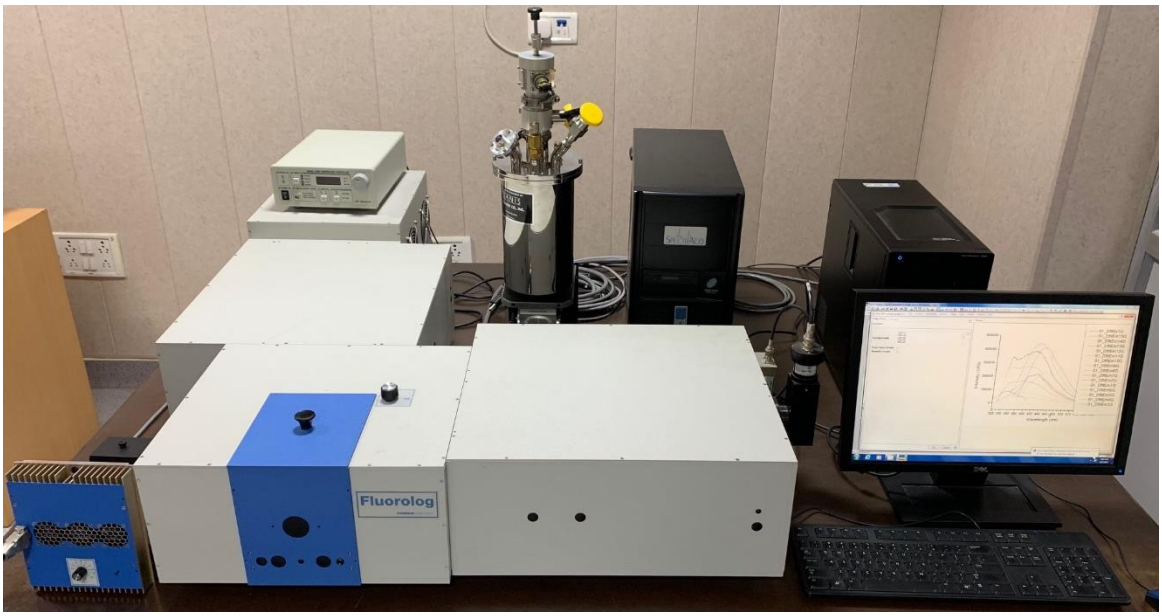

Figure 2.7. *Photograph of spectrofluorometer, Fluorolog-3, Horiba Jobin Yvon.*

The PL measurement was carried out with Horiba Jobin Yvon Fluorolog-3 spectrofluorometer equipped with double monochromators (grating 1200 lines/mm) at excitation and emission and a photomultiplier tube (PMT) detector. The 450-Watt Xenon lamp is used as a source with variable slit width from 0.5 nm to 5 nm (Fig. 2.7).

2.5 Time-correlated spectroscopy for photon counting (TCSPC)

It is advantageous for measuring the fluorescence lifetime in nano and sub-nano seconds [7–12]. TCSPC is a technique to count the time-correlated photons with the excitation pulse through time to amplitude converter (TAC). It uses either laser pulses or intense flash lamps of specific wavelengths to record time-dependent intensity profiles.

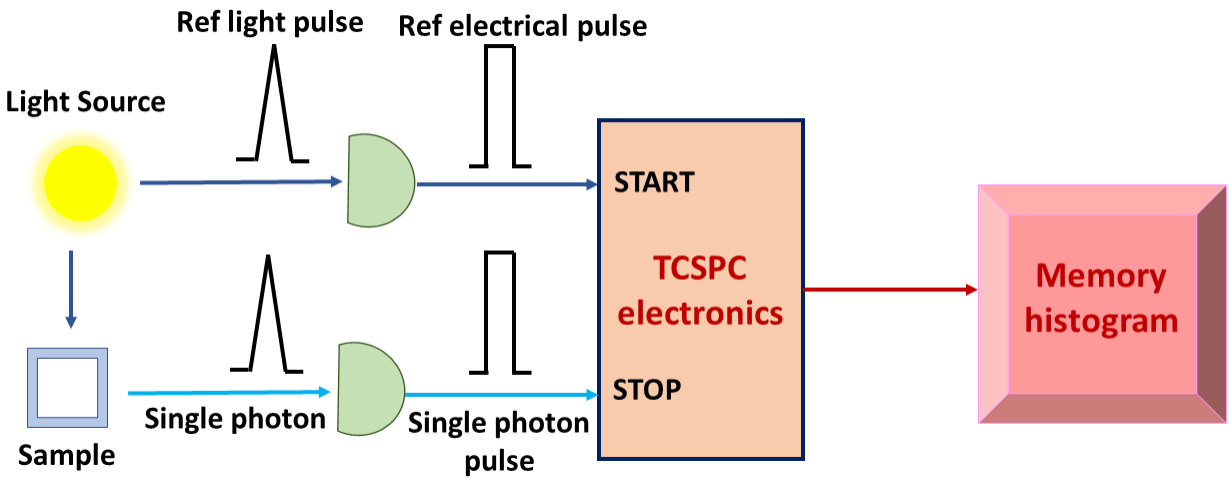

Figure 2.8. *Schematic representation of TCSPC.*

The TCSPC process involves the total time measurement from excitation of a specimen by laser light source and fluorescent photon (re-emitted radiation) to the PMT. The time correlation between the excitation and emission processes is done by a time-to-amplitude converter (TAC). Here, the timing capacitor is linearly charged from a constant current source after applying a start signal, at certain fixed delay and discontinued the charging by the applying a stop pulse, hence an output pulse is produced with amplitude. The start-stop process is represented in the histogram as increased memory value and the x-axis shows the time. The final plot demonstrates the plot between counts and channels, as shown in Fig. (2.8).

The plot represents the fluorescence decay of the sample and a single start-stop pulse obtains each point of the plot. A neutral density filter is used to minimize the attenuate excitation intensity, so the single-photon is recorded by 100 excitation pulses. With this rate, the 8000 pulses/second for excitation source of frequency 50 MHz. Typically, the 10000 counts are collected to maximize the signal-to-noise ratio. The instrument response function (IRF) was also measured, which is the intensity-time function of the laser pulse and is generated by Stokes or Rayleigh scattering of LUDOX at the excitation wavelength.

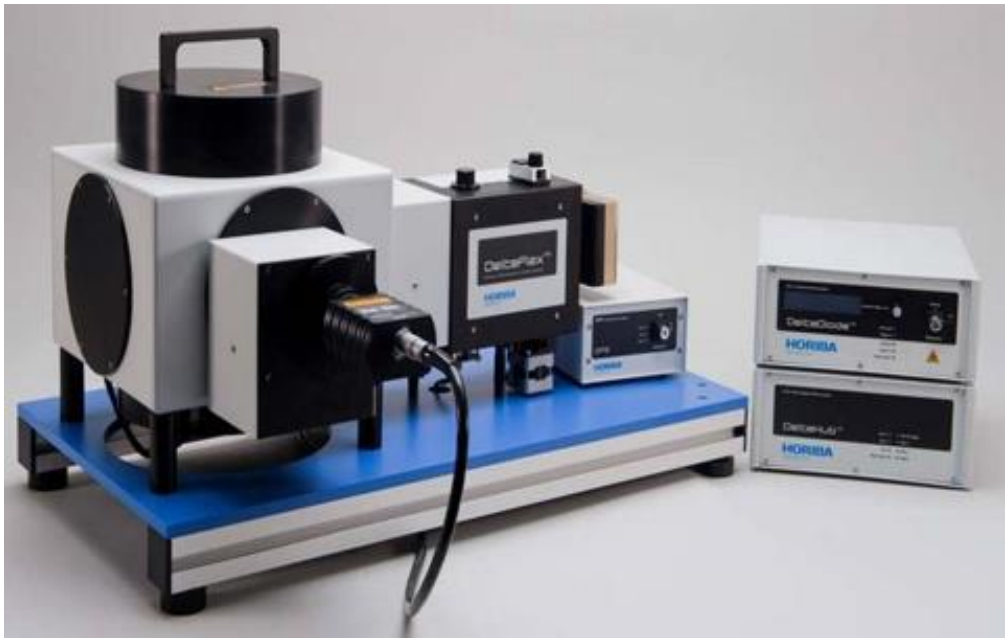

Figure 2.9. *DeltaFlex-01-DD TCSPC measurement unit.*

The fluorescence decay times were measured using DeltaFlex-01-DD, Horiba Jobin Yvon, equipped with delta diodes as pulse source and PPD.850 PMT for detection. All the data sets were optimized using the least square fitting method by the software provided by Horiba (Fig.2.9).

2.6 Fourier transform infrared spectroscopy (FTIR)

FTIR spectroscopy is a technique that involves the collection of high-resolution spectral data in the IR range. This comprise the correlation of transmission or absorption occurred in IR region and produces the information about the vibrational modes (i.e., the stretching and the bending vibrations to deliver the compositional analysis of the material) [13–15]. It is a specific compositional method to determine the unique fingerprinting of the molecular structures, which makes it vital for various analyses. The primary benefit of the IR spectroscopy is that it measures in a very wide range of the frequency, dislike other dispersive spectrometers, which have a limited range of intensity measurements.

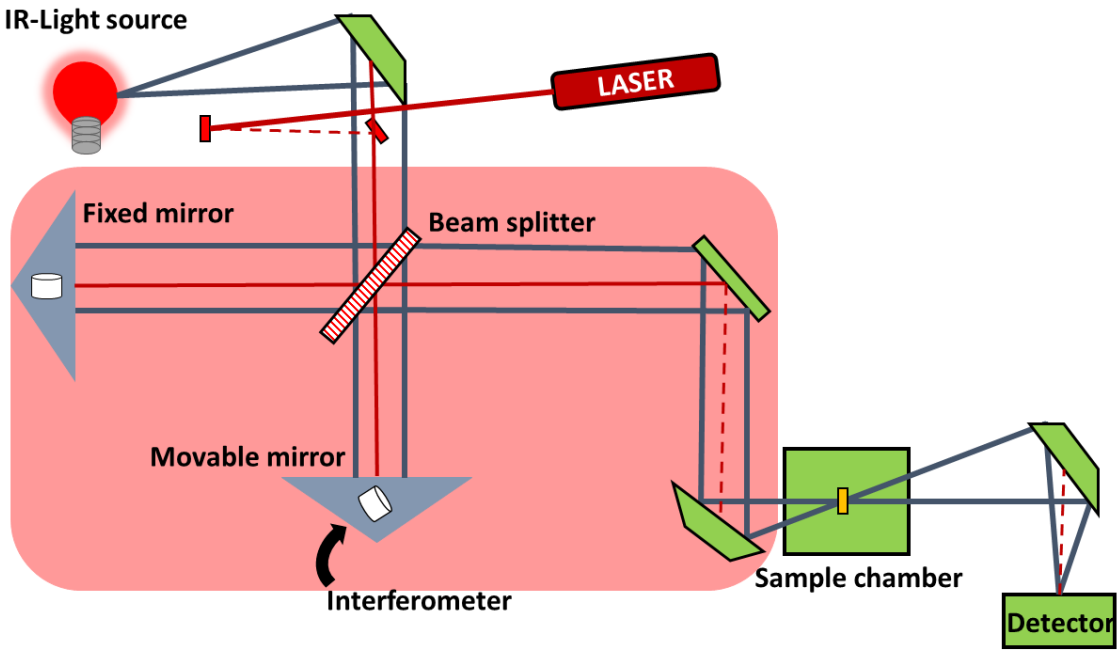

Figure 2.10. *Schematic ray diagram of FT-IR.*

The FTIR causes the IR beam to fall over the sample and record the amount of radiation absorbed or transmitted. The beam is then split into two separate frequencies to give a second data point, and this process is repeated multiple times to record the whole spectrum. The recorded data is analyzed on a computer for each data point. The FTIR spectrometry is based on the Michelson interferometer and can simultaneously process all the IR frequencies instead of processing one after the other. This makes it time-efficient to few seconds from several minutes. The schematic diagram of FTIR is shown in figure (2.10). In experiments, the FTIR spectra were

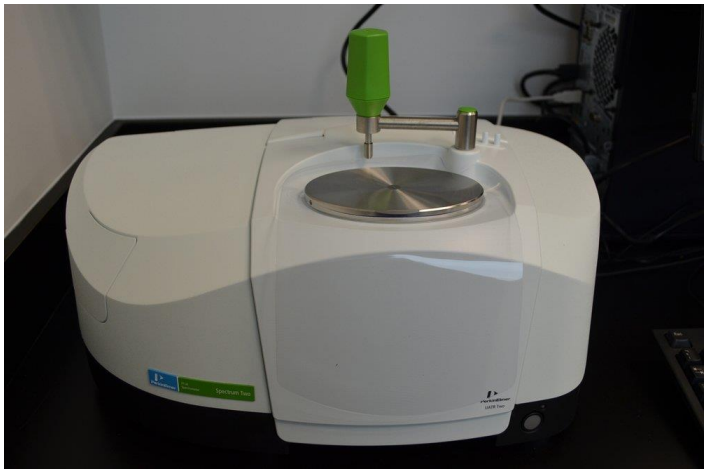

Figure 2.11. *Photograph of FTIR, Spectrum-II, Perkin Elmer*

recorded through spectrum (II) (Perkin Elmer) instrument, whereas the recording range would be 450 to 4000 cm^{-1} (Fig. 2.11).

2.7 Chemicals used

All chemicals used during the experiments were of the analytical grade received from Sigma Aldrich. As a molybdenum (Mo) source, sodium molybdate has been used, whereas thioacetamide (TAA) was used as the sulfur source. The 1,4-diaminobutane has been used for amine functionalization of QDs and as a capping agent. The salts for different metal analytes were employed during the experiments i.e., mercury chloride, lead (II) perchlorate, aluminium perchlorate nonahydrate, cadmium chloride hydrate, copper (II) chloride anhydrous, cobalt (II) perchlorate hexahydrate, zinc perchlorate hexahydrate, iron (III) perchlorate hydrate, iron (II) perchlorate tetrahydrate and nickel (II) perchlorate were obtained from Sigma Aldrich. The Pur-a-lyzer dialysis kit of pore size 1KDa was used from Sigma Aldrich.

2.8 Synthesis procedure of MoS_2 nanostructure

To synthesize MoS_2 nanostructures, several techniques have been acquired. Majorly, these synthesis techniques were categorized in two ways, i.e., top-down and bottom-up approaches, as discussed in Table (2.1).

In top-down techniques, the bulk semiconducting materials were broken into nano-sized particles using various techniques like mechanical exfoliation- ball-milling process, liquid-phase exfoliation, electrochemical exfoliation technique, etc. In comparison, the bottom-up approaches include the synthesis mechanism of building nanoparticles from more minor reagents by many techniques like chemical vapour deposition (CVD), pulsed laser deposition (PLD), hydrothermal/solvothermal method, sol-gel process, etc.

Category	Synthesis method	Phase	Morphology	Advantages	Disadvantage	Primary applications
Top-Down	Mechanical exfoliation	2H	Monolayer and few-layers	• High quality • Mild conditions	Low yield, random layer numbers	Study and device performance demonstration
	Liquid exfoliation	2H	Few layers	• High yield • scalable	Use of toxic solvents, surfactant residue, large size distribution	Energy storage, electronic devices
	Chemical exfoliation	1T/2H hybrid	monolayers	• High yield • Presence of defects for further functionalization	Use of flammable chemicals, phase conversion	Hydrogen evolution reaction, membrane materials
Bottom-up	Chemical vapour deposition (CVD)	2H	Mono and few layers	• Crystalline and high quality sample • Size and thickness control	High temp. required, potential leaking of toxic vapour (sulfur, H_2S)	Optoelectronics, sensors, electronics
	Hydrothermal/ solvothermal synthesis	1T/2H hybrid	Nanoflowers and nanotubes	• Scalable • High yield • Facile hybridization	Harsh conditions, aggregation into microscale structures	Catalysis, environmental adsorbents

Table 2.1. *Top-down and bottom-up approaches for the synthesis of MoS_2 nanostructures.*

The advantages of the bottom-up technique over the top-down approach are that it provides greater control over the shape, size and composition of the nanomaterials. The major drawback is the presence of numerous impurities. The various synthesis techniques of the MoS_2 nanostructures are listed in Fig. (2.12).

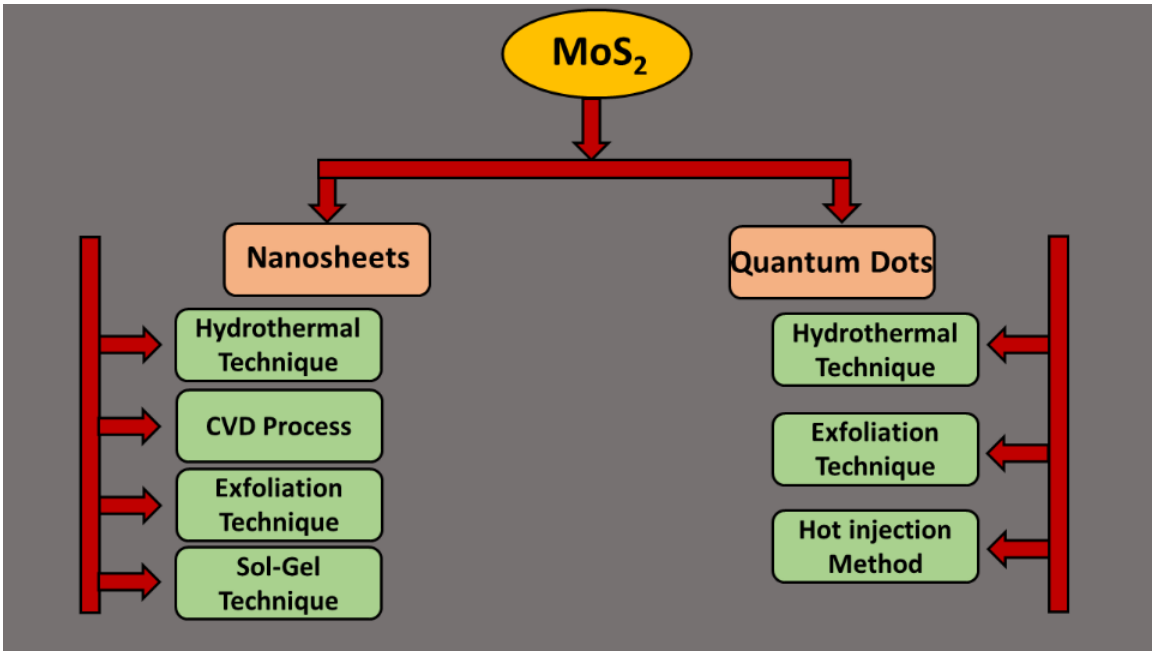

Figure 2.12. *Synthesis techniques of MoS_2 nanostructures.*

2.8.1 MoS_2 nanosheets synthesis process

A facile hydrothermal route has been opted to synthesize the MoS_2 nanosheets. Here, 1.0 g of ammonium hepta-molybdate tetrahydrate (AHM) and 0.5 g of citric acid were dissolved in 60 mL of de-ionized (DI) water for 1 h in an argon atmosphere. The citric acid helps the MoS_2 nanosheets to grow by reducing Mo (VI) to Mo (IV). Then, 1.2 g of thiourea is mixed into the solution, and the final solution is kept at 60 °C with stirring for another 1 h. After that, the solution is transferred to the Teflon-lined hydrothermal vessel (of capacity ~100 mL), treated at high temperature up to 200 °C for a day and permitted to cool naturally to room temperature. The obtained black precipitates were centrifuged at 5000 rpm for 20 min few times with DI and ethanol to remove the excess chelating agent and the unreacted precursors. Then, the precipitates were dried at 60 °C for 12 h in a hot air oven. To achieve highly crystalline MoS_2 nanosheets, the finally obtained black powder was annealed under the inert environment in a tubular furnace at 850 °C for 2 h.

2.8.2 MoS_2 quantum dots synthesis process

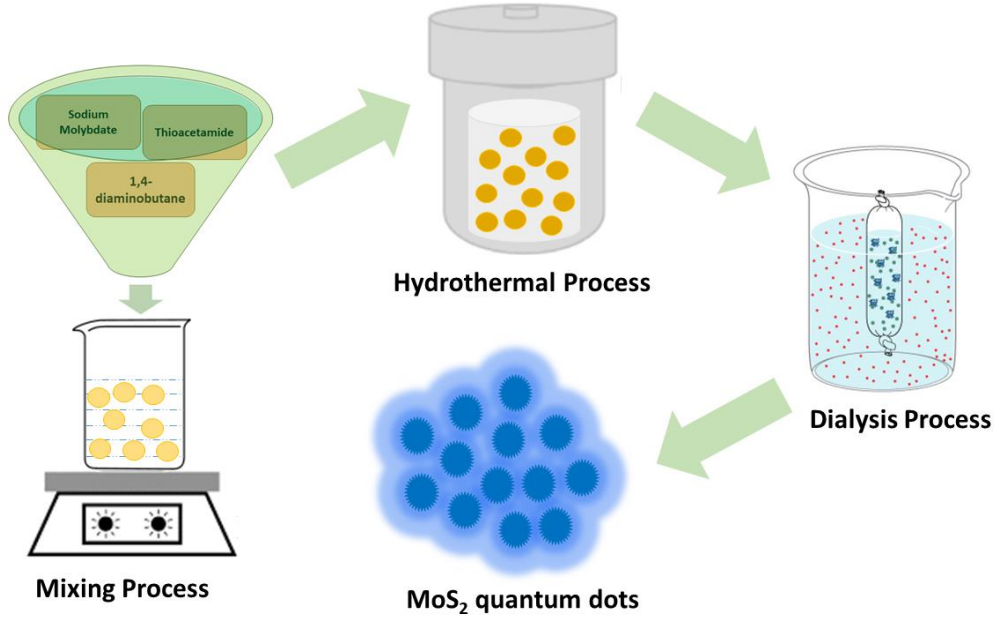

Figure 2.13. *Synthesis process of MoS_2 quantum dots.*

The preparation of MoS_2 QDs was conducted in a sealed Teflon-lined hydrothermal chamber. The facile route of synthesis involves the chemical reaction between the sodium molybdate and thioacetamide as the Mo and S sources, whereas the 1,4-diaminobutane (DAB) acts as capping agent as well as amine source for the functionalization of the QDs. To synthesize MoS_2 QDs, the 0.25 g of sodium molybdate was dissolved in ultrapure water (60 mL) and stirred for 10 min. Then, 0.5 ml of DAB was added to the mixture and stirred for 30 min in an inert atmosphere. Afterward, the 0.3g TAA was added to the mixture and the final solution was transferred to the Teflon vessel after stirring for 30 min. The Teflon line hydrothermal was kept at 200 ^oC for 24 h. The high pressure forming inside the chamber forced the reagent to react, and the formation of MoS_2 QDs takes place. The heterogeneous QDs were filtered out to remove larger particles, after allowing hydrothermal to cool down naturally. The filtered extract was then purified through a dialysis membrane (pore size ~1kDa) for 48 h and water

was changed in the interval of 2h. Then, the finally remained extract or the QDs were stored in glass vials and kept at 4 ^{o}C for further characterizations (Fig. 2.13) [16,17].

References

[1] L.H. Schwartz, J.B. Cohen, The Nature of Diffraction, in: Diffr. from Mater., Springer Berlin Heidelberg (1987), 46–76.

[2] B. D. Cullity, Elements of X-ray diffraction, J. Chem. Educ. 34 (1957), A178.

[3] F. Lin, Preparation and Characterization of Polymer TiO_2 nanocomposites via In-situ polymerization (2006).

[4] H.J. Jeon, S.C. Yi, S.G. Oh, Preparation and antibacterial effects of Ag-SiO_2 thin films by sol-gel method, Biomaterials. 24 (2003) 4921–4928.

[5] P. Whitfield, L. Mitchell, X-ray diffraction analysis of nanoparticles: Recent developments, potential problems and some solutions, Int. J. Nanosci. 3 (2004) 757–763.

[6] L.A. Bendersky, F.W. Gayle, Electron diffraction using transmission electron microscopy, J. Res. Natl. Inst. Stand. Technol. 106 (2001) 997–1012.

[7] I. Gregor, J. Enderlein, Time-resolved methods in biophysics. 3. Fluorescence lifetime correlation spectroscopy, Photochem. Photobiol. Sci. 6 (2007) 13–18.

[8] R.M. Ianniello, EAS 2004, November 15–18, Somerset, NJ, Appl. Spectrosc. 58 (2004) 123A-254A.

[9] M. Carrabba Spectroscopists' Calendar, Appl. Spectrosc. 58 (2004) 256A-257A.

[10] M. Köllner, J. Wolfrum, How many photons are necessary for fluorescence-lifetime measurements?, Chem. Phys. Lett. 200 (1992) 199–204.

[11] D. O'Connor, Time-correlated single photon counting - 1st Edition (1984), 9780323141444, 298.

[12] J. R. Lakowicz, Fluorophores, Principles of Fluorescence Spectroscopy, Springer US, (2006) 63–95..

[13] E. Knözinger, P. R. Griffiths, J. A. de Haseth: Fourier Transform Infrared Spectroscopy, Vol. 83 aus der Reihe: Chemical Analysis-A Series of Monographs of Analytical Chemistry and Its Applications, John Wiley + Sons, Chichester, New York, Brisbane, Toronto, Singapore, Berichte Der Bunsengesellschaft Für Phys. Chemie. 90 (1986) 1240–1241.

[14] C. N. Banwell, Fundamentals of molecular spectroscopy, McGraw-Hill, 2nd edition, (1972).

[15] H.H. Willard, J.L.L. Merritt, J.A. Dean, J.F.A. Settle, Instrumental methods of analysis, 7th edition, (1988).

[16] P. Sharma, M.S. Mehata, Colloidal MoS_2 quantum dots based optical sensor for detection of 2,4,6-TNP explosive in an aqueous medium, Opt. Mater. (Amst). 100 (2020) 109646.

[17] P. Sharma, M.S. Mehata, Rapid sensing of lead metal ions in an aqueous medium by MoS_2 quantum dots fluorescence turn-off, Mater. Res. Bull. 131 (2020) 110978.

CHAPTER 3

Synthesis of fluorescent MoS_2 QDs and their application in detection of 2,4,6-TNP explosive *

3.1 Introduction

Nowadays, chemical sensing for the quick detection of deleterious explosives, which have a lasting adverse effect on earthling, has been a great notion of research. It is a tenacious subject from the viewpoint of national security, human health and environmental fortification [1]. The sensing platform for 2,4,6-trinitrophenol (TNP) (picric acid) is important as it has superior explosive strength than 2,4,6-trinitrotoluene (TNT) [2]. Also, TNP acts as a notorious pollutant for the environment because of its great acidic behaviour and excellent solubility in water and could cause severe hazards to the agricultural land and aquatic life [3,4]. This is frequently used in the industrial sector to produce dyes, leather, glass and fireworks [5], which is a treacherous matter of fact, that a renowned toxic pollutant is continuously released in the surroundings throughout the manufacturing and consumption of the byproducts. Hence, intended to trace hidden explosives and environmental monitoring, the detection of TNP in soil and water holds a great significance [6].

Usually, a photo induced electron transfer (PET) mechanism is considered for explosive sensing because of the poor electron affinity but does not hold good for the selectivity [7]. In addition, nonradiative and radiative energy transfer (RET) mechanisms are also explored to enhance selective sensing of TNP.

* Part of this work has been published in **Optical Materials 100 (2020) 109646.**

The energy transfer (ET) system includes an excited fluorophore (donor), which transfers its energy into an acceptor through dipole-dipole interactions. Hence, the overall lifetime of donor entities will decrease [8,9]. Quantum dots (QDs) are usually preferred for TNP detection because of the alteration in photoemission colour by constraining the particle size [10-13]. The layered transition-metal dichalcogenide material (LTMD) *viz.*, molybdenum disulfide (MoS_2), has fascinated the research society because of its unique structure, catalytic and electronic properties [14–17]. Unlike MoS_2 nanosheets (NSs), its QDs comprise few layers with compact size and definite shape exhibit excellent fluorescence, electrochemical, catalytic and photocatalytic properties because of the quantum confinement and the edge effects. Among all the 0-D materials, MoS_2 QDs has been confirmed as a potential sensing platform for gas sensing, chemical sensing, biosensing, bioimaging, etc. [18-20].

In this study, amine-functionalized fluorescent MoS_2 QDs have been prepared through a simple and eco-friendly hydrothermal method, which was further used for effective detection of TNP (considered as an explosive and a toxic) in aqueous media. The quenching of PL of QDs as a function of TNP concentrations has been recorded and analyzed.

3.2 Materials and method

Sodium molybdate, thioacetamide (TAA), diaminobutane (DAB) and 1KDa Pur-a-lyzer dialysis kit were acquired from Sigma-Aldrich. To synthesize the DAB-capped MoS_2 QDs, the bottom-up approach was attained for which 50 mg of sodium molybdate is dissolved in 40 ml de-ionized (DI) water in an inert environment. Then 1 ml of DAB is added to the solution and kept at 50 ºC for 1h. Afterward, TAA was added as a sulfur source to the above mixture and left for another 0.5h. The pH of the above mixture was maintained at 7 using a buffer solution. Finally, the resultant mixture was transferred to the 100 ml Teflon lined autoclave, which was

kept in an electric oven at 200 ^{o}C for 24 h then left to cool down naturally, shown in Fig. 3.1. Thereafter, the synthesized nanodots were dialyzed using 1KDa Pur-a-lyzer dialysis kit for 48 h, with the surrounding water being changed after every two hours.

To prepare the MoS_2 QDs incorporated polyvinyl alcohol (PVA) films for the measurement of low temperature-dependent (TD) PL, 0.5 gm of PVA was dissolved in 10 ml of DI and DI+QDs (9:1). The mixture was stirred for 4 h at room temperature and then transferred to a petri dish to settle homogeneously all over its surface. Then the petri dish was kept at 60 ^{o}C in an oven to dry for 8 h. Finally, the plain PVA and PVA+QDs films were retrieved.

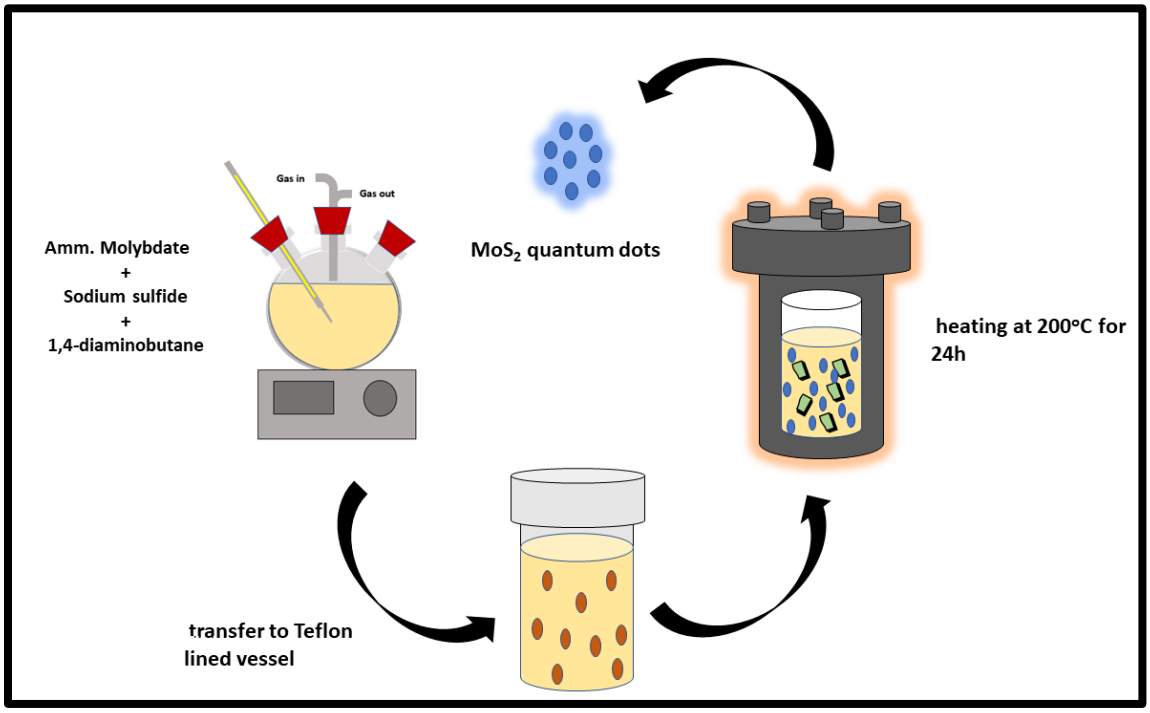

Figure 3.1. *The schematic mechanism for preparation of MoS_2 QDs in water.*

3.3 Characterization Techniques

High resolution-transmission electron microscopy (HR-TEM) images were recorded by TALOS (Thermo scientific instruments) with an accelerating voltage of 200kV. The Fourier

transform infrared spectroscopy (FT-IR) was recorded on Spectrum II (Perkin Elmer) ranging from 450 to 4000 cm^{-1}. The absorption spectra were recorded with a spectrophotometer, Lambda 750 (Perkin Elmer) and the photoluminescence (PL) spectra were recorded on a spectrofluorometer, Fluorolog-3 (Horiba Jobin Yvon) equipped with a 450 W xenon lamp. The PL lifetimes were recorded on a time co-related single-photon counting (TCSPC) system, DeltaFlex-01-DD (Horiba Jobin Yvon, IBH Ltd.) equipped with PMT (PPD 850) detector and 340 nm delta diode as the excitation source [21].

3.4 Results and discussion

3.4.1 High-resolution transmission electron microscope (HR-TEM) images

The high-resolution images of MoS_2 QDs were recorded by HR-TEM. Fig. 3.2 illustrates the HR-TEM images of MoS_2 QDs having non-uniform spherical architectures with size ranges from 3-4 nm. The HR-TEM image shows the formation of crystalline MoS_2 with paralleled and ordered lattice fringes. The lattice d-spacing of the as-synthesized MoS_2 QDs estimated to be 2.2 Å, corresponding to (103) faces.

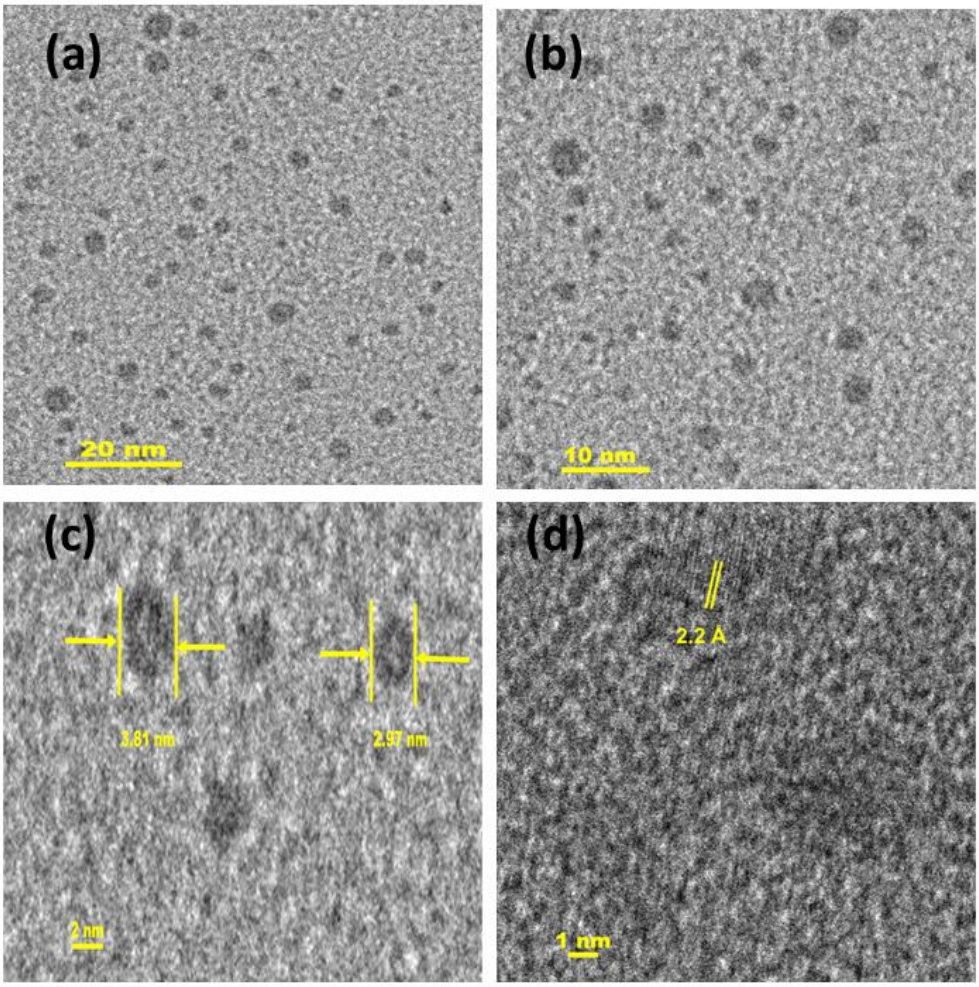

Figure 3.2. *HR-TEM images of MoS_2 quantum dots dispersed in water.*

3.4.2 Fourier transform infrared (FTIR) spectra

Fig. 3.3 shows the FT-IR spectrum of amine-functionalized MoS_2 QDs. The vibrational peak at 3315 cm^{-1} illustrates the N-H stretching vibrations and the peak at 1630 cm^{-1} indicates N-H bending and in-plane stretching. The weak band observed at 467 cm^{-1} arises due to Mo-S stretching vibration [21].

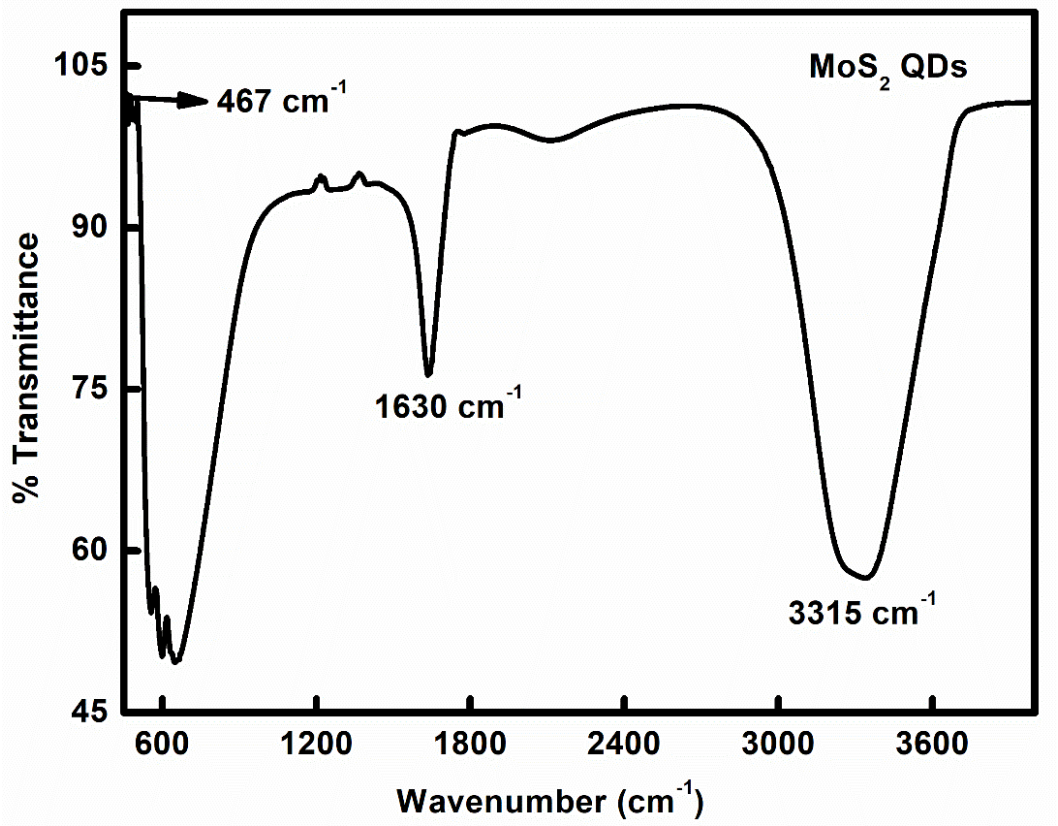

Figure 3.3. *FT-IR spectrum of MoS_2 QDs dispersed in water.*

3.4.3 UV-visible absorption and photoluminescence spectra

Fig. 3.4 shows the absorption spectrum of MoS_2 QDs dispersed in water. Two absorption bands were noticed at 275 and 335 nm, which arise due to transitions from the deep valence band to the conduction bands.

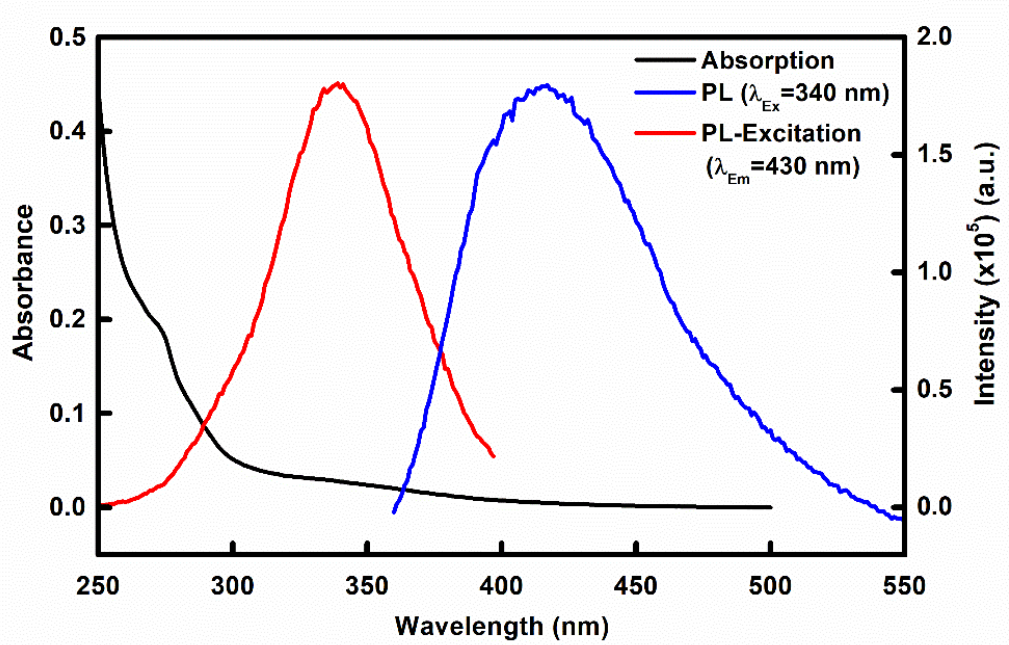

Figure 3.4. *The absorption, PL and PL-excitation spectra of MoS_2 QDs dispersed in water.*

The optical band-gap of MoS_2 QDs calculated from Tauc's plot comes out to be 4.56 eV, as shown in Fig. 3.5. The band-gap energy (E_g) of MoS_2 QDs was calculated from a well-established equation:

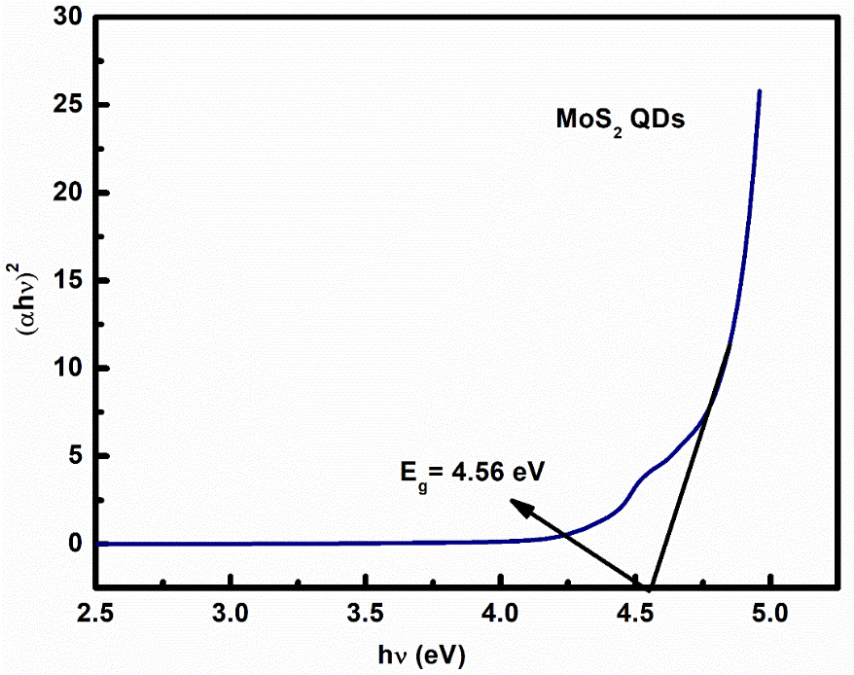

Figure 3.5. *The Tauc's plot obtained from the absorption of MoS2 QDs.*

$$\boldsymbol{\alpha h\nu = A(h\nu - E_g)^n} \quad \textbf{(3.1)}$$

where A is the constant, α is the absorption coefficient, I_o is the input intensity, I is the transmitted intensity, $h\nu$ be the photon energy and n are the constant (n = 1/2 for direct semiconductor) and L is the path length. The variation in $(\alpha h\nu)^2$ with the photon energy $h\nu$ allows calculating the band-gap energy [22]. The tangent around the band edge was extrapolated to find the $E_{g.}$ As predicted, the value of band-gap energy (Eg) outdoes the bulk MoS_2 (~1.2eV). The PL spectrum (Fig. 3.4) peaked at 430 nm when excited with 340 nm wavelength and the corresponding PL-excitation spectrum (blue spectrum) peaked at 340 nm. Further, the as-synthesized MoS_2 QDs exhibit the excitation dependence PL (Fig. 3.6). With an increase in excitation wavelength from 260 to 400 nm, the PL spectrum of MoS_2 gradually shifts towards the longer wavelength region.

Moreover, the PL-excitation spectrum also shifted towards red (by ~25 nm) while increasing the monitored PL wavelength (Fig. 3.6). The variation in excitation spectra is observed while varying the PL peaks from 400 to 460 nm wavelengths. The change observed was quite evident as it changed almost 25 nm of wavelength.

These different peaks may arise from the recombination of electron-hole pairs at varying energy levels due to the surface states. The estimated quantum yield of the amine-functionalized MoS_2 QDs is ~8 %.

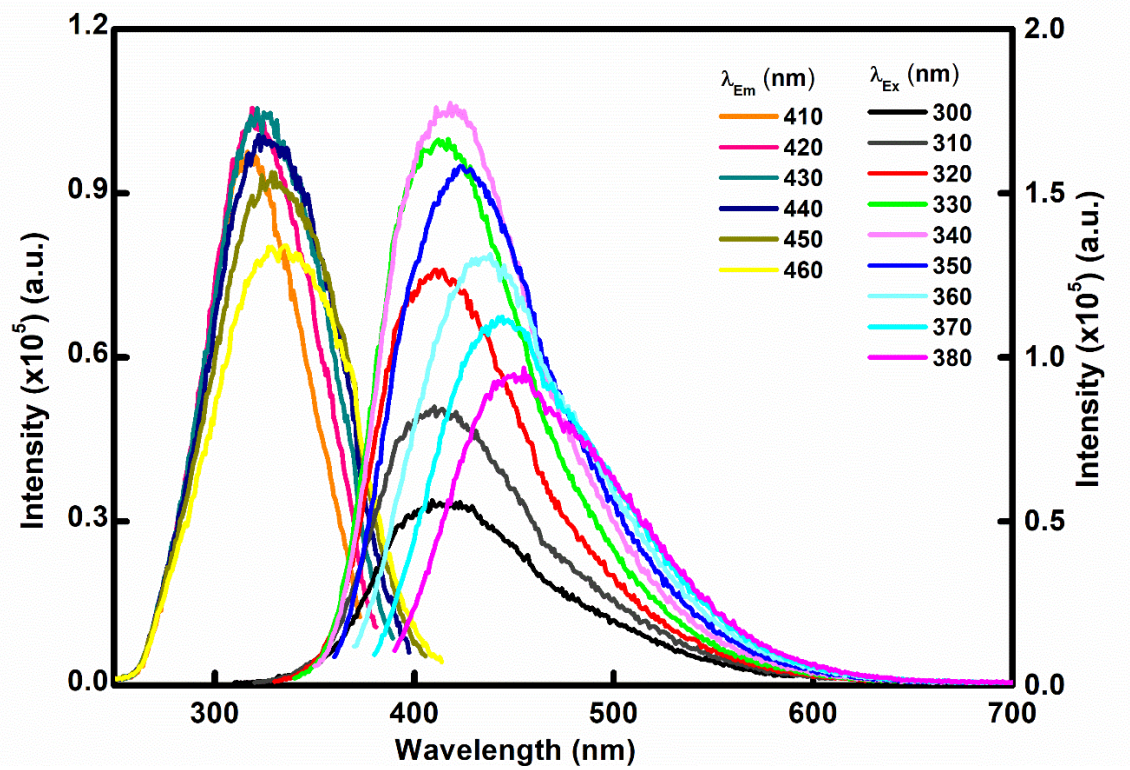

Figure 3.6. *The PL spectra at different excitation wavelengths and the PL-excitation spectra at different PL wavelengths of MoS_2 QDs dispersed in water.*

3.4.4 Time-resolved spectroscopy (PL lifetimes)

Fig. 3.7 illustrates the PL decay profiles of colloidal MoS_2 QDs collected across the PL wavelength at the fixed excitation wavelength (340 nm). The obtained PL decays are well reproduced with triexponential function ($I(t) = \alpha_1 e^{(-t/\tau_1)} + \alpha_2 e^{(-t/\tau_2)} + \alpha_3 e^{(-t/\tau_3)}$), where α_i describes the pre-exponential factors and τ_i represents the lifetimes, as mono and bi-exponential functions could not give reasonable fitting. All three lifetimes increase with increasing monitored wavelength, e.g., τ_1 varies from 0.29 to 0.39 ns, τ_2 from 2.25 to 2.86 ns and τ_3 from 8.45 to 9.76 ns. However, the corresponding pre-exponential factors, α_2 and α_3 increase whereas α_1 decreases.

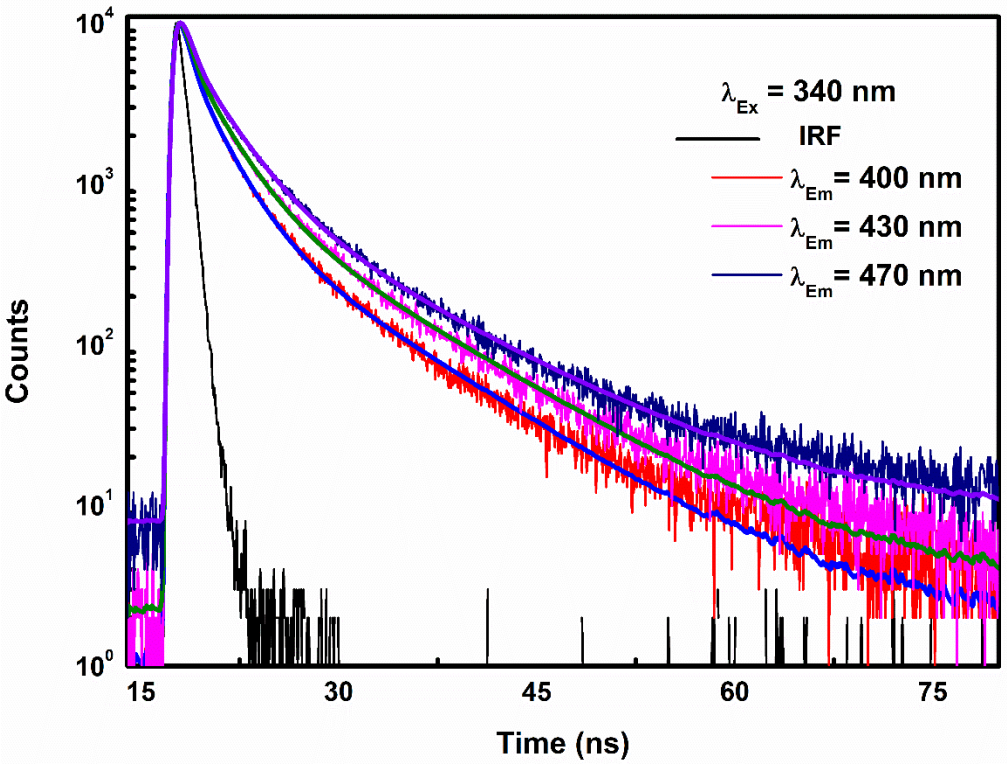

Figure 3.7. *The fitted photoluminescence decay curves of MoS_2 QDs dispersed in water. The excitation wavelength was 340 nm.*

The observed lifetime and corresponding amplitude at the red edge of the PL band indicates that the shortest component comes from the band edge PL whereas the longer one comes from the surface states. The average lifetime ($\tau_{av} = \sum \alpha_i \tau_i^2 \; / \; \sum(\alpha_i \tau_i)$) follows the same trend, i.e., increase in the lifetime with increasing PL wavelength. Thus, the prepared QDs may have edge defects, resulting in an increase in τ_{av} at the red edge of the PL band.

3.4.5 Low-temperature photoluminescence

The temperature-dependent PL of MoS_2 QDs incorporated in PVA were recorded in the range of 300 to 100 K, and the observed results are shown in Fig. 3.8. With lowing temperature caused an explicit increase in the PL intensity and became maximum at 100 K.

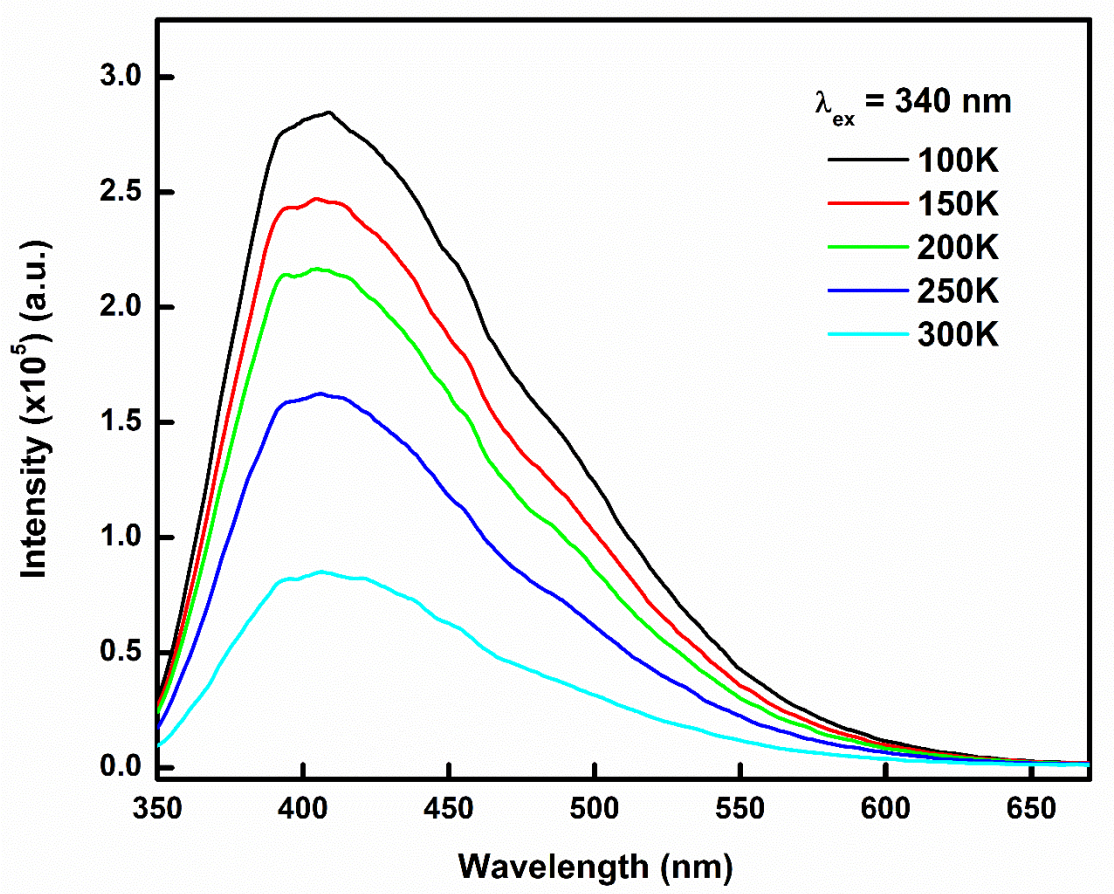

Figure 3.8. *The temperature-dependent PL spectra of MoS_2 QDs incorporated in PVA film.*

The rise in intensity at low temperature originates, due to increase in ground state population of the charge carriers as compared to the PL at room temperature. Fig. 3.9 (a-e) illustrates the TD-PL contour maps of temp. ranging from 300K to 100K, of the MoS_2 QDs incorporated in PVA at different excitation wavelengths. The QDs were excited from wavelength of 280 to 360 nm and illustrated the 3D-coloured representation of PL intensities. The counter maps indicated the variation in PL with the excitation wavelengths. The red elliptical area demonstrates the maximum PL intensity, which ranges from 390 to 430 nm, obtained when excited with the wavelengths from 330 to 360 nm. No new PL peak has been observed at low temperature study of the MoS_2 QDs.

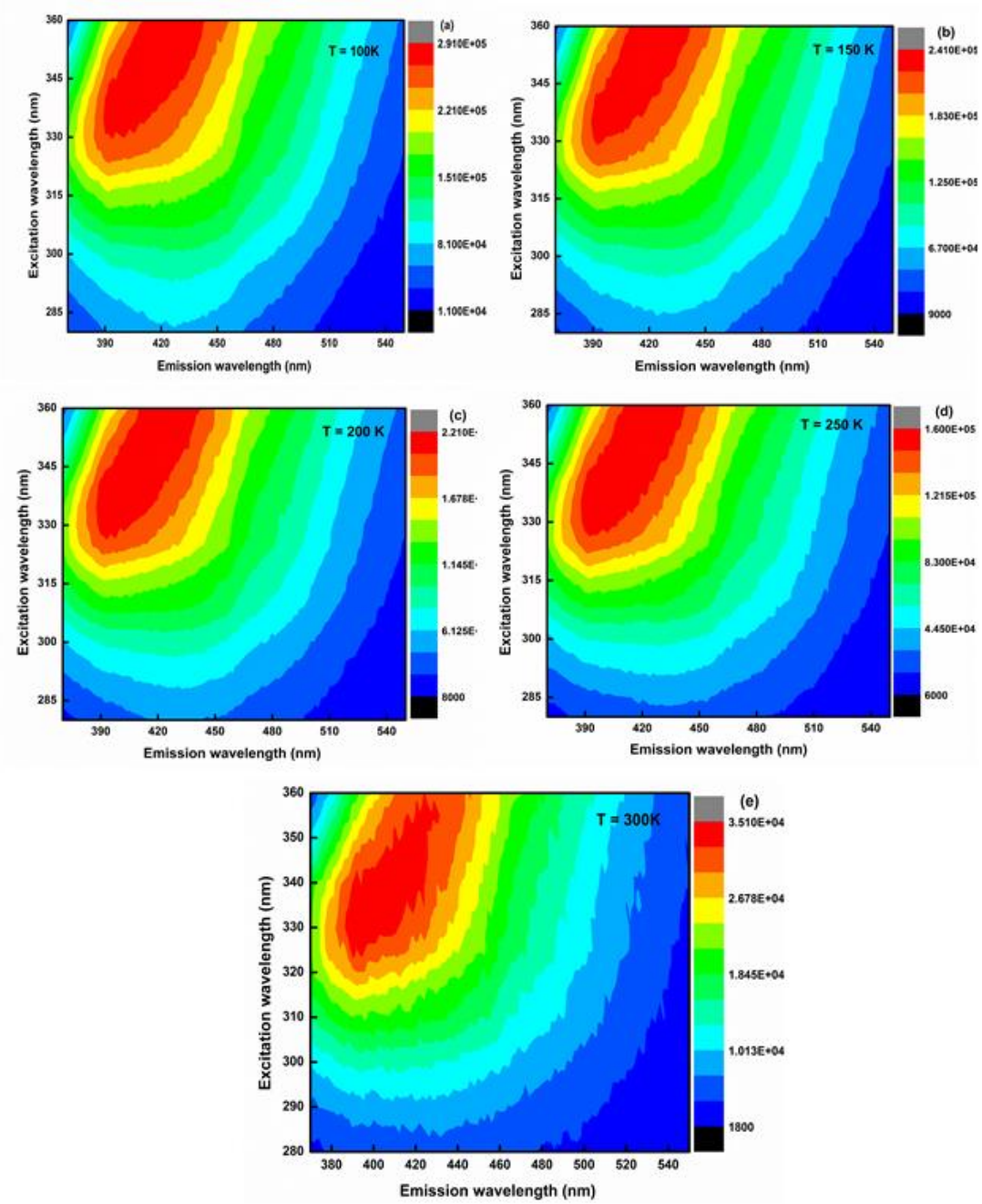

Figure 3.9. *The PL contour maps of MoS_2 QDs (a, b, c, d and e) were obtained at 100, 150, 200, 250, 300 K. The excitation wavelengths were 280 to 360 nm.*

3.4.6 PL quenching of MoS_2 QDs by TNP

Furthermore, the PL of MoS_2 QDs quenched in the presence of a small amount of TNP explosive poured into the cuvette. The substantial quenching in PL of MoS_2 QDs was observed

by adding 3 μM concentration of TNP (Fig. 3.10). After adding up to 20 μM concentration of TNP, the PL intensity of the MoS_2 QDs was quenched to 60% to the initial intensity.

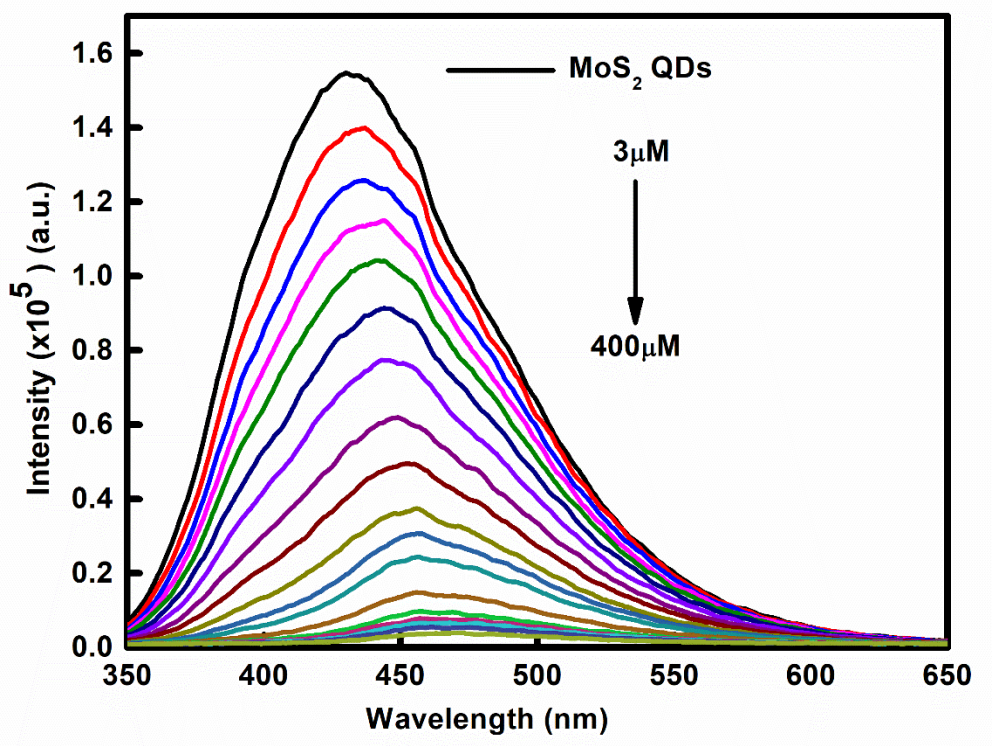

Figure 3.10. *PL spectra of MoS_2 QDs with the addition of different concentrations of TNP. The excitation wavelength was 340 nm.*

When the TNP concentration is continued to increase upto 400 μM, the PL intensity of QDs gradually quenches to 98% and the PL peak shifts and finally reached the PL of TNP, which is appeared at 465 nm (Fig. 3.11). With the increase in TNP concentration, a redshift in PL was observed (Fig. 3.10), might be due to the dominance of the PL of TNP. The absorption, PL and PL-excitation spectra of TNP were shown in Fig. 3.11.

The well-known Stern-Volmer (S-V) relation (Eq. 3.2) was plotted for the quenching of PL intensity of MoS_2 QDs in the presence of various concentrations of trinitrophenol [23].

$$\boldsymbol{I_0/I \;=\; 1 + \; K_{SV}\,[TNP]} \qquad \textbf{(3.2)}$$

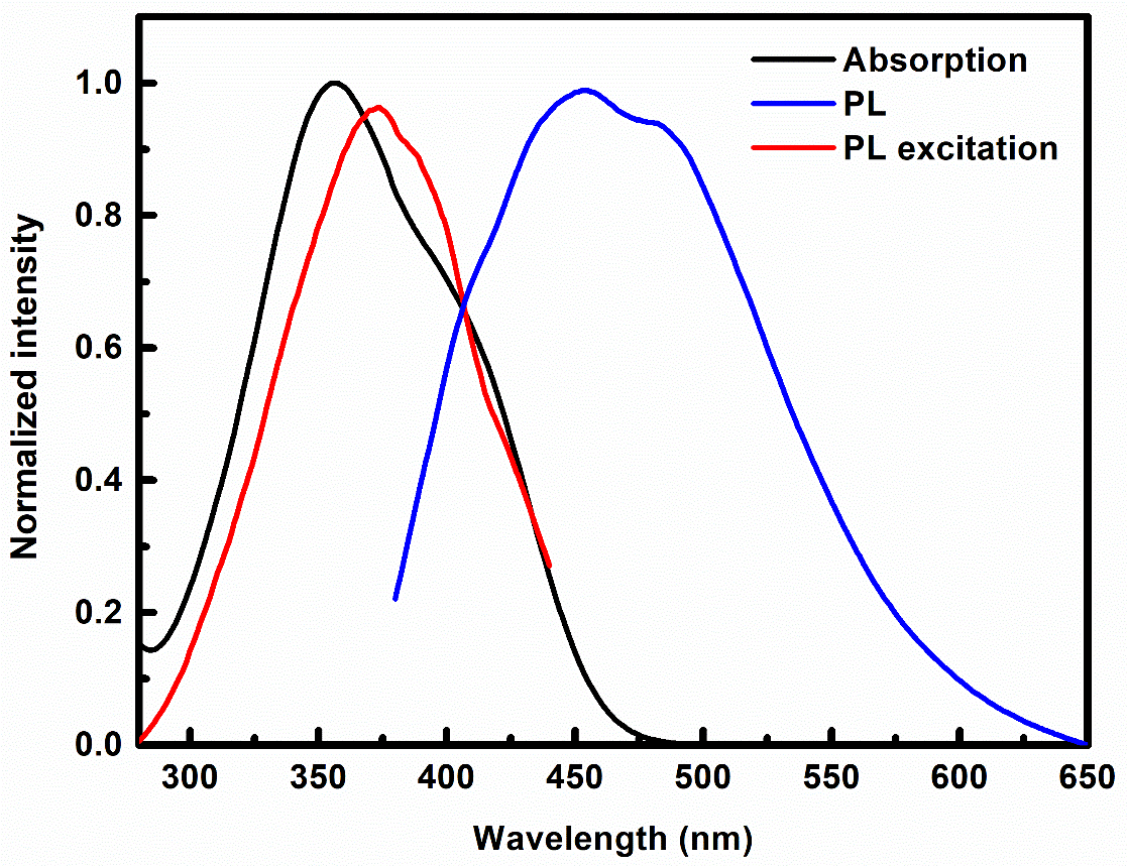

Figure 3.11. *The normalized absorption, PL (λ_{ex}= 367 nm) and PL-excitation (λ_{em}= 465 nm) spectra of TNP in water.*

Where I and I_0 are PL intensities of MoS_2 QDs with and without the quencher (TNP), respectively and K_{SV} is the S-V constant, calculated from the linear relation of S-V plot shown in Fig. 3.12 and comes out to be 0.31 x 10^6 M^{-1}. The quenching rate constant K_q, determined by Eq. ($K_{SV} = K_q\tau_0$) is comes out to be 7.78 × 10^{11} $M^{-1}S^{-1}$, where τ_0 is the lifetime of MoS_2 QDs in the absence of quencher.

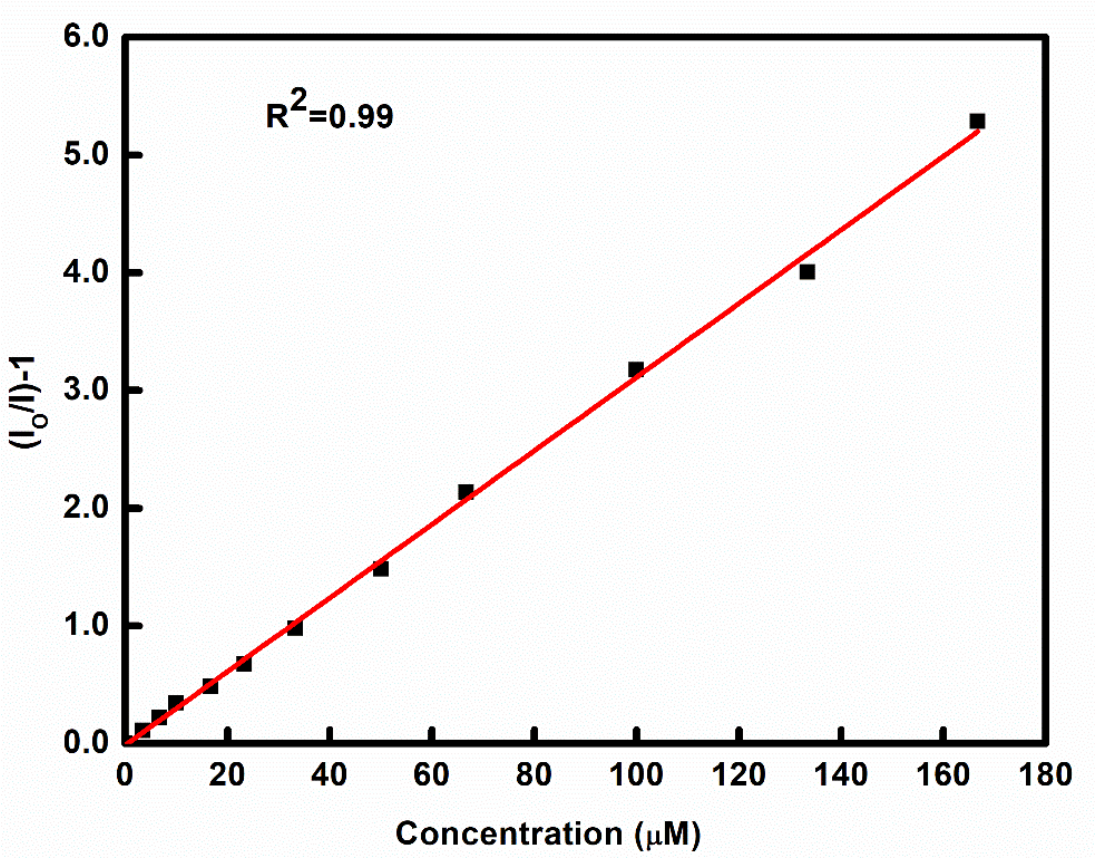

Figure 3.12. *The Stern-Volmer plot between relative PL intensity of MoS_2 QDs and TNP.*

The limit of detection (LOD) for the selectively detected nitro explosive TNP is 5.3×10^{-6} M. To report the selectivity of TNP among other nitro explosives, 2,6-dinitrotoluene (2,6-DNT), 2-nitrotoluene (2-NT) and 4-nitrotoluene (4-NT) were also studied. These compounds could not outperform as TNP, demonstrated in Fig. 3.13 at a particular concentration of the nitro compounds, whereas Fig. 3.14 presents the 3-D plot for the different nitro compounds at variable concentrations. Thus, it has been concluded that MoS_2 QDs shows selective sensing of TNP over other nitro compounds.

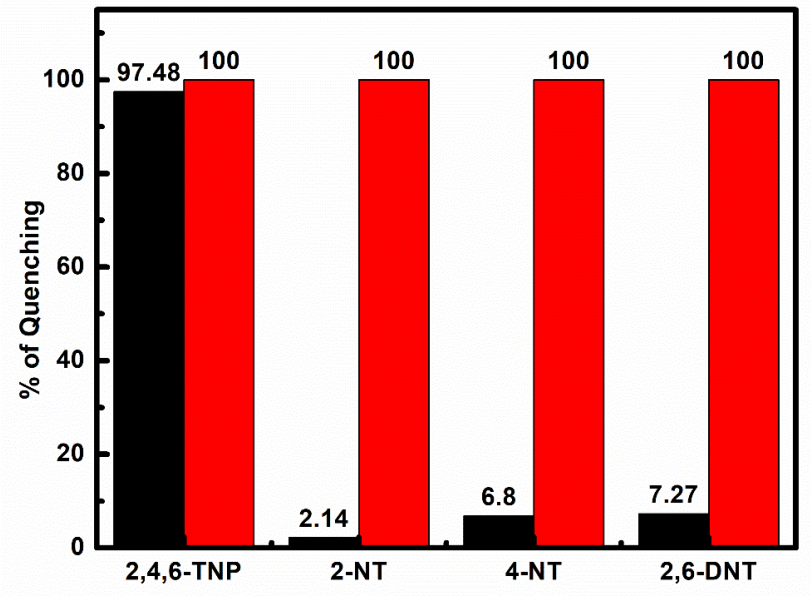

Figure 3.13. *Bar diagram of PL intensity of MoS_2 QDs at a particular concentration of various nitro-explosives.*

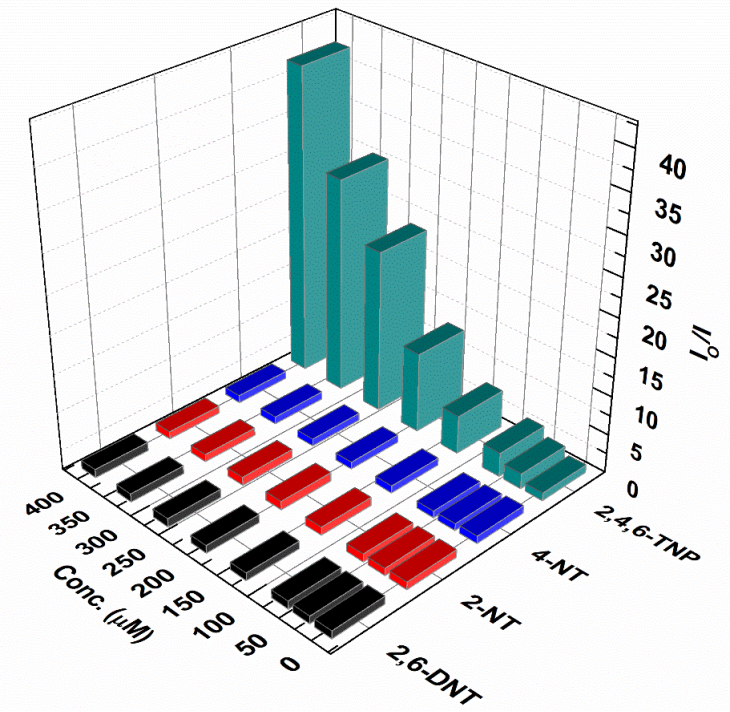

Figure 3.14. *Bar diagram of PL intensity of MoS_2 QDs with varying concentrations of various nitro-explosives.*

3.4.7 Energy transfer mechanism

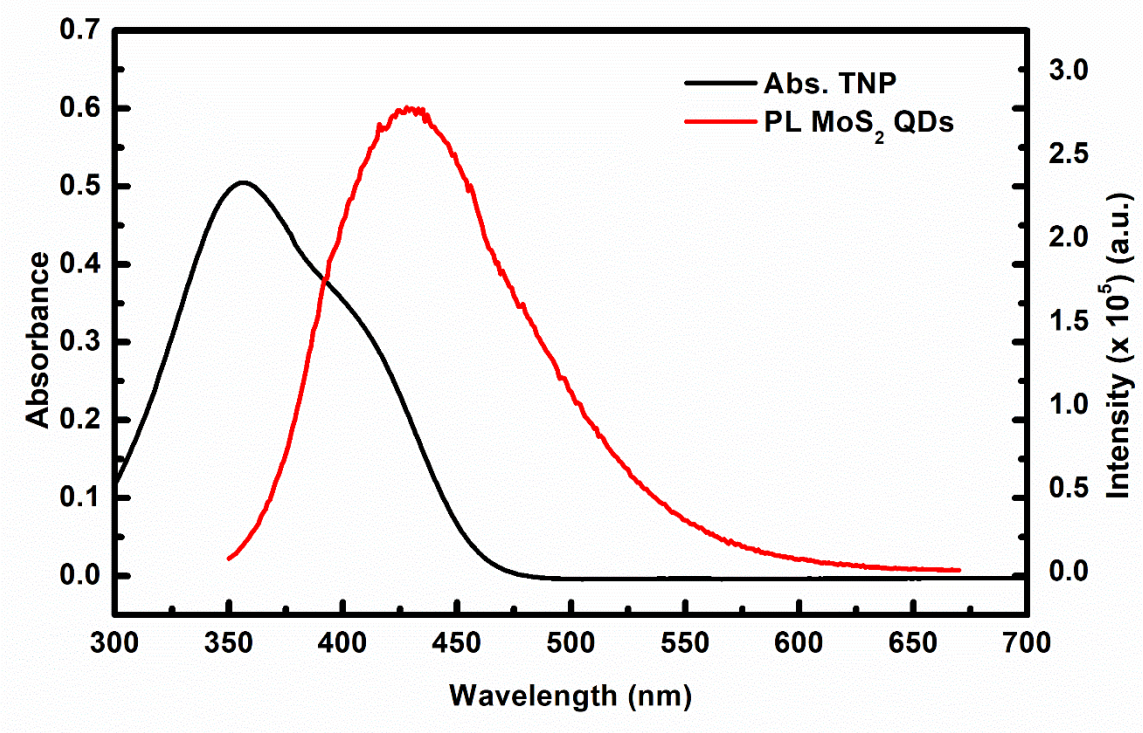

Figure 3.15. *The spectral overlap of the absorption spectrum of TNP and PL spectrum of MoS_2 QDs in water.*

Further, there is significant overlapping between the PL spectrum of MoS_2 and the absorption spectrum of TNP (Fig. 3.15), indicating the possibility of the energy transfer process.

The amine capped MoS_2 quantum dots (QDs) possess high electron affinity because of the electron-rich -NH_2 group around the QDs. In the presence of nitro groups presence on TNP, there are strong electrostatic interactions between them and causes an instant electron transfer between the donor (QDs) and acceptor (TNP). This process is similar to resonance electron transfer (RET) due to energy transfer to the acceptor, which also depends on the spectral overlap of emission of donor and absorbance of the acceptor (shown in Fig. 3.15) like RET. In Fig. 3.15, the PL peak for MoS_2 arises at 430 nm, whereas the absorbance peak of TNP observed at 355 nm shows a significant overlap. As the PL of the QDs is decreased, the plot

of the rate of energy transfer (K_T) as a function of TNP concentration is nearly linear (Fig. 3.16).

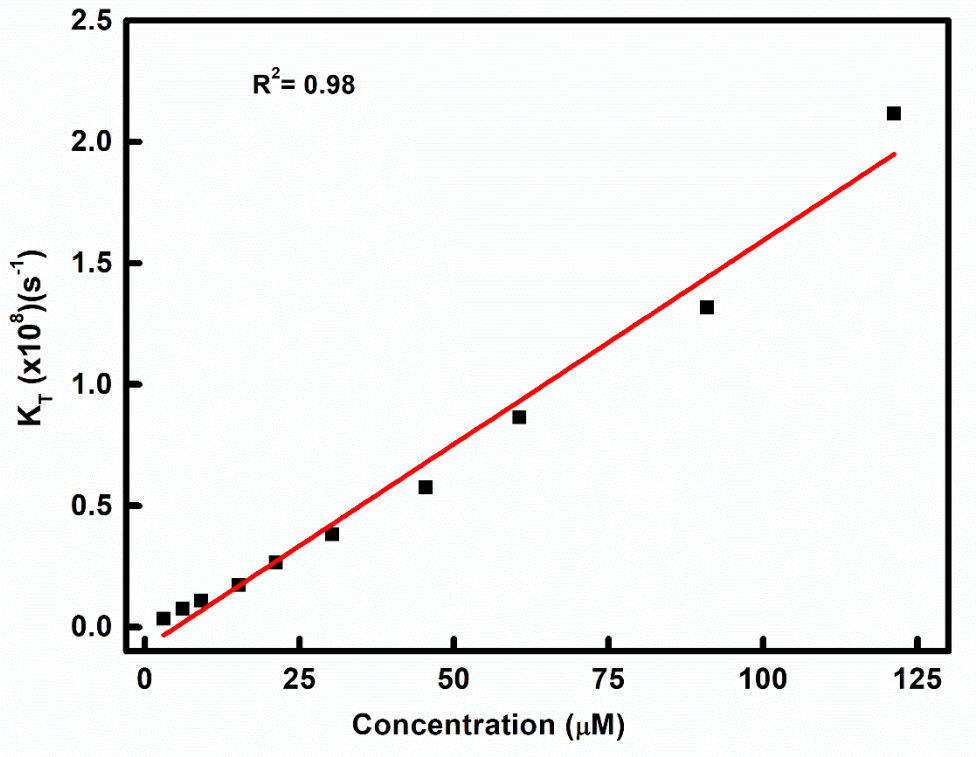

Figure 3.16. *A plot between the rate of energy transfer (K_T) as a function of the concentration of TNP.*

The spectral overlap integral J(λ), represented by an equation ($J(\lambda)=\int_{\infty}^{0} F_D(\lambda)\varepsilon_A(\lambda)\lambda^4 d\lambda$) is calculated to be $1.35719\times10^{17} nm^4 M^{-1} cm^{-1}$. Where $F_D(\lambda)$ represents the corrected donor fluorescence intensity, $\varepsilon_A(\lambda)$ represents the acceptor's extinction coefficient at λ. The Förster distance or critical distance (R_0) is the distance at which the FRET efficiency is 50% and could be calculated from Eq. ($R_0 = \frac{9(ln10)k^2\Phi_D}{128\pi^5 N n^4}[J(\lambda)]$) where, k^2 represents the orientation of dipoles interactions, Φ_D represents the quantum yield of donor, N and n represents the Avogadro's number and refractive index of the medium, respectively [24]. The R_0 was calculated to be 28

Å. The efficiency of energy transfer (E%) can be defined by Eq. ($E = 1 - \frac{F_{DA}}{F_D}$) where, F_{DA} and F_D are fluorescence intensity of donor in presence and in absence of acceptor respectively. The efficiency depends on distance (r_{DA}) between the donor and the acceptor, which can be represented by Eq. (${r_{DA}}^6 = \frac{{R_0}^6[1-E]}{E}$).

The steady-state fluorescence results show a gradual increase in E% with the increase in TNP concentration and the r_{DA} are represented in Figs. 3.17 and 3.18, respectively. The rate of energy transfer or the resonance energy transfer rate (K_T) is given by, $\boldsymbol{K_T = \frac{1}{\tau_D}(\frac{R_0}{r_{DA}})^6}$ where, $\boldsymbol{\tau_D}$ is the lifetime of the donor in the absence of the acceptor.

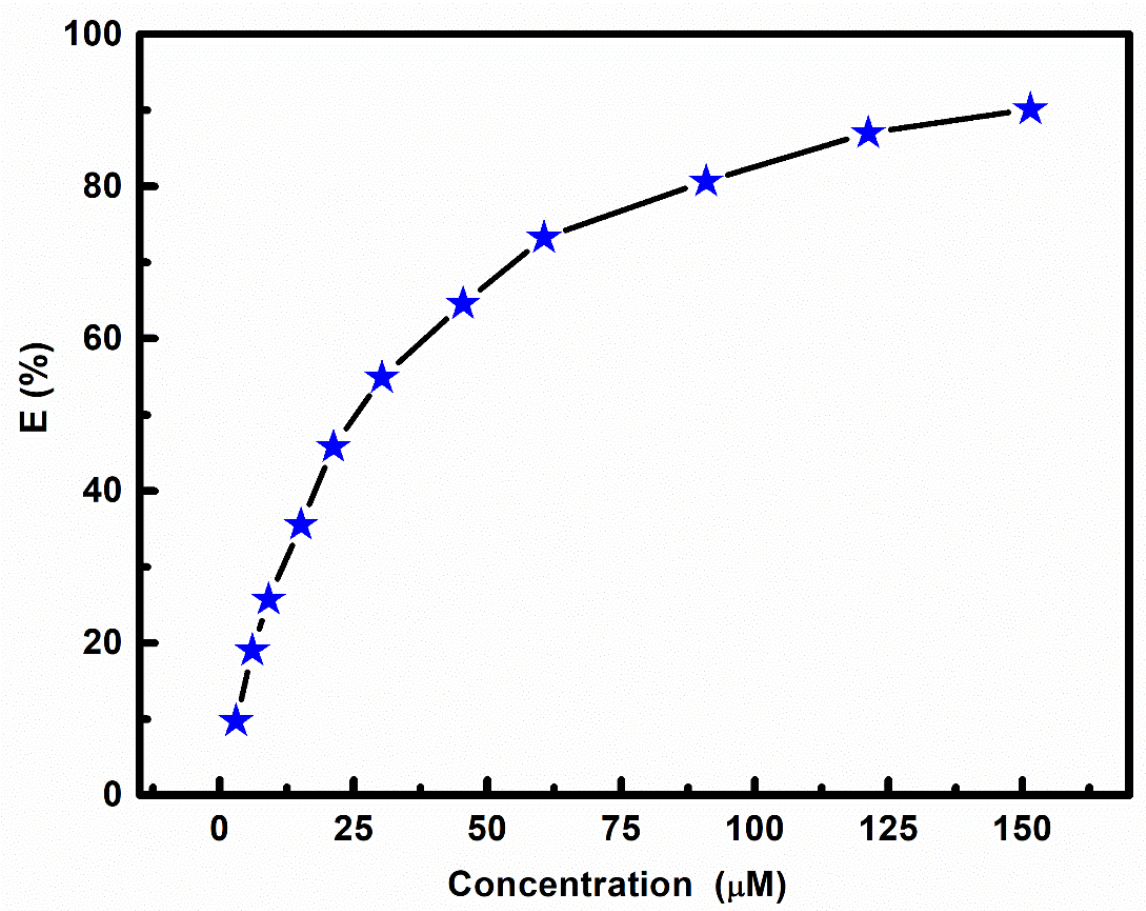

Figure 3.17. *A plot between efficiency of energy transfer (E) and concentration of TNP.*

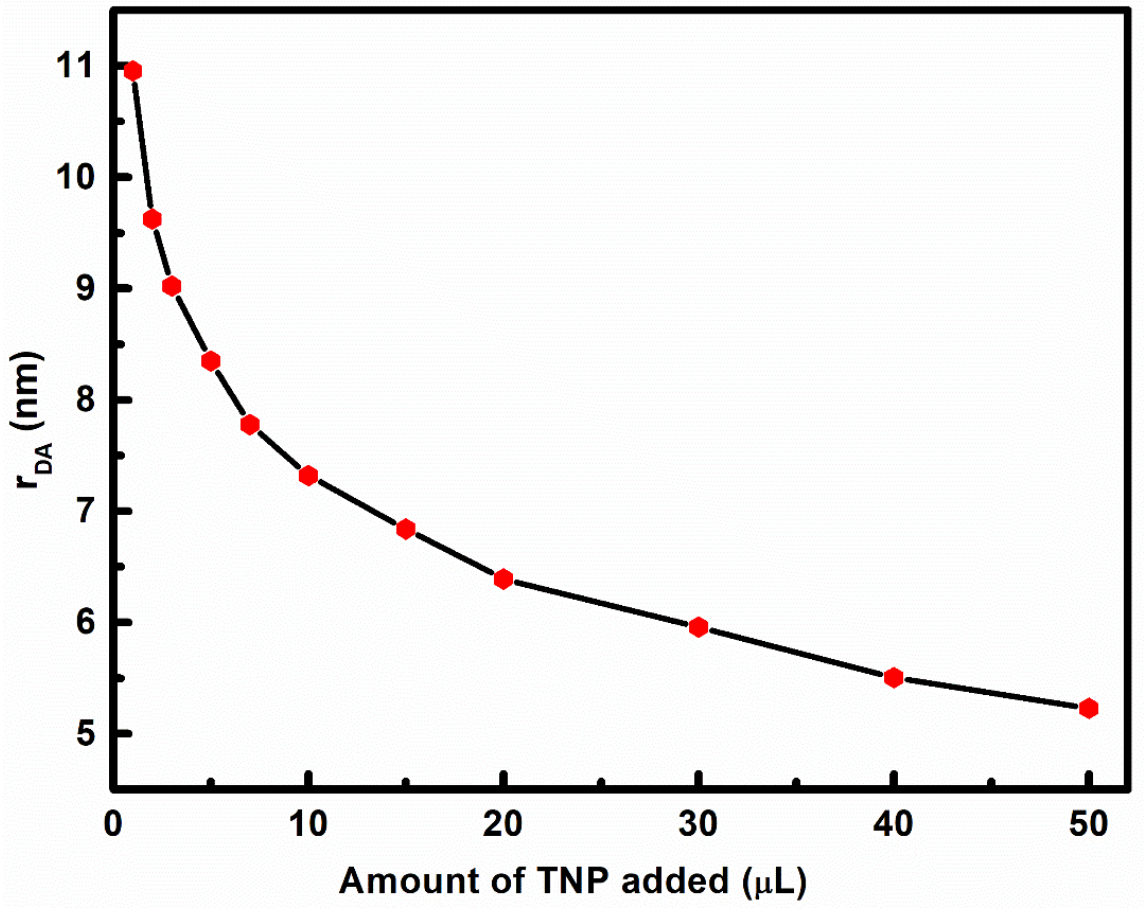

Figure 3.18. *The plot between donor-acceptor distance (r_{DA}) and the concentrations of TNP.*

However, unlike PL, the lifetime of MoS_2 QDs in the absence and the presence of TNP is nearly the same; hence, Förster resonance electron transfer (FRET) is excluded. The observed almost constant lifetime and the linear relation between the rate of energy transfer and TNP concentration demonstrated the radiative energy transfer as an efficient mechanism between the QDs and TNP. Fig. 3.19 shows the possible PL quenching mechanism of MoS_2 QDs by TNP while using QDs as a sensing probe and TNP as a quencher.

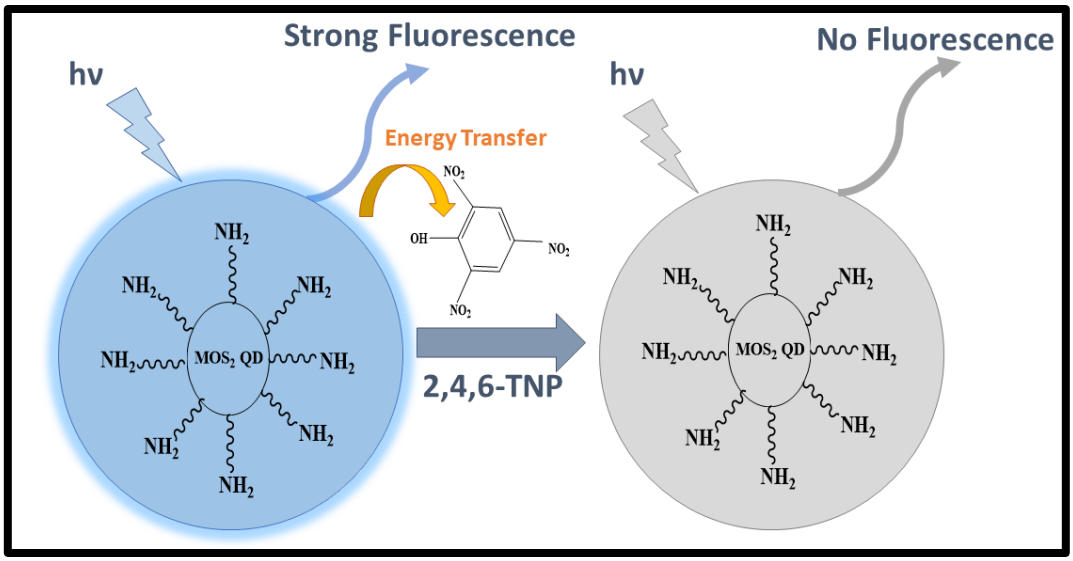

Figure 3.19. *Schematic diagram of the process of fluorescence quenching of MoS_2 QD by TNP.*

3.5 Conclusions

The functionalized colloidal MoS_2 QDs were prepared by considering a facile hydrothermal route to get high-quality of QDs. The HR-TEM of QDs exhibits a spherical shape with size in the range of 2-4 nm. The quantum yield of the fluorescent MoS_2 QDs comes out to be 8%. The FTIR spectrum of the QDs further supports the formation of Mo-S and N-H vibrational stretching. The absorption spectrum of MoS_2 QDs showed a peak at 287 nm. The band-gap energy estimated by Tauc's relation is 4.5 eV. The PL peak was observed at 420 nm when excited with wavelength of 340 nm. The PL of QDs doped in PVA film were also studied at low temperatures. The exponential increase in the PL intensity was observed by lowering the temperature from 300 to 100 K.

The functionalized QDs then employed as an efficient and highly selective probe for detecting TNP without the interference of other nitro explosives. The PL intensity of the MoS_2 QDs was quenched to ~98%. The linear S-V plot and rate of energy transfer as a function of

concentration along with the constant lifetime confirmed the feasibility of radiative energy transfer instead of nonradiative energy transfer as a possible mechanism for PL quenching.

References

[1] Z. Hu, B.J. Deibert, J. Li, Luminescent metal-organic frameworks for chemical sensing and explosive detection, Chem. Soc. Rev. 43 (2014) 5815–5840.

[2] M.E. Germain, M.J. Knapp, Optical explosives detection: from color changes to fluorescence turn-on, Chem. Soc. Rev. 38 (2009) 2543–2555.

[3] K. Das, U. Panda, A. Datta, S. Roy, S. Mondal, C. Massera, T. Askun, P. Celikboyun, E. Garribba, C. Sinha, K. Anand, T. Akitsu, K. Kobayashi, An enolato-bridged dinuclear Cu (ii) complex with a coumarin-assisted precursor: a spectral, magnetic and biological study, New J. Chem. 39 (2015) 7309–7321.

[4] R. Feyisa Bogale, J. Ye, Y. Sun, T. Sun, S. Zhang, A. Rauf, C. Hang, P. Tian, G. Ning, Highly selective and sensitive detection of metal ions and nitroaromatic compounds by an anionic europium (iii) coordination polymer, Dalt. Trans. 45 (2016) 11137–11144.

[5] G. He, H. Peng, T. Liu, M. Yang, Y. Zhang, Y. Fang, A novel picric acid film sensor via combination of the surface enrichment effect of chitosan films and the aggregation-induced emission effect of siloles, J. Mater. Chem. 19 (2009) 7347.

[6] J.F. Xiong, J.X. Li, G.Z. Mo, J.P. Huo, J.Y. Liu, X.Y. Chen, Z.Y. Wang, Benzimidazole Derivatives: Selective Fluorescent Chemosensors for the Picogram Detection of Picric Acid, J. Org. Chem. 79 (2014) 11619–11630.

[7] D. Haldar, D. Dinda, S.K. Saha, High selectivity in water soluble MoS_2 quantum dots for sensing nitro explosives, J. Mater. Chem. C. 4 (2016) 6321–6326.

[8] E.R. Goldman, I.L. Medintz, J.L. Whitley, A. Hayhurst, A.R. Clapp, H.T. Uyeda, J.R. Deschamps, M.E. Lassman, H. Mattoussi, A hybrid quantum dot−antibody fragment fluorescence resonance energy transfer-based TNT sensor, J. Am. Chem. Soc. 127 (2005) 6744–6751.

[9] P. Sharma, M.S. Mehata, Colloidal MoS_2 quantum dots based optical sensor for detection of 2,4,6-TNP explosive in an aqueous medium, Opt. Mater. (Amst). 100 (2020) 109646.

[10] K. Zhang, H. Zhou, Q. Mei, S. Wang, G. Guan, R. Liu, J. Zhang, Z. Zhang, Instant visual detection of trinitrotoluene particulates on various surfaces by ratiometric fluorescence of dual-emission quantum dots hybrid, J. Am. Chem. Soc. 133 (2011) 8424–8427.

[11] P. Wu, C. Xu, X. Hou, J.-J. Xu, H.-Y. Chen, Dual-emitting quantum dot nanohybrid for imaging of latent fingerprints: simultaneous identification of individuals and traffic light-type visualization of TNT, Chem. Sci. 6 (2015) 4445–4450.

[12] D. Gao, Z. Wang, B. Liu, L. Ni, M. Wu, Z. Zhang, Resonance energy transfer-amplifying fluorescence quenching at the surface of silica nanoparticles toward ultrasensitive detection of TNT, Anal. Chem. 80 (2008) 8545–8553.

[13] R. Cheng, S. Jiang, Y. Chen, Y. Liu, N. Weiss, H.-C. Cheng, H. Wu, Y. Huang, X. Duan, Few-layer molybdenum disulfide transistors and circuits for high-speed flexible

electronics, Nat. Commun. 5 (2014) 5143.
[14] Q.H. Wang, K. Kalantar-Zadeh, A. Kis, J.N. Coleman, M.S. Strano, Electronics and optoelectronics of two-dimensional transition metal dichalcogenides, Nat. Nanotechnol. 7 (2012) 699–712.
[15] H.I. Karunadasa, E. Montalvo, Y. Sun, M. Majda, J.R. Long, C.J. Chang, A molecular MoS_2 edge site mimic for catalytic hydrogen generation, Science. 335 (2012) 698–702.
[16] K.F. Mak, C. Lee, J. Hone, J. Shan, T.F. Heinz, Atomically thin MoS_2 : A new direct-gap semiconductor, Phys. Rev. Lett. 105 (2010) 136805.
[17] D. Gopalakrishnan, D. Damien, M.M. Shaijumon, MoS_2 quantum dot-interspersed exfoliated MoS_2 nanosheets, ACS Nano. 8 (2014) 5297–5303.
[18] H. Dong, S. Tang, Y. Hao, H. Yu, W. Dai, G. Zhao, Y. Cao, H. Lu, X. Zhang, H. Ju, Fluorescent MoS_2 quantum dots: ultrasonic preparation, up-conversion and down-conversion bioimaging, and photodynamic therapy, ACS Appl. Mater. Interfaces. 8 (2016) 3107–3114.
[19] S. Xu, D. Li, P. Wu, One-pot, facile, and versatile synthesis of monolayer MoS_2 /WS_2 quantum dots as bioimaging probes and efficient electrocatalysts for hydrogen evolution reaction, Adv. Funct. Mater. 25 (2015) 1127–1136.
[20] M. Singh Mehata, Y. Yang, K. Han, Probing charge-transfer and short-lived triplet states of a biosensitive molecule, 2,6-ANS: transient absorption and time-resolved spectroscopy, ACS Omega. 2 (2017) 6782–6785.
[21] W. Xiao, W. Zhou, T. Feng, Y. Zhang, H. Liu, L. Tian, Simple synthesis of molybdenum disulfide/reduced graphene oxide composite hollow microspheres as supercapacitor electrode material., Mater. (Basel, Switzerland). 9 (2016) 783.
[22] R.K. Ratnesh, M.S. Mehata, Controlled synthesis and optical properties of tunable CdSe quantum dots and effect of pH, AIP Advances 5 (2015) 097114.
[23] R.K. Ratnesh, M.S. Mehata, Investigation of biocompatible and protein sensitive highly luminescent quantum dots/nanocrystals of CdSe, CdSe/ZnS and CdSe/CdS, Spectrochim. Acta - Part A Mol. Biomol. Spectrosc. 179 (2017) 201–210.
[24] H. Swaminathan, K. Balasubramanian, Sensors and Actuators B : Chemical Förster resonance energy transfer between MoS_2 quantum dots and polyaniline for turn-on bovine serum albumin sensing, Sensors and Actuators B. Chem. 264 (2018) 337–343.

CHAPTER 4

MoS_2 Quantum Dots for the Lead Metal Ions Sensing*

4.1 Introduction

Over the years, a series of fluorescent chemo-sensors have been recognized for the remarkable detection of ions and other neutral analytes, widely implied in distinct sectors such as pharmacology, physiology, biology, and environmental sciences. Despite the development made over the period, several more challenges could be achieved in the coming years through fluorescent sensors. Such challenges include the detection of the biologically and environmentally important species, such as detection of the toxic heavy metal ions (which are biologically not essential and are harmful) [1–4], the reactive oxygen (ROS) and nitrogen (RNS) species (which are essential for cell's internal redox status, but redox changes could lead to acute diseases like cancer, diabetes, etc.) [5–7], chemical explosive compounds [8], etc. In the past few years, the semiconductor quantum dots (QDs) have been preferred for sensing applications because of their unique photophysical properties. The bright luminous QDs act as a fluorescent probe for the rapid detection of various ions and neutral analytes [9].

The two-dimensional (2D) compounds and their quantum dots have recently gained great attention for sensing purposes. One such compound is the molybdenum disulfide (MoS_2) nanoparticles which have been the notion of research because of its magnificent electrical, optical and physical properties, which makes it appropriate for various applications such as sensing, energy storage, electro catalysis, photo catalysis and optoelectronic devices [10-19].

*Part of this work has been published in **Materials Research Bulletin 131 (2020) 1109782.**

MoS_2 is a popularly recognized layered transition metal dichalcogenide, also acknowledged as the inorganic cousin of graphene. The preparation of their quantum dots turns out to be very significant because of their distinct optical and electronic properties compared to their bulk counterparts due to the enactment of quantum confinement and edge effects [21–23]. The MoS_2 QDs exhibit excellent blue emission when exposed to ultraviolet (UV) illumination, which attributes to the transition from the K point of the Brillouin zone [24].

The exceptional properties of MoS_2 QDs lead to various applications in bioimaging, catalysis, sensing and photodynamic therapy [25–32]. The luminescent behaviour of MoS_2 QDs acts as a fluorescent probe for various sensing applications, such as detection of pesticide (i.e., methyl parathion), explosive compounds (i.e., 2,4,6-trinitrophenol), biomolecules (i.e., bovine serum albumin, hyaluronidase and dopamine) and other chemical compounds (such as hydrogen peroxide, glucose, hypochlorite) [29,33–36]. So far, very few articles have been reported that recognize the MoS_2 QDs as a metal ion sensor for detecting ions like Al^{3+}, Cu^{2+} and Fe^{3+} [4,37–40]. However, the study of metal ion sensing through MoS_2 QDs is limited [41].

Both top-down and bottom-up approaches could develop the MoS2 QDs. The top-down approach includes harmful reagents, organic solvent, and very time taking processes [21]. While in the bottom-up method, the reaction conditions can be controlled more appropriately and produce high-quality QDs. Here, MoS_2 QDs were developed by modifying the previously reported hydrothermal method of synthesis [8]. The large-scale production of MoS_2 QDs is proposed by mixing sodium molybdate and thioacetamide as Mo and sulfur sources, respectively, in a fixed proportion and followed by the hydrothermal process. The as-

synthesized MoS_2 QDs exhibit blue emission at 440 nm when excited at 360 nm wavelength and possess a high quantum yield (QY) of ~17% in an aqueous medium.

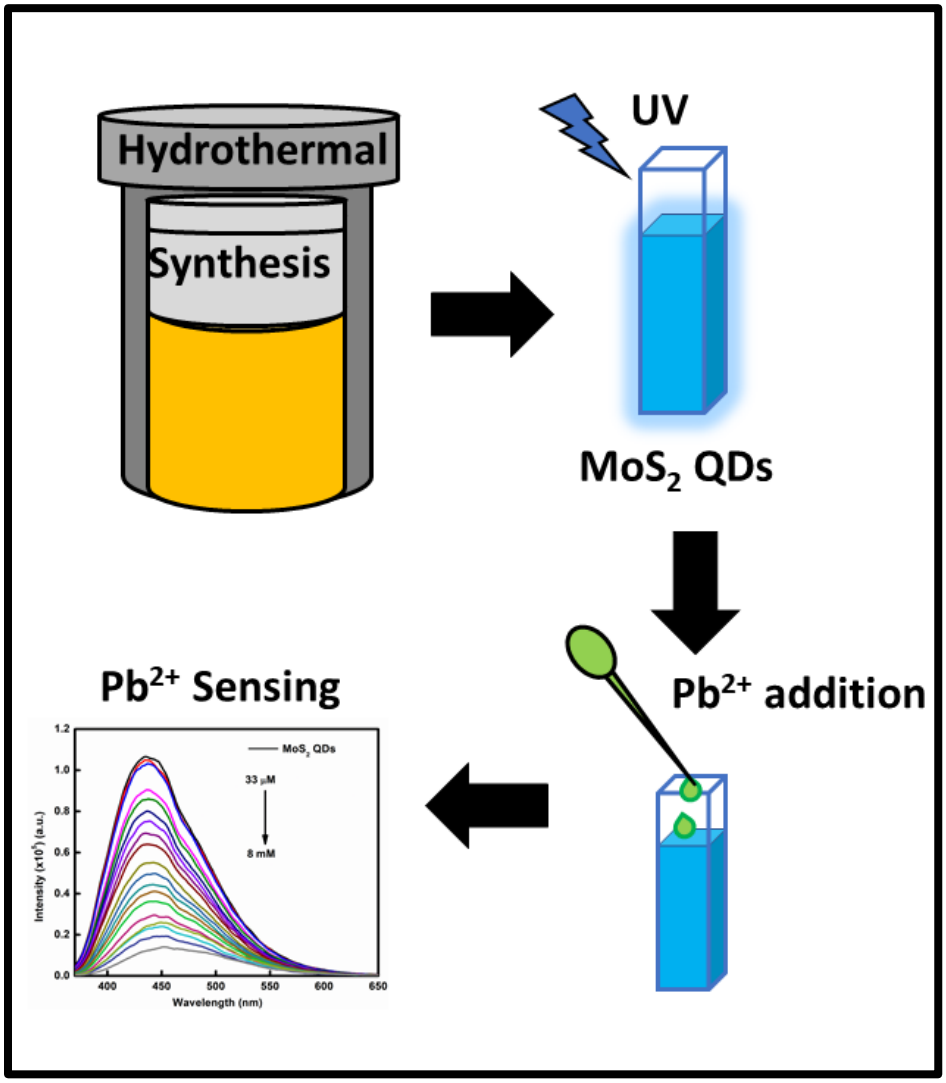

Figure 4.1. *Schematic representation of the steps involved in the PL quenching of MoS_2 QDs occurred in the presence of Pb^{2+} metal ions in water.*

The QDs were used as a fluorescent probe for the primary detection of the toxic metal ions in the aqueous medium, as shown in Fig. 4.1 (for Pb^{2+}). The processed colloidal sensing probe shows promising sensitivity towards the detection of Pb^{2+} ions. Lead is a commonly used substance for commercial purposes like agricultural sectors, pharmaceuticals, and

industries such as batteries, pigments, metallurgy, etc. Also, Pb^{2+} has been declared one of the most toxic elements by the world health organization (WHO) for the environment and human health and wildlife [42–44]. The small amount of Pb^{2+} metal ions can cause severe brain dysfunctionalities and nervous breakdown [45,46]. So, due to its high toxicity, it becomes an urgent requirement to detect Pb^{2+} metal ions by using advanced materials with high sensitivity and selectivity.

4.2 Materials and Method

4.2.1 Chemicals and reagents

All precursors and reagents used were of analytical grade and received from Sigma Aldrich. The sodium molybdate, thioacetamide and 1,4-diaminobutane were used as precursors for the synthesis of MoS_2 QDs. The metal analytes used in the experiment such as lead (II) perchlorate, cadmium chloride hydrate, mercury chloride, aluminum perchlorate nonahydrate, zinc perchlorate hexahydrate, cobalt (II) perchlorate hexahydrate, copper (II) chloride anhydrous, nickel (II) perchlorate, iron (II) perchlorate tetrahydrate and iron (III) perchlorate hydrate were obtained from Sigma Aldrich. For the dialysis, a 1KDa Pur-a-lyzer dialysis kit was acquired from Sigma Aldrich.

4.2.2 Synthesis of MoS_2 QDs

MoS_2 QDs were synthesized by a facile hydrothermal process involving the sodium molybdate as Mo source, thioacetamide (TAA) as a sulfur source and 1,4-diaminobutane (DAB) as capping agent. MoS_2 QDs were synthesized through the interaction of both the precursors in a high-temperature hydrothermal reactor and considered as an eco-friendly and easy approach. Here, 0.2 g of sodium molybdate and 0.3 g of TAA was dissolved in 70 ml deionized (DI) water for 0.5 h. Then, a certain amount of DAB was added to the above mixture. Afterward,

the resultant mixture was kept in a bum shell for the hydrothermal process in an oven at 200 ^{o}C for 24 h, and eventually allowed to cool down naturally. Finally, the obtained supernatant was dialyzed through the 1kDa dialysis membrane for 48 h. At every 2 h interval, the water of the dialysis membrane was changed. The as-purified amine-functionalized MoS_2 QDs were stored at 4^{o} C for further characterization and uses. The schematic synthesis of functionalized MoS_2 QDs by the facile hydrothermal process is demonstrated in Fig. 4.2.

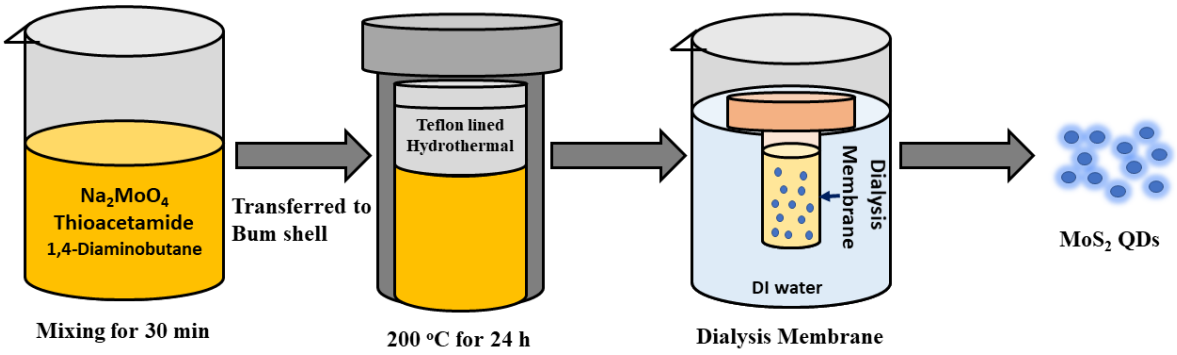

Figure 4.2. *Schematic representation of the synthesis of functionalized MoS_2 QDs by facile hydrothermal process.*

4.3 Instrumentation

The morphological studies of the prepared MoS_2 QDs were analyzed using high-resolution transmission electron microscopy (HR-TEM, TALOS, Thermo scientific instruments) at an accelerating voltage of 200 kV. The Fourier transform infrared spectroscopy (FT-IR) spectrum was recorded on the spectrum (II) (Perkin Elmer) ranging from 450 to 4000 cm^{-1}. The UV/VIS/IR double beam spectrophotometer (Lambda 750, Perkin Elmer) was used to observe the steady-state absorption spectra. The spectrofluorometer (Flourolog-3, Horiba Jobin Yvon Inc.) equipped with a 450 W xenon lamp was used to record the photoluminescence (PL) spectra [47]. Quartz cuvette was used for recording absorption and PL spectra, whereas the frontal geometry stage was used to eliminate the inner filter effect. Fluorescence decay curves

were recorded with the time-correlated single-photon counting (TCSPC) arrangement (DeltaFlex-01-DD, Horiba Jobin Yvon IBH Ltd.) equipped with PMT (PPD 850) and Delta Diode of wavelength 360 nm. To analyse the observed PL decays, the least square fitting and re-convolution methods were used. The total number of counts was kept at 10,000 in the peak channel. The instrument response function was taken by Ludox scatterer.

4.4 Results and Discussion

4.4.1 High-resolution transmission electron microscope (HR-TEM) images

Fig. (4.3) illustrates the HRTEM images of the prepared MoS_2 QDs. The images show that the particles were heterogeneously distributed with dimensions ranging from 2 to 5 nm (Fig. 4.3a). The ordered lattice fringes confirm the crystalline structure of MoS_2 QDs and the lattice d-spacing corresponds to the (103) plane is 2.25 Å (Fig. 4.3b).

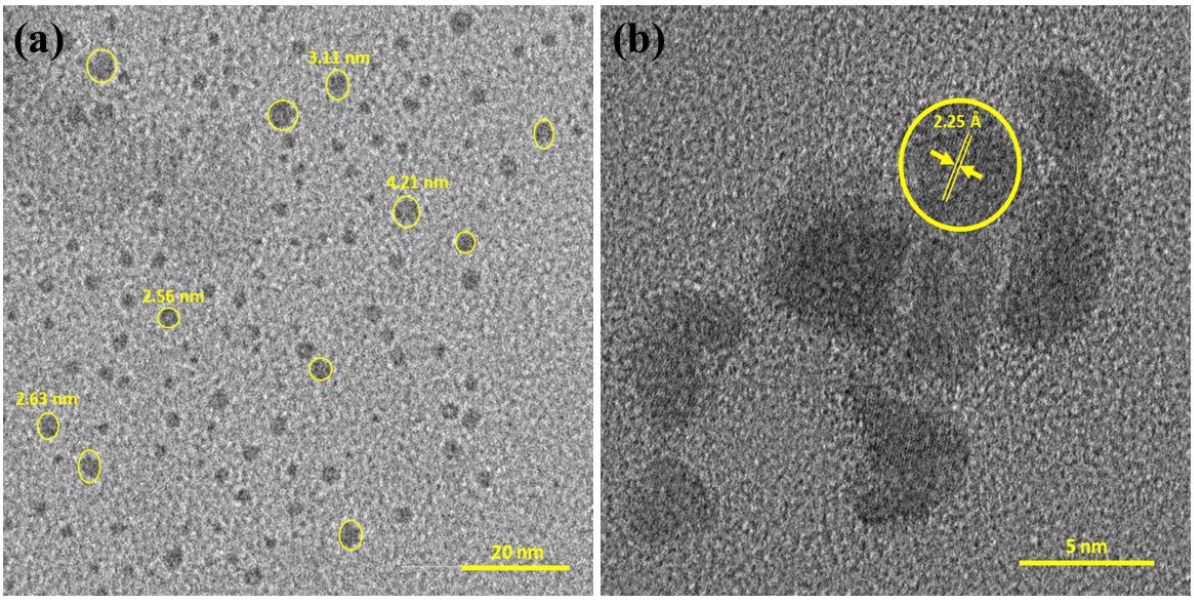

Figure 4.3. *HR-TEM images of MoS_2 QDs dispersed in water at different magnifications.*

4.4.2 Fourier transform infrared (FTIR) spectrum

Fig. (4.4) illustrates the FT-IR spectrum of functionalized MoS_2 QDs. The vibrational peaks at 3333 cm^{-1} and 1630 cm^{-1} represent the N-H stretching and bending modes, respectively, with a weak band at 481 cm^{-1} corresponding to Mo-S stretching vibrations [8].

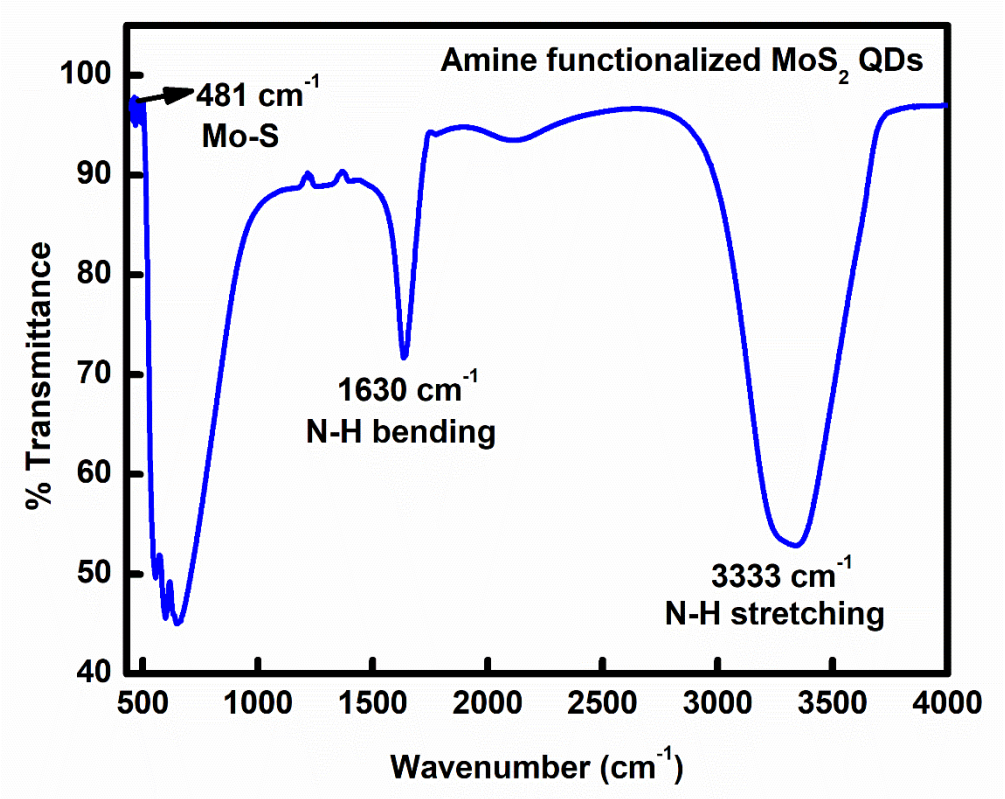

Figure 4.4. *FTIR spectrum of pristine MoS_2 QDs dispersed in water.*

4.4.3 UV-visible absorption spectroscopy

The absorption spectrum of as-synthesized MoS_2 QDs dispersed in water is shown in Fig. 4.5. The absorption peak at around 300 nm corresponds to the excitonic behaviour of MoS_2 QDs, which is slightly redshifted from the earlier report [38] and is probably due to the larger size of QDs. The optical energy bandgap (E_g) of as-synthesized MoS_2 QDs has been calculated from the Tauc′s equation:

$$\boldsymbol{\alpha h\nu = A(h\nu - E_g)^n} \qquad \textbf{(4.1)}$$

where A is a constant identified as the band tailing parameter, α signifies the absorption coefficient, ***n*** represents the power factor of the transition mode and ***hν*** is the photon energy. The factor '***n***' depends on the type of electronic transition and is considered ½ for the direct transitions. The energy bandgap of QDs was calculated by extrapolating the linear part of the Tauc′s plot obtained between $(\alpha h\nu)^2$ and the photon energy $(h\nu)$, and the interception of the $h\nu$ axis by the straight line gives the energy bandgap of MoS_2 QDs, as shown in the inset of Fig. 4.5.

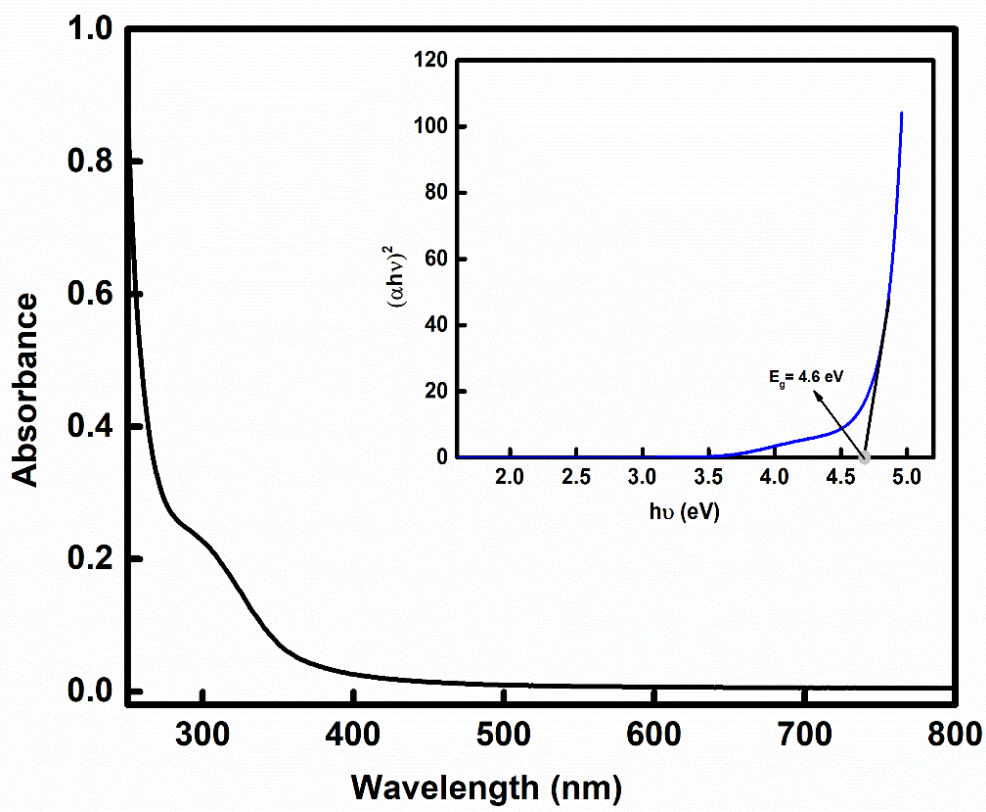

Figure 4.5. *The absorption spectrum of MoS_2 QDs dispersed in water. Inset shows the Tauc's plot for the direct optical bandgap.*

The direct optical bandgap of the developed QDs comes out to be ~4.6 eV, which is very large as compared to its bulk counterpart (1.2 eV) and is due to the quantum confinement effect.

4.4.4 Photoluminescence (PL) spectroscopy

The PL spectrum of the as-synthesized MoS_2 QDs exhibits a maximum intensity at 440 nm when excited with 360 nm wavelength, whereas the corresponding excitation spectrum peaked at 360 nm (Fig. 4.6).

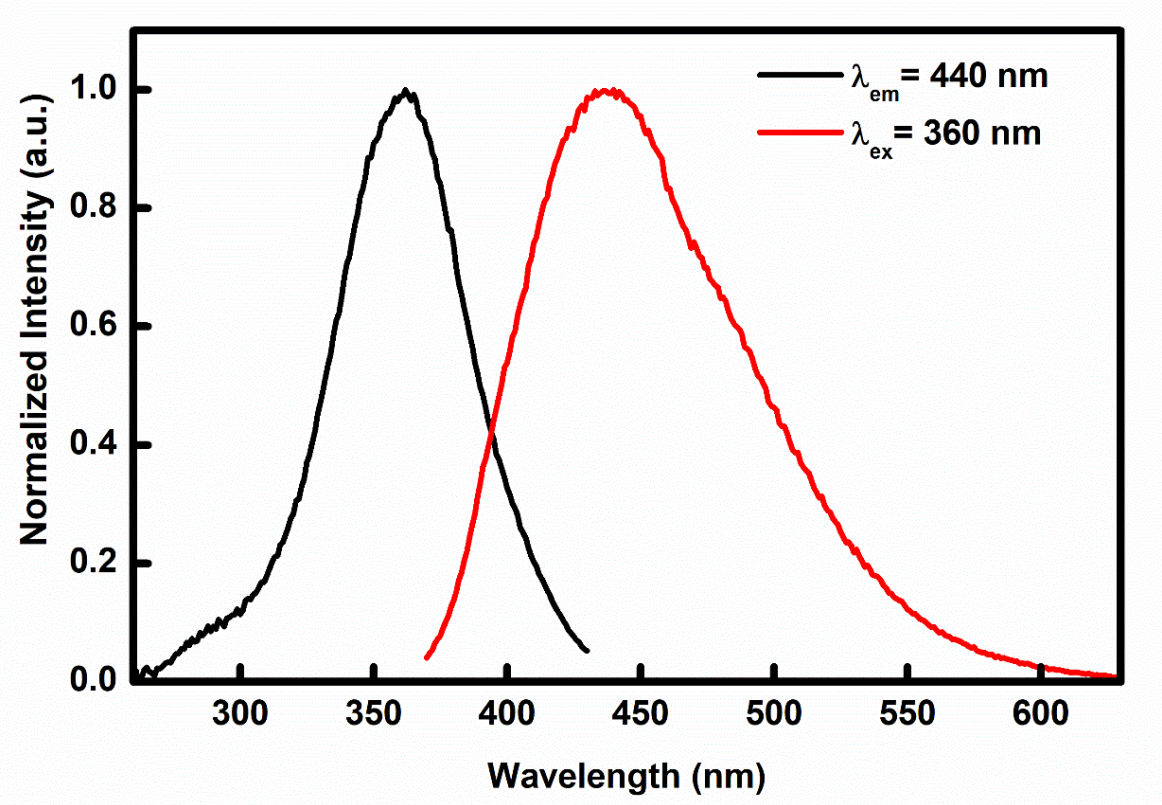

Figure 4.6. *The peak normalized PL (red) and PL-excitation (black) spectra of MoS_2 QDs in water.*

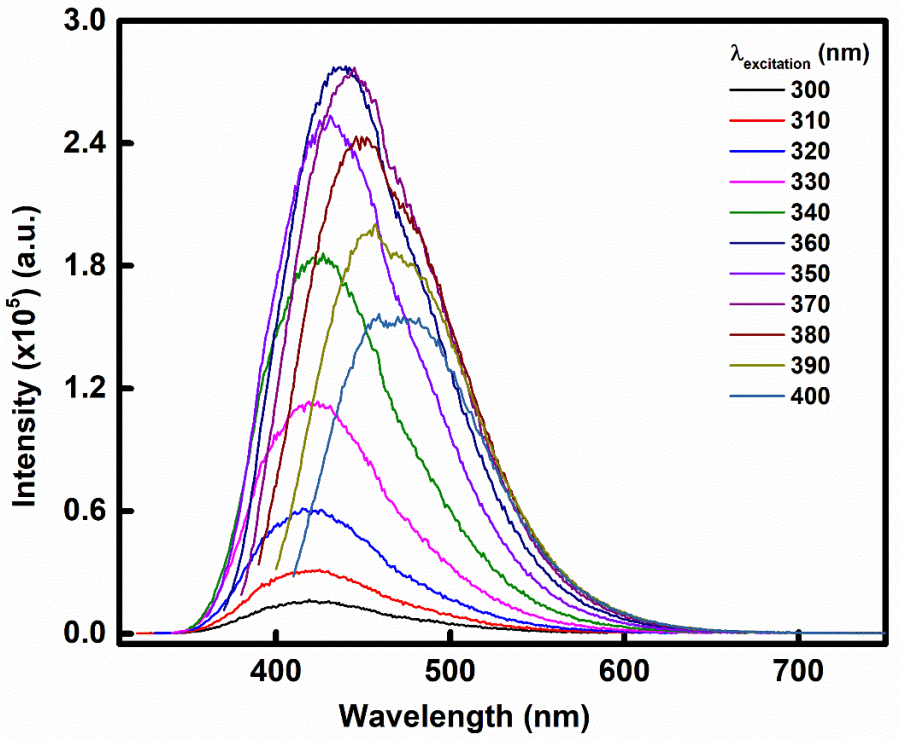

Figure 4.7. *The PL spectra of MoS_2 QDs in the water at different excitation wavelengths.*

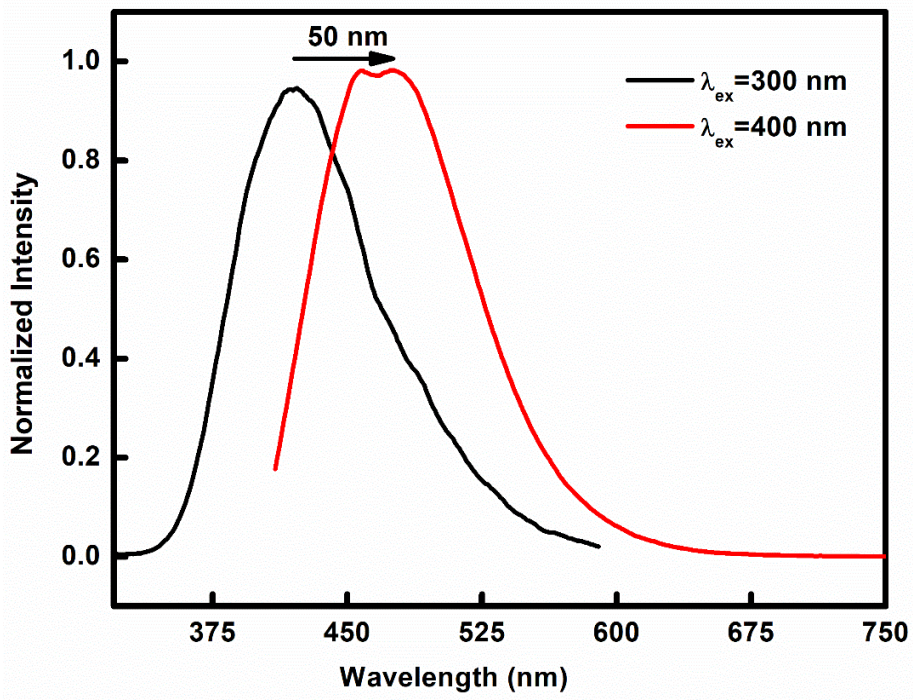

Figure 4.8. *Peak normalized PL spectra of MoS_2 QDs dispersed in water at excitation wavelengths of 300 and 400 nm.*

The PL intensity increases without changing peak wavelength after changing the excitation wavelength from 300 to 350 nm. With further increasing the excitation wavelength from 350 to 400 nm, the PL maximum shifts towards the longer wavelength region *i.e.*, from 410 to 470 nm, as shown in Fig. 4.7. The normalized PL intensity demonstrates the shift in PL maximum, as shown in Fig. 4.8. Similarly, the PL excitation spectrum shifted from 347 to 367 nm by increasing the monitored PL wavelength from 400 to 470 nm (Figs. 4.9 and 4.10). The wavelength-dependent behaviour of MoS_2 QDs may be considered due to the polydispersity of colloidal synthesis or inhomogeneous distribution of particles and surface functionalization [48,49].

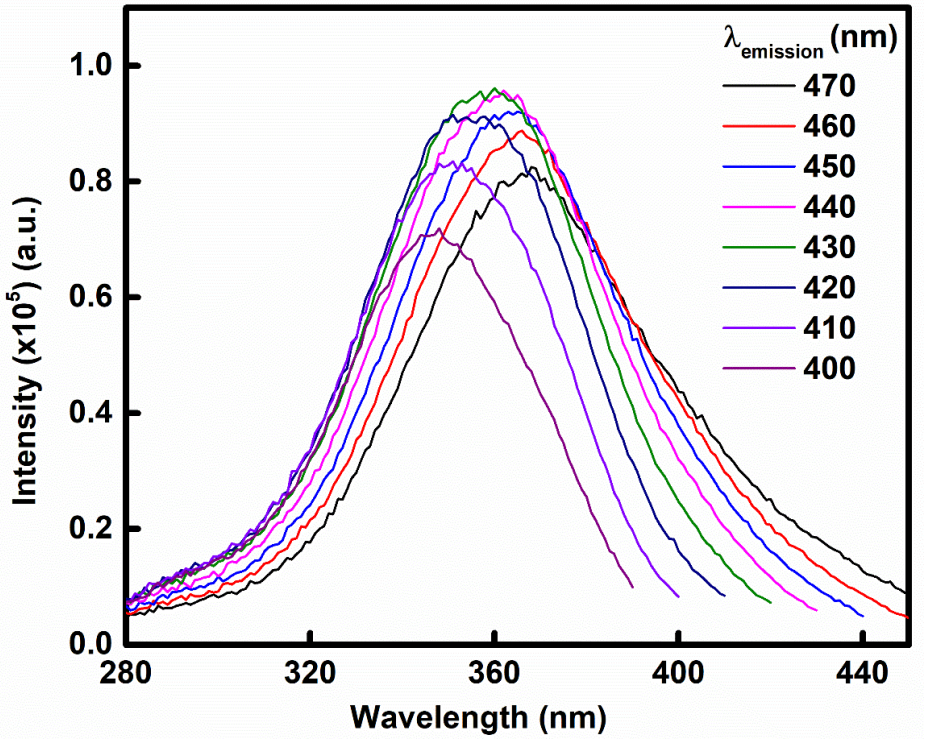

Figure 4.9. *PL-excitation spectra of MoS_2 QDs dispersed in water at different PL wavelengths.*

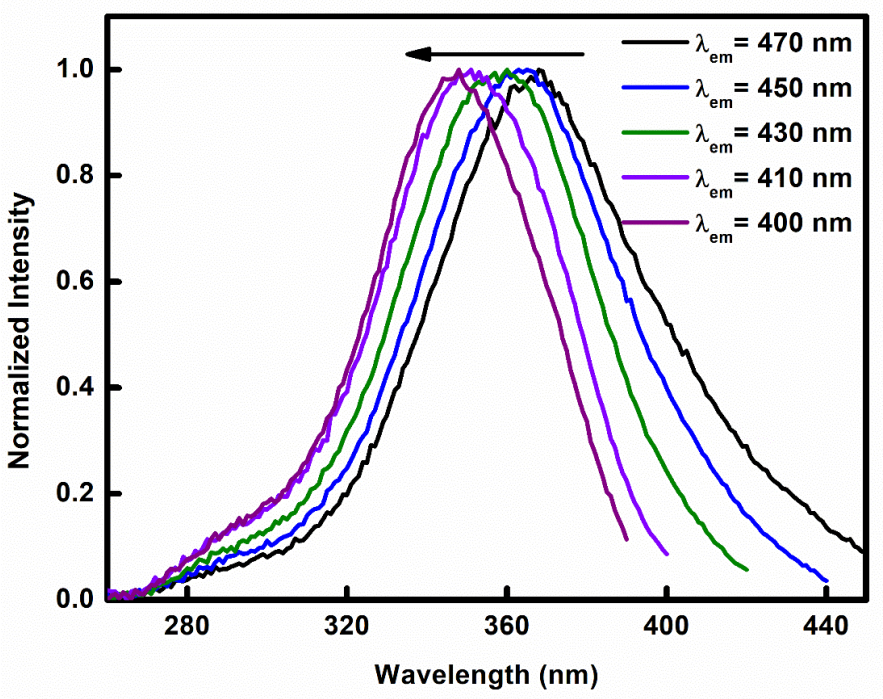

Figure 4.10. *Peak normalized PL-excitation spectra of MoS_2 QDs dispersed in water at different PL wavelengths.*

The PL quantum yield (QY) of the MoS_2 QDs was calculated using Eq (4.2), considering quinine sulphate as a reference with a quantum yield of 54.2% [5,50].

$$\boldsymbol{QY_{sample} = QY_{reference} \times \frac{Area_{sample}}{Area_{reference}} \times \frac{Abs_{reference}}{Abs_{sample}} \times \left(\frac{\eta_{sample}}{\eta_{reference}}\right)^2} \qquad \textbf{(4.2)}$$

where the QY_{sample} and $QY_{reference}$ signify the quantum yield of sample and reference respectively, $Area_{sample}$ and $Area_{reference}$ represent the area under the curve of PL for sample and reference, respectively (at the excitation wavelength of 300 nm), whereas *Abs* represents the absorbance and $\boldsymbol{\eta}$ is the refractive index of the medium. The estimated QY of MoS_2 QDs is ~17%, which is higher than that of the reported fluorescent MoS_2 QDs and graphene QDs [8,51–54].

4.4.5 Absorption spectra of MoS_2 QDs with metal ions (Sensing)

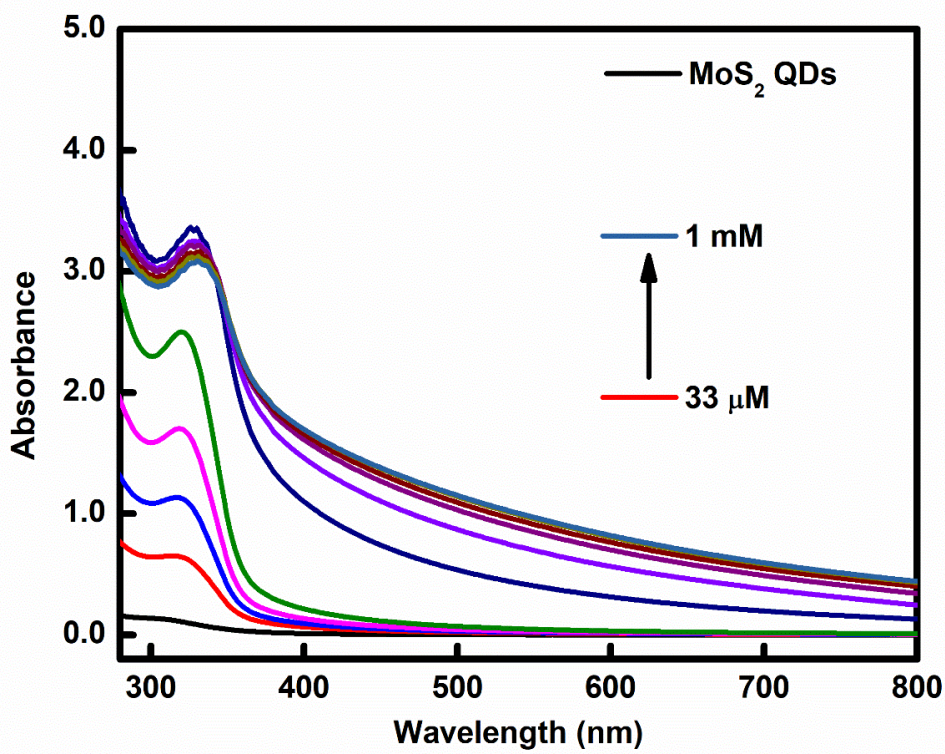

Figure 4.11. *The absorption spectra of MoS_2 QDs in the presence of various concentrations of Pb^{2+} ions in water.*

Fig. 4.11 illustrates the absorption spectra of the synthesized MoS_2 QDs in the presence of different concentrations of Pb^{2+} ions. In the presence of a low concentration of Pb^{2+} ions (33 μM), the optical density (absorbance) is increased, accompanied by the sharpening of the absorption band. Upon increasing the concentration of Pb^{2+} ions from 0.0 to 0.2 mM, the optical density increases from 0.10 to 3.30. The increase in absorbance and change in the spectral shape indicates the formation of MoS_2 QDs/Pb^{2+} complex. A linear relationship has been observed between the absorbance of MoS_2 QDs with the concentration of Pb^{2+} metal ions (Fig. 4.12). The observed linear relation demonstrates that MoS_2 QDs could be used as a probe for sensing Pb^{2+} metal ions in the aqueous environment.

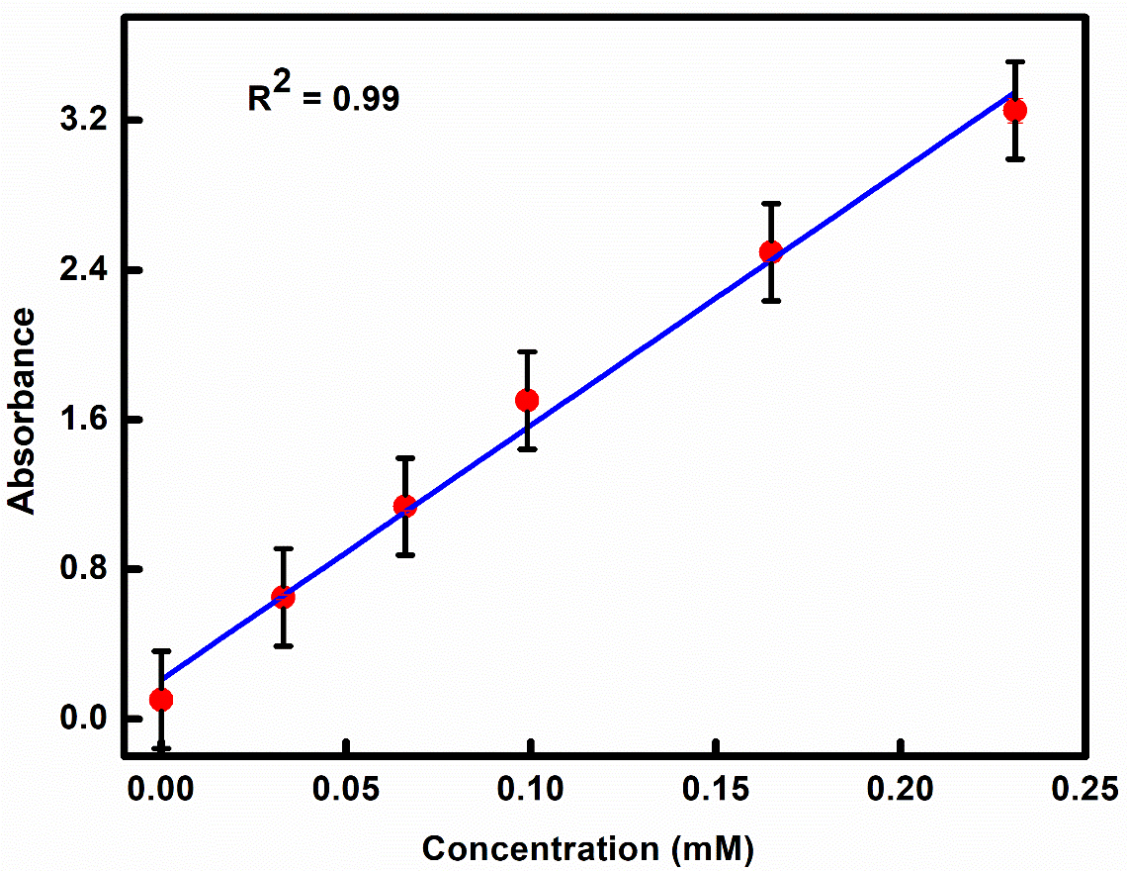

Figure 4.12. *A plot between the absolute absorption intensity of MoS_2 QDs vs. the concentration of Pb^{2+} ions.*

4.4.6 PL quenching of MoS_2 QDs with metal ions

The PL titration of MoS_2 QDs, used as a fluorescent probe (sensor), was conducted for different concentrations of metal ions in an aqueous environment, and the results are shown in Fig. 4.13.

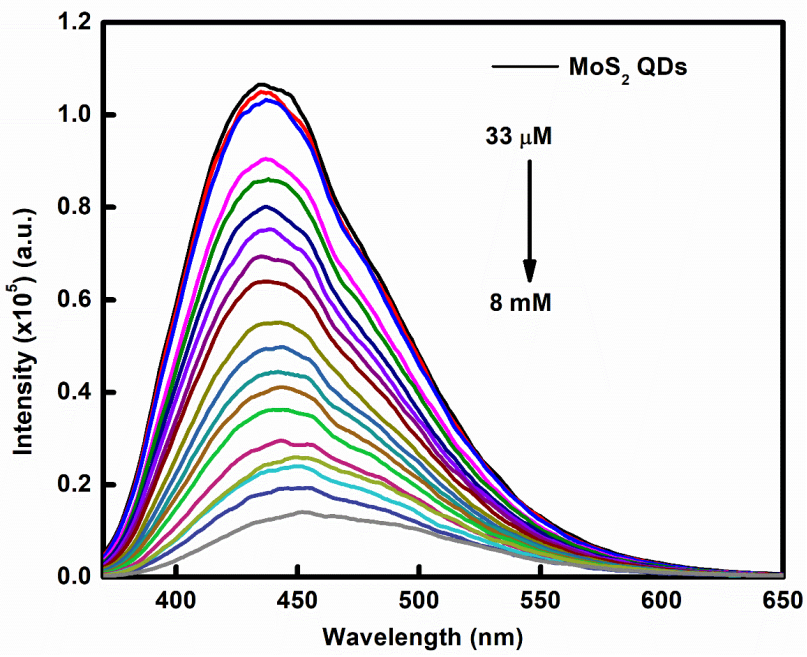

Figure 4.13. *The PL spectra of MoS_2 QDs at different concentrations of Pb^{2+} ions in water at the excitation wavelength of 360 nm.*

The metal ion sensing experiments were done by taking 3 mL of the MoS_2 QDs dispersed in DI water in a quartz cuvette (10 ×10 mm) and then various concentrations of metal ion (from 33 µM to 8.0 mM) were added. The PL intensity obtained at 360 nm excitation quenched gradually with increasing the concentration of metal ions, as shown in Fig. 4.13. With a small amount (33 µM) of Pb^{2+} ions, a decrement in PL intensity is noticed. Almost half of the PL intensity has been quenched with the addition of 1.6 mM of Pb^{2+} ion. When the analyte concentration reaches around 8.0 mM, the PL intensity reduced approximately 89% of the initial value. The graphical representation of the turn-off PL of MoS_2 QDs by Pb^{2+} ions is shown in Fig. 4.14. Initially, the QDs solution shows the flaxen colour under sunlight and blue colour under UV light; however, in the presence of metal ions, the solution became colourless under UV light.

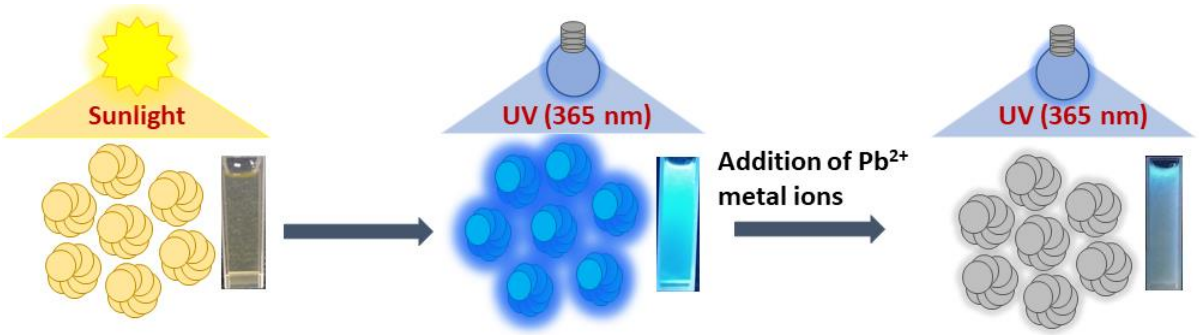

Figure 4.14. *The graphical representation of PL turn-off sensing of Pb^{2+} ions by MoS_2 QDs.*

The substantial reduction in PL intensity was analysed using a well-known Stern-Volmer (S-V) equation (4.3)

$$\mathbf{I_0/I = K_{S\text{-}V}\,[Pb^{2+}] + 1} \qquad \mathbf{(4.3)}$$

where I_0 and I signify the initial PL intensity and final PL intensity (in the presence of analytes), respectively, $[Pb^{2+}]$ signifies the molar concentration of the analyte added to the MoS_2 QDs and $K_{S\text{-}V}$ signifies the PL quenching constant (M^{-1}). The S-V plot for the PL quenching in the presence of Pb^{2+} metal ions illustrate a linear relationship for the complete range of concentrations (Fig. 4.15). The estimated quenching constant ($K_{S\text{-}V}$) came out to be 824 M^{-1}. Thus, the described Pb^{2+} metal ions sensor exhibits high sensitivity with a limit of detection (LOD) of 50 μM and covers a linear detection range from 3.3×10^{-7} to 8×10^{-3} M.

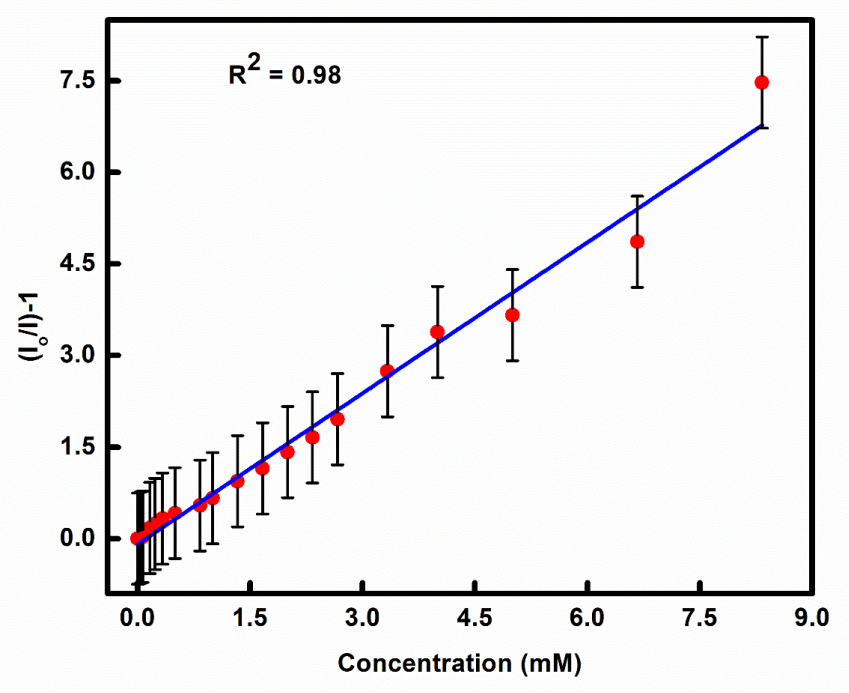

Figure 4.15. *The Stern-Volmer plot between relative PL intensity of MoS_2 QDs and Pb^{2+} ions concentration.*

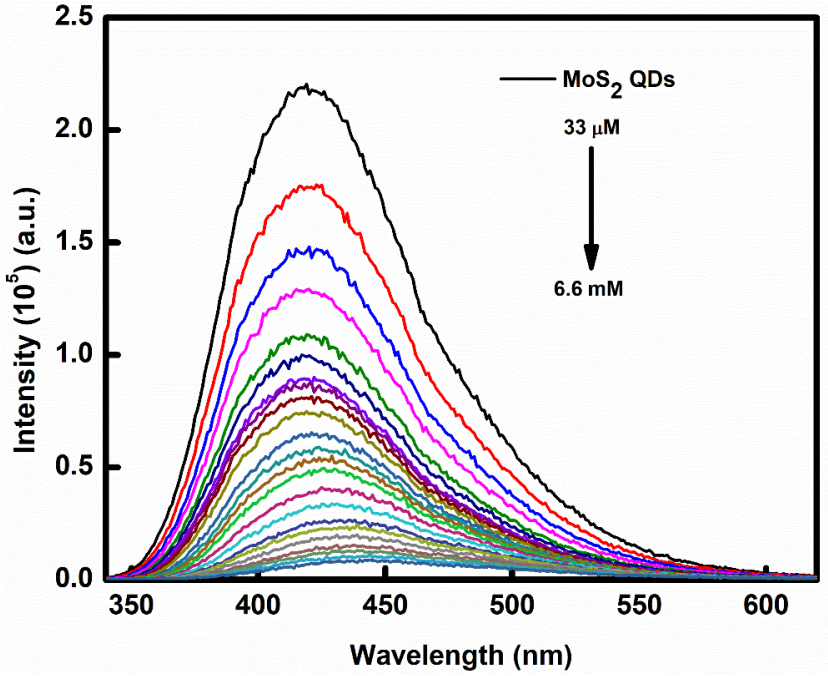

Figure 4.16. *PL spectra of MoS_2 QDs dispersed in water in the presence of various concentrations of lead ions. The excitation wavelength was 330 nm.*

Similar results were observed by changing the excitation wavelength, *i.e.*, with 330 nm excitation. The PL intensity is quenched significantly and covers a similar range of concentrations (Fig. 4.16). The corresponding S-V plot is linear (Fig. 4.17). The value of $K_{S\text{-}V}$ and LOD comes out to be 3.5×10^{3} M^{-1} and 12×10^{-5} M, respectively.

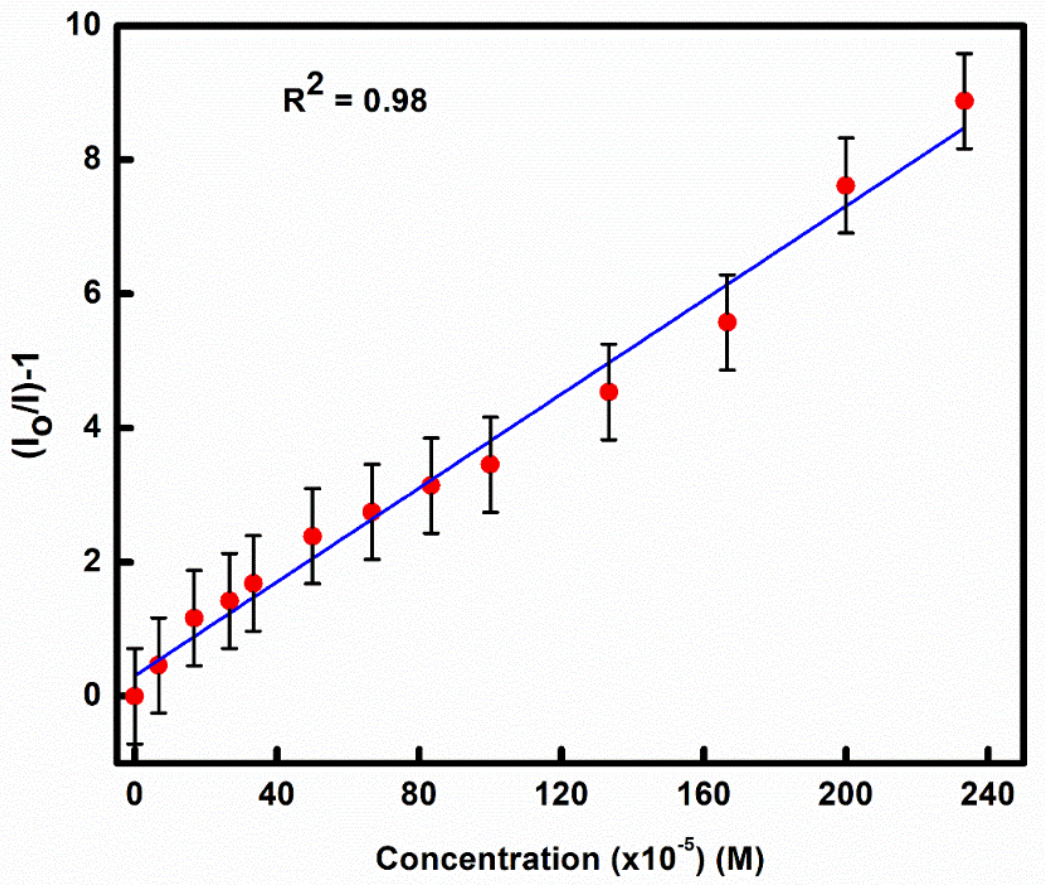

Figure 4.17. *A Stern-Volmer plot of MoS_2 QDs in the presence of various concentrations of Pb^{2+} ions.*

4.4.7 Time-resolved PL spectroscopy

The time-resolved PL decays of MoS_2 QDs at various analyte concentrations were recorded and demonstrated in Fig. 4.18. The decay curves could not be fitted well with mono- and bi-exponential models but follow a triexponential function:

$$\boldsymbol{I(t) = \alpha_1 e^{(-t/\tau_1)} + \alpha_2 e^{(-t/\tau_2)} + \alpha_3 e^{(-t/\tau_3)}} \qquad \textbf{(4.4)}$$

where α_i illustrates the pre-exponential factors and τ_i represents the lifetimes. The estimated lifetimes and corresponding pre-exponential values are summarized in Table 1. The lifetime component of 2.27 ns with the highest amplitude (72%), may represent the band edge PL. In contrast, the long lifetime component (16.18 ns), which has the smallest contribution (3%), may be assigned to the defect state of QDs. The average lifetime is calculated from equation (4.5).

$$\boldsymbol{\tau_{av}} = \sum(\boldsymbol{\alpha_i \tau_i}) \qquad \textbf{(4.5)}$$

The average lifetime decreased from 3.8 ns (0 mM) to 2.26 ns with the addition of a 1.65 mM Pb^{2+} ion. The slight increase of average PL lifetime at high concentration is due to the increase of longest lifetime component and corresponding amplitude, which may be arising from the increase of defect states contribution.

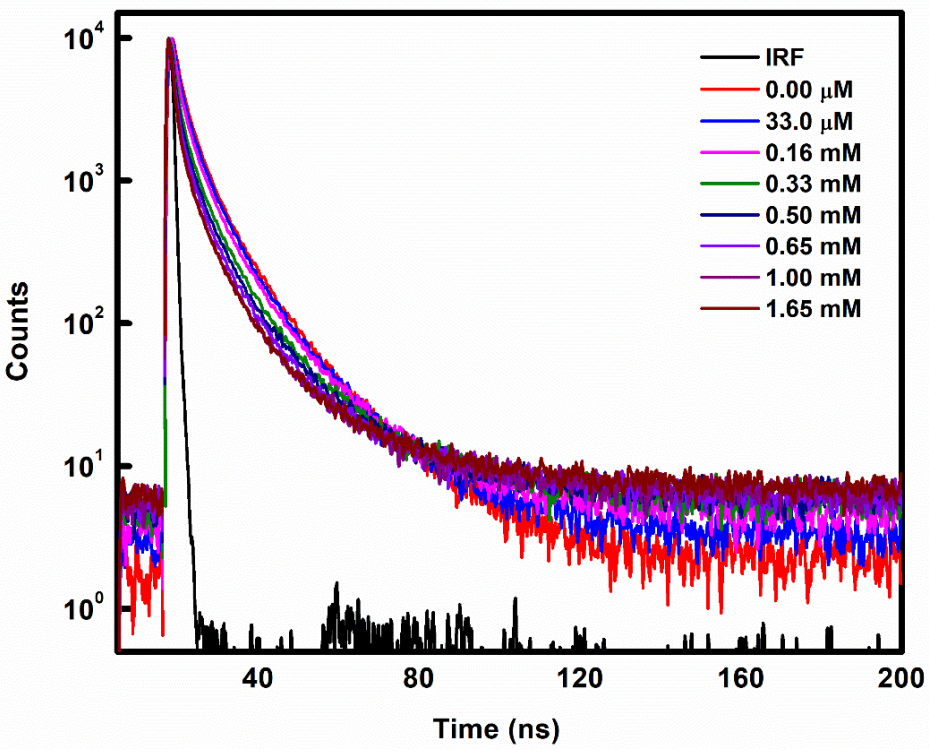

Figure 4.18. *The PL decay curves of MoS_2 QDs in the absence and the presence of different concentrations of Pb^{2+} ions with instrument response function (IRF).*

The decrease in the PL lifetime of MoS_2 QDs with the increase in the concentration of Pb^{2+} metal ions follows the S-V relation (Eq. 4.6).

$$\boldsymbol{I_0/I = \tau_o/\tau = K_{S\text{-}V}\,[Pb^{2+}] + 1} \qquad \textbf{(4.6)}$$

The $K_{S\text{-}V}$ value obtained from the slope of the linear S-V plot of Fig. 4.19 came out to be 0.60 M^{-1}. The quenching rate constant K_q calculated from the equation $K_{S\text{-}V} = K_q\tau_0$ is 1.58×10^8 $M^{-1}s^{-1}$, where τ_0 is the PL lifetime of MoS_2 QDs in the absence of metal ions.

Table 4.1. *Lifetimes (τ_i) and pre-exponential factors (α_i) of MoS_2 QDs with various concentrations of Pb^{2+} ions dispersed in water. The λ_{ex} and λ_{em} were 360 and 440 nm, respectively.*

Pb^{2+} conc. (mM)	$\tau_1(ns)$	$\tau_2(ns)$	$\tau_3(ns)$	α_1	α_2	α_3	$\tau_{av}(ns)$
0.00	6.67±0.02	2.28±0.02	16.18±0.31	0.25	0.72	0.03	3.80
0.16	7.01±0.02	2.17±0.01	18.47±0.69	0.21	0.77	0.02	3.51
0.30	7.31±0.11	1.93±0.01	22.63±3.16	0.18	0.81	0.01	3.10
0.50	7.10±0.12	1.84±0.02	21.05±2.10	0.16	0.83	0.01	2.90
0.65	6.09±0.10	1.55±0.01	16.39±1.51	0.17	0.81	0.02	2.62
1.00	6.57±0.10	1.50±0.01	20.35±2.25	0.14	0.85	0.01	2.40
1.65	5.97±0.15	1.35±0.01	18.83±0.67	0.16	0.83	0.01	2.26
2.31	5.65±0.16	1.37±0.01	16.70±0.42	0.16	0.82	0.02	2.36
3.30	5.97±0.15	1.46±0.01	18.32±0.57	0.17	0.81	0.02	2.56

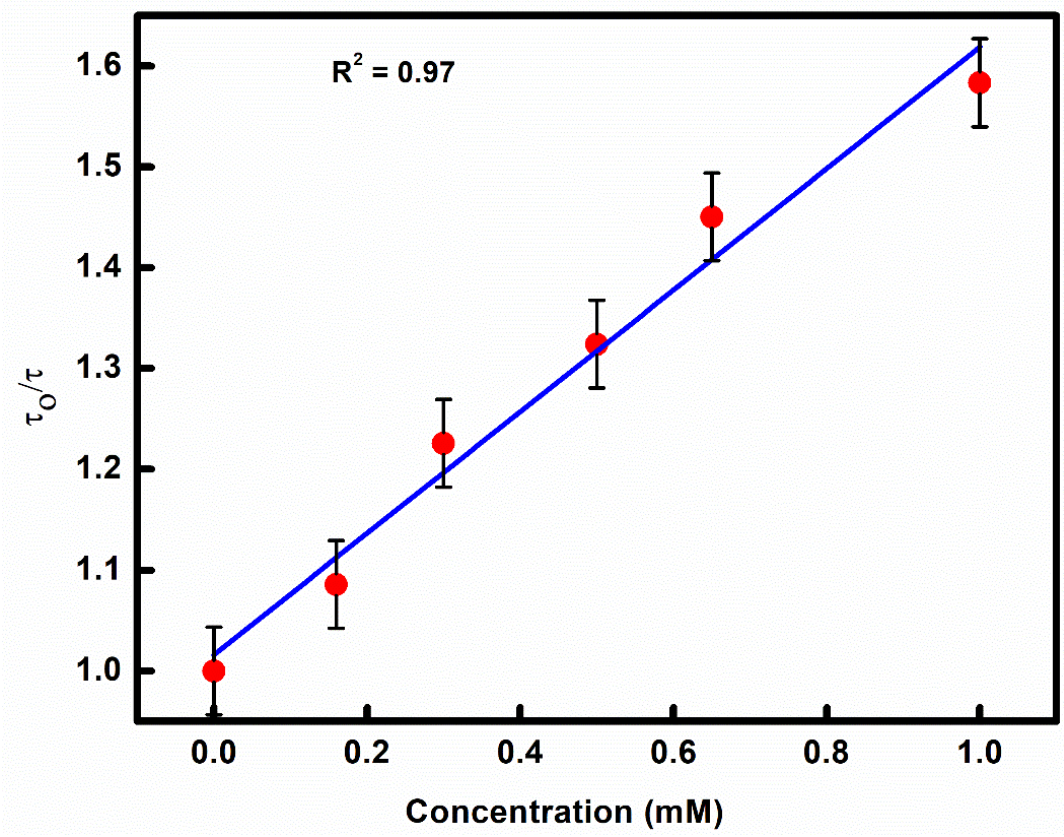

Figure 4.19. *The Stern-Volmer plot between relative PL lifetime of MoS_2 QDs and Pb^{2+} ions concentration.*

4.4.8 Selectivity tests towards Pb^{2+} ions

To test the selectivity of the as-synthesized MoS_2 QDs towards Pb^{+2} metal ions, we have also performed PL titration for other metals ions, such as Ni^{2+}, Cu^{2+}, Fe^{2+}, Ba^{2+}, Fe^{2+}, Zn^{2+}, Co^{2+}, Hg^{2+}, Al^{3+}, Fe^{3+}, *etc*. The percentage of quenching in PL intensity by the individual metal ions is shown in Fig. 4.20. The Hg^{2+} and Fe^{3+} metal ions show considerable PL quenching at initial concentrations and get saturated after quenching (20-40%) of the initial PL intensity. Further, the interference of other metal ions on Pb^{2+} metal ions in water was studied. The PL spectra of MoS_2 QDs were monitored individually at a fixed concentration (1.6 mM) of each metal ion and then with the addition of an equal concentration of Pb^{2+} metal ion. The addition of Pb^{2+} ion prominently quenched the PL intensity of QDs in the presence of other analytes (Fig. 4.21).

The percentage of quenching is almost equal for Pb^{2+} ions in the presence of each of the other metal analytes and maintained nearly the same percentage of quenching (~90%). Hence, no significant interference was observed in the presence of different metal ions on PL quenching of MoS_2 QDs by Pb^{2+}.

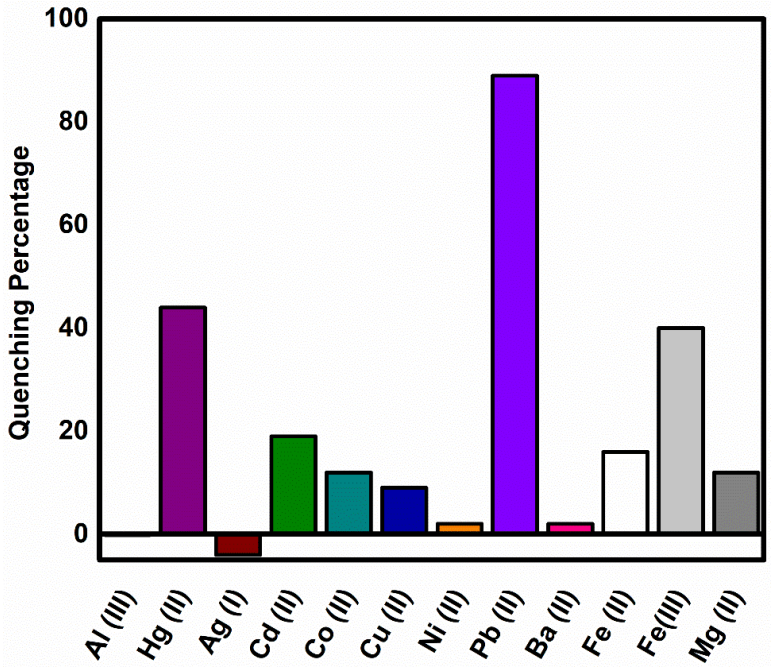

Figure 4.20. *Bar diagram of PL quenching (%) of MoS_2 QDs in the presence of various metal ions in water.*

The absorption spectrum of MoS_2 QDs in the presence of Pb^{2+} shows a significant change. The absolute absorption intensity increases linearly and acts as an absorbance-dependent sensing probe to detect the selected metal ions. This indicates the formation of the complex between functionalized MoS_2 QDs and Pb^{2+} ions in an aqueous medium. The reduction in PL intensity and PL lifetime follows a linear S-V relationship, which indicates that the diffusional quenching is a predominant mechanism. The decrease in PL intensity and lifetime with increasing the concentrations of the Pb^{2+} ions indicates the nonradiative electron-hole recombination-annihilation, *i.e.*, transfer of electron of excited QDs to the metal ions.

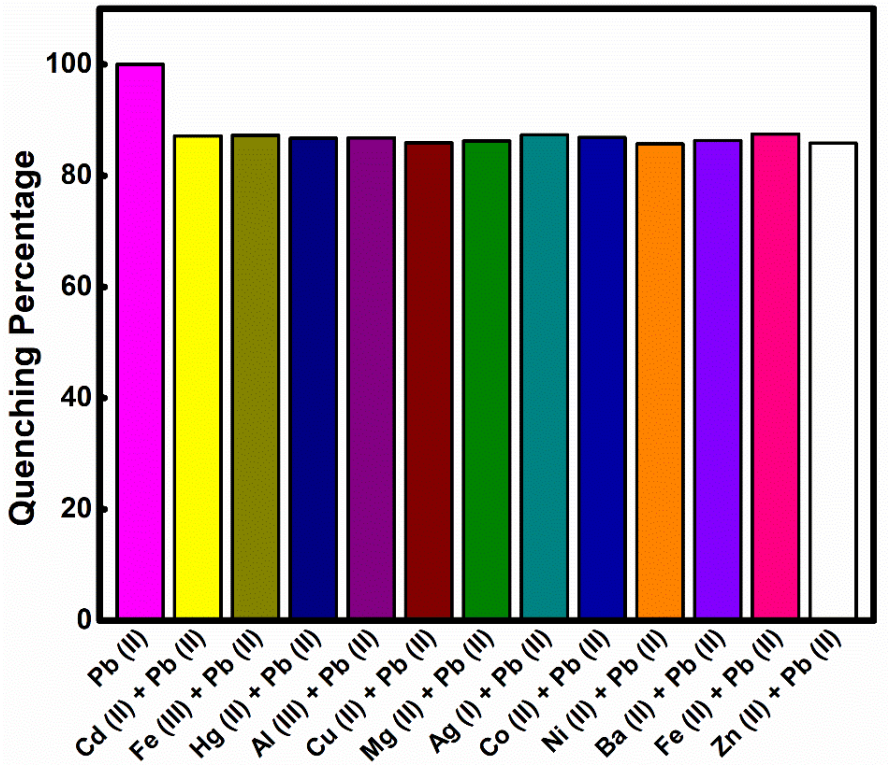

Figure 4.21. *Bar diagram of PL quenching (in %) of MoS_2 QDs in the presence of various metal ions (1.65 mM) together with a fixed concentration of Pb^{2+} ions.*

The electron-deficient nature of Pb^{2+} metal ions binds to the nitrogen donor atoms of the functional group attached over the surface of MoS_2 QDs [55]. An electron transfer process occurs between the excited state of the QDs to the Pb^{2+} ions, which quenches the PL of the QDs [56]. Another plausible quenching pathway might be, i.e., the cation-exchange process, which is usually observed in heavy metal ions, as no red shift was observed in absorption and PL of MoS_2 QDs in the presence of analytes [57]. Also, at high concentration (~6 mM), little aggregation was observed, which might be due to detaching ligands from the surface of QDs and traps the electrons from the conduction band, which leads to the PL quenching. As no red shift was observed in the absorption and PL spectra and no precipitation was observed even at high concentration concludes that the electron transfer from the conduction band of QDs to the

electron-deficient metal ions is the major factor of the PL quenching of the MoS_2 QDs. The quenching of MoS_2 QDs towards selective metal ions also depends on the size of QDs, i.e., the bandgap of QDs. Usually, the sensitivity and selectivity of the QDs towards the analyte depend upon the respective quenching pathways. Here, the Pb^{2+} ions quench PL of large-sized MoS_2 QDs. This study does not support the variation in quenching due to the different sizes of QDs, as HR-TEM analysis exhibit the presence of an inhomogeneous distribution of QDs within the range of 2-5 nm only, hence cannot be considered as the large variation in their size. The interference of other analytes in the presence of Pb^{2+} ions does not show any considerable effect; therefore, it can be concluded that MoS_2 QDs is an effective probe for detecting Pb^{2+} metal ions. On the other hand, the PL quenching by Fe^{3+} ions could be due to the formation of a dark complex with $-NH_2$ group at the surface [58].

4.5 Conclusions

The functionalized MoS_2 QDs were prepared using the facile and highly efficient hydrothermal technique, which provides high-quality quantum dots in large quantities. The size of QDs is in the range of 2 to 5 nm. The FTIR of the MoS_2 QDs demonstrated the presence of Mo-S and N-H vibrational stretching, which confirms the amine functionalization of the MoS_2 QDs. The absorption spectrum of MoS_2 QDs showed a peak at 300 nm with a bandgap of 4.6 eV. The MoS_2 QDs were then analyzed randomly to detect the heavy metal ions and showed a great response with lead metal ions. The absolute absorption intensity of MoS_2 QDs exhibits a linear dependence on the concentration of Pb^{2+} ions, which shows the potential sensing capability of the MoS_2 QDs towards the Pb^{2+} ions. The PL intensity of MoS_2 QDs was quenched significantly in the presence of Pb^{2+} ions and followed a linear S-V relationship for the wide dynamic range of concentrations, i.e., from 33 μM to 8 mM, with a sensitivity (LOD) of 50

μM. The high sensitivity of PL of MoS_2 QDs towards the Pb^{2+} ions was noticed among 13 selected analytes. Thus, the conducted research work has great significance for humans as the presence of lead metal ions in drinking water could cause severe health hazards; therefore, detecting Pb^{2+} ions in the aqueous medium becomes more significant for human well-being.

References

[1] S. Kaviya, S. Kabila, K. V. Jayasree, Room temperature biosynthesis of greatly stable fluorescent ZnO quantum dots for the selective detection of Cr^{3+} ions, Mater. Res. Bull. 95 (2017) 163–168.

[2] A. Jeevika, D.R. Shankaran, Functionalized silver nanoparticles probe for visual colorimetric sensing of mercury, Mater. Res. Bull. 83 (2016) 48–55.

[3] R. Liu, H. Li, W. Kong, J. Liu, Y. Liu, C. Tong, X. Zhang, Z. Kang, Ultra-sensitive and selective Hg^{2+} detection based on fluorescent carbon dots, Mater. Res. Bull. 48 (2013) 2529–2534.

[4] P.Y. Gu, Z. Wang, Q. Zhang, Azaacenes as active elements for sensing and bio applications, J. Mater. Chem. B. 4 (2016) 7060–7074.

[5] Z. Lou, P. Li, K. Han, Redox-responsive fluorescent probes with different design strategies, Acc. Chem. Res. 48 (2015) 1358–1368.

[6] F. Yu, P. Li, G. Li, G. Zhao, T. Chu, K. Han, A near-IR reversible fluorescent probe modulated by selenium for monitoring peroxynitrite and imaging in living cells, J. Am. Chem. Soc. 133 (2011) 11030–11033.

[7] F. Yu, P. Li, B. Wang, K. Han, Reversible near-infrared fluorescent probe introducing tellurium to mimetic glutathione peroxidase for monitoring the redox cycles between peroxynitrite and glutathione in vivo, J. Am. Chem. Soc. 135 (2013) 7674–7680.

[8] P. Sharma, M.S. Mehata, Colloidal MoS_2 quantum dots based optical sensor for detection of 2,4,6-TNP explosive in an aqueous medium, Opt. Mater. (Amst). 100 (2020) 109646.

[9] P. Sharma, M.S. Mehata, Rapid sensing of lead metal ions in an aqueous medium by MoS_2 quantum dots fluorescence turn-off, Mater. Res. Bull. 131 (2020) 110978.

[10] R. Lv, J.A. Robinson, R.E. Schaak, D. Sun, Y. Sun, T.E. Mallouk, M. Terrones, Transition metal dichalcogenides and beyond: Synthesis, properties, and applications of single- and few-layer nanosheets, Acc. Chem. Res. 48 (2015) 56–64.

[11] X. Zhang, Z. Lai, C. Tan, H. Zhang, Solution-Processed Two-Dimensional MoS_2 Nanosheets: Preparation, Hybridization, and Applications, Angew. Chemie - Int. Ed. 55 (2016) 8816–8838.

[12] H. Schmidt, F. Giustiniano, G. Eda, Electronic transport properties of transition metal dichalcogenide field-effect devices: surface and interface effects, Chem. Soc. Rev. 44 (2015) 7715–7736.

[13] K. Kalantar-Zadeh, J.Z. Ou, Biosensors based on two-dimensional MoS_2, ACS Sensors. 1 (2016) 5–16.

[14] R.-Q.Y. and X.C. Jia Ge, En-Cai Ou, A novel aptameric nanobiosensor based on the self-assembled DNA–MoS_2 nanosheet architecture for biomolecule detection, J. Mater. Chem. B. 2 (2014) 625–628.

[15] C. Zhu, Z. Zeng, H. Li, F. Li, C. Fan, H. Zhang, Single-layer MoS_2-based nanoprobes for homogeneous detection of biomolecules, J. Am. Chem. Soc. 135 (2013) 5998–6001.

[16] X. Cao, C. Tan, X. Zhang, W. Zhao, H. Zhang, Solution-processed two-dimensional metal dichalcogenide-based nanomaterials for energy storage and conversion, Adv. Mater. 28 (2016) 6167–6196.
[17] T. Lin, J. Wang, L. Guo, F. Fu, Fe_3O_4@MoS_2 core-shell composites: Preparation, characterization, and catalytic application, J. Phys. Chem. C. 119 (2015) 13658–13664.
[18] C.N.R. Rao, K. Gopalakrishnan, U. Maitra, Comparative study of potential applications of graphene, MoS_2, and other two-dimensional materials in energy devices, sensors, and related areas, ACS Appl. Mater. Interfaces. 7 (2015) 7809–7832.
[19] Q. Lu, Y. Yu, Q. Ma, B. Chen, H. Zhang, 2D transition-metal-dichalcogenide-nanosheet-based composites for photocatalytic and electrocatalytic hydrogen evolution reactions, Adv. Mater. 28 (2016) 1917–1933.
[20] K. Qi, S. Yu, Q. Wang, W. Zhang, J. Fan, W. Zheng, X. Cui, Decoration of the inert basal plane of defect-rich MoS_2 with Pd atoms for achieving Pt-similar HER activity, J. Mater. Chem. A. 4 (2016) 4025–4031.
[21] G. Eda, H. Yamaguchi, D. Voiry, T. Fujita, M. Chen, M. Chhowalla, Photoluminescence from chemically exfoliated MoS_2, Nano Lett. 11 (2011) 5111–5116.
[22] K.F. Mak, C. Lee, J. Hone, J. Shan, T.F. Heinz, Atomically Thin MoS_2 : A new direct-gap semiconductor, Phys. Rev. Lett. 105 (2010) 136805.
[23] D. Gopalakrishnan, D. Damien, M.M. Shaijumon, MoS_2 quantum dot-interspersed exfoliated MoS_2 nanosheets, ACS Nano. 8 (2014) 5297–5303.
[24] H.D. Ha, D.J. Han, J.S. Choi, M. Park, T.S. Seo, Dual role of blue luminescent MoS_2 quantum dots in fluorescence resonance energy transfer phenomenon, Small. 10 (2014) 3858–3862.
[25] Y.N. Wang, P. Zhang, J.H. Yu, J.Q. Xu, 4-(4-Carboxyphenoxy)phthalate-based coordination polymers and their application in sensing nitrobenzene, Dalt. Trans. 44 (2015) 1655–1663.
[26] H. Lin, C. Wang, J. Wu, Z. Xu, Y. Huang, C. Zhang, Colloidal synthesis of MoS_2 quantum dots: Size-dependent tunable photoluminescence and bioimaging, New J. Chem. 39 (2015) 8492–8497.
[27] H. Dong, S. Tang, Y. Hao, H. Yu, W. Dai, G. Zhao, Y. Cao, H. Lu, X. Zhang, H. Ju, Fluorescent MoS_2 quantum dots: ultrasonic preparation, up-conversion and down-conversion bioimaging, and photodynamic therapy, ACS Appl. Mater. Interfaces. 8 (2016) 3107–3114.
[28] Y. Wang, Y. Ni, Molybdenum disulfide quantum dots as a photoluminescence sensing platform for 2,4,6-trinitrophenol detection, Anal. Chem. 86 (2014) 7463–7470.
[29] R. Feyisa Bogale, J. Ye, Y. Sun, T. Sun, S. Zhang, A. Rauf, C. Hang, P. Tian, G. Ning, Highly selective and sensitive detection of metal ions and nitroaromatic compounds by an anionic europium(III) coordination polymer, Dalt. Trans. 45 (2016) 11137–11144.
[30] J.Z. Ou, A.F. Chrimes, Y. Wang, S.Y. Tang, M.S. Strano, K. Kalantar-Zadeh, Ion-driven photoluminescence modulation of quasi-two-dimensional MoS_2 nanoflakes for

applications in biological systems, Nano Lett. 14 (2014) 857–863.
[31] S. Xu, D. Li, P. Wu, One-pot, facile, and versatile synthesis of monolayer MoS_2 /WS_2 quantum dots as bioimaging probes and efficient electrocatalysts for hydrogen evolution reaction, Adv. Funct. Mater. 25 (2015) 1127–1136.
[32] X.Q. Qiao, Z.W. Zhang, F.Y. Tian, D.F. Hou, Z.F. Tian, D.S. Li, Q. Zhang, Enhanced catalytic reduction of p-nitrophenol on ultrathin MoS_2 nanosheets decorated with noble metal nanoparticles, Cryst. Growth Des. 17 (2017) 3538–3547.
[33] W. Gu, Y. Yan, C. Zhang, C. Ding, Y. Xian, One-step synthesis of water-soluble MoS_2 quantum dots via a hydrothermal method as a fluorescent probe for hyaluronidase detection, ACS Appl. Mater. Interfaces. 8 (2016) 11272–11279.
[34] D.R. Hang, D.Y. Sun, C.H. Chen, H.F. Wu, M.M.C. Chou, S.E. Islam, K.H. Sharma, Facile bottom-up preparation of WS_2-based water-soluble quantum dots as luminescent probes for hydrogen peroxide and glucose, Nanoscale Res. Lett. 14 (2019).
[35] H. Swaminathan, K. Balasubramanian, Förster resonance energy transfer between MoS_2 quantum dots and polyaniline for turn-on bovine serum albumin sensing, Sensors Actuators, B Chem. 264 (2018) 337–343.
[36] X. Liu, W. Zhang, L. Huang, N. Hu, W. Liu, Y. Liu, S. Li, C. Yang, Y. Suo, J. Wang, Fluorometric determination of dopamine by using molybdenum disulfide quantum dots, Microchim. Acta. 185 (2018) 1–8.
[37] Q. Wu, X. Wang, Y. Jiang, W. Sun, C. Wang, M. Yang, C. Zhang, MoS_2-QD-based dual-model photoluminescence sensing platform for effective determination of Al^{3+} and Fe^{3+} simultaneously in various environment, ChemistrySelect. 3 (2018) 2326–2331.
[38] X. Li, D.W. He, Y.S. Wang, Y. Hu, X. Zhao, C. Fu, J.Y. Wu, Facile and controllable synthesis of molybdenum disulfide quantum dots for highly sensitive and selective sensing of copper ions, Chinese Phys. B. 27 (2018).
[39] H. Cao, H. Wang, Y. Huang, Y. Sun, S. Shi, M. Tang, Quantification of gold(III) in solution and with a test stripe via the quenching of the fluorescence of molybdenum disulfide quantum dots, Microchim. Acta. 184 (2017) 91–100.
[40] L. Hu, Q. Zhang, X. Gan, W. Yin, W. Fu, Switchable fluorescence of MoS_2 quantum dots: a multifunctional probe for sensing of chromium(VI), ascorbic acid, and alkaline phosphatase activity, Anal. Bioanal. Chem. 410 (2018) 7551–7557.
[41] R.K. Ratnesh, M.S. Mehata, Investigation of biocompatible and protein sensitive highly luminescent quantum dots/nanocrystals of CdSe, CdSe/ZnS and CdSe/CdS, Spectrochim. Acta - Part A Mol. Biomol. Spectrosc. 179 (2017) 201–210.
[42] RS_2, Potable water specification, 2nd Ed, Rwanda Bureau of standard, kigali, 2012.
[43] H. Cao, Y. Huang, Y. Xie, W. Shi, C. Fu, W. He, A fast-responsive fluorescent probe for sensitive detection of graphene oxide based on MoS_2 quantum dots, Analyst 143 (2018) 3107-3113.
[44] B. Gu, Q. Zhang, Recent advances on functionalized upconversion nanoparticles for detection of small molecules and ions in biosystems, Adv. Sci. 5 (2018) 1700609.

[45] H. Bradl, C. Kim, U. Kramar, D. StÜben, Heavy metals in the environment: origin, interaction and remediation, Interface Sci. Technol. 6 (2005) 28–164.
[46] P.B. Tchounwou, C.G. Yedjou, A.K. Patlolla, D.J. Sutton, Molecular, clinical and environmental toxicicology Volume 3: Environmental Toxicology, 2012.
[47] M.K. Singh, M.S. Mehata, Phase-dependent optical and photocatalytic performance of synthesized titanium dioxide (TiO_2) nanoparticles, Optik (Stuttg). 193 (2019) 163011.
[48] D. Haldar, D. Dinda, S.K. Saha, High selectivity in water soluble MoS_2 quantum dots for sensing nitro explosives, J. Mater. Chem. C. 4 (2016) 6321–6326.
[49] J. Yang, W. Chen, X. Liu, Y. Zhang, Y. Bai, Hydrothermal synthesis and photoluminescent mechanistic investigation of highly fluorescent nitrogen doped carbon dots from amino acids, Mater. Res. Bull. 89 (2017) 26–32.
[50] M.S. Mehata, R.K. Ratnesh, Luminescence properties and exciton dynamics of core-multi-shell semiconductor quantum dots leading to QLEDs, Dalt. Trans. 48 (2019) 7619–7631.
[51] D. Pan, J. Zhang, Z. Li, M. Wu, Hydrothermal route for cutting graphene sheets into blue-luminescent graphene quantum dots, Adv. Mater. 22 (2010) 734–738.
[52] T. Werner, G. Sweetman, M.F. Savitski, T. Mathieson, M. Bantscheff, M.M. Savitski, Ion coalescence of neutron encoded TMT 10-plex reporter ions, Anal. Chem. 86 (2014) 3594–3601.
[53] W. Dai, H. Dong, B. Fugetsu, Y. Cao, H. Lu, X. Ma, X. Zhang, Tunable fabrication of molybdenum disulfide quantum dots for intracellular microrna detection and multiphoton bioimaging, Small. 11 (2015) 4158–4164.
[54] W. Xiao, W. Zhou, T. Feng, Y. Zhang, H. Liu, L. Tian, Simple synthesis of molybdenum disulfide/reduced graphene oxide composite hollow microspheres as supercapacitor electrode material., Mater. (Basel, Switzerland). 9 (2016) 783.
[55] P. Wu, X.-P. Yan, Ni^{2+}-modulated homocysteine-capped CdTe quantum dots as a turn-on photoluminescent sensor for detecting histidine in biological fluids, Biosens. Bioelectron. 26 (2010) 485–490.
[56] J. Duan, X. Jiang, S. Ni, M. Yang, J. Zhan, Facile synthesis of N-acetyl-l-cysteine capped ZnS quantum dots as an eco-friendly fluorescence sensor for Hg^{2+}, Talanta. 85 (2011) 1738–1743.
[57] T.T. Gan, Y.J. Zhang, N.J. Zhao, X. Xiao, G.F. Yin, S.H. Yu, H.B. Wang, J.B. Duan, C.Y. Shi, W.Q. Liu, Hydrothermal synthetic mercaptopropionic acid stabled CdTe quantum dots as fluorescent probes for detection of Ag^{+}, Spectrochim. Acta Part A Mol. Biomol. Spectrosc. 99 (2012) 62–68.
[58] M. Karimi, A. Badiei, G.M. Ziarani, A novel naphthalene-immobilized nanoporous SBA-15 as a highly selective optical sensor for detection of Fe^{3+} in water, J. Fluoresc. 25 (2015) 1297–1302.

CHAPTER 5

Synthesis of pristine MoS_2 nanosheets and their applications *

5.1. Introduction

Nowadays, water pollution has become a great concern for human beings and the environment [1]. The increased industrialization has led to the dumping of untreated hazardous organic pollutants directly into the water bodies (rivers, ponds, etc.), affecting the water quality and aquatic life [2–4]. Therefore, the detection of toxic compounds (like heavy metal ions, organic compounds, nitro explosives, etc.) and the degradation of organic compounds under illumination possess great significance for the betterment of the ecosystem [5–7]. The photocatalysis process is one of the most extensively studied oxidation processes because of its numerous environmental applications as hydrogen evolution, organic compounds degradation, pharmaceutical waste removal, dye degradation, *etc*. Usually, metal oxides (TiO_2, ZnO, SnO_2, etc.) are used as photocatalysts because of their high stability, efficient photoactivity, cost-effective production, and non-toxic behaviour [8–10]. Despite these outstanding features, the bandgap of the metal oxides lies in the ultraviolet (UV) region [9]. Therefore, an alternative for the metal oxides is constantly being searched due to its narrow window of excitation wavelengths, i.e., the ultraviolet (UV) region consists of only 5% of the natural sunlight.

* Part of this work has been published in the **Journal of Molecular Structure 1249 (2022) 131651.**

The molybdenum disulfide (MoS_2) is the most studied layered transition metal dichalcogenide (LTMD). In the past few decades, it has been the research notion in the scientific community because of its structural similarity with graphene [5,7].

The two-dimensional (2D) structure of MoS_2 possesses excellent electronic and optical properties with greater surface area. The MoS_2 nanosheets can be implied to a wide range of applications like photocatalysis, transistors, supercapacitors, gas sensing, catalysis, photo-detectors, batteries and optoelectronic devices [10-25]. The structure of MoS_2 nanosheets consists of strong intra-layer covalent bonding between Molybdenum (Mo) and Sulfur (S) atoms in the trigonal prismatic arrangement, where the Mo atoms possess the hexagonal plane, which is packed between the two hexagonal planes of S atoms. The interlayer MoS_2 stackings are strengthened with the weak Van der Waals forces [27], as shown in Fig. 5.1. Due to the weak interlayer bonding, the production of ultrathin nanosheets is possible with the micro-mechanical cleavage technique, as demonstrated by Novoselov *et al.* [28]. But it is quite challenging to produce a high yield of MoS_2 monolayer through microexfoliation. The weak interlayer interactions in MoS_2 nanosheets led the incorporated ions or molecules to be introduced between the layers through intercalation. Therefore, MoS_2 could be formed as an intercalation host in terms to deliver a promising alternate electrode material in high energy density batteries.

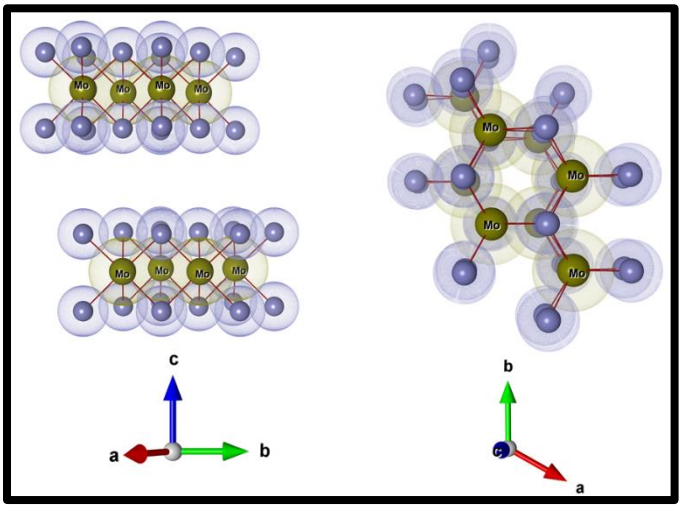

Figure 5.1. *The molecular structure of the MoS_2 nanosheets.*

Despite the structural similarity with graphene, the MoS_2 shows distinct semiconducting properties as the monolayer MoS_2 has a bandgap of 1.9 eV (direct bandgap), while the bulk MoS_2 has 1.3 eV (indirect bandgap), as compared to the graphene, which has zero bandgaps [29]. This indirect to direct bandgap transition originated due to the quantum confinement effect. The photoluminescence property of MoS_2 occurred because of the large bandgap, which made it an active photocatalyst in the visible range [30]. The pristine MoS_2 nanosheets have shown great photocatalytic activity towards the CV dye due to low bandgap energy, high surface to volume ratio, multiple active edge sites. To synthesize MoS_2 nanosheets, the facile hydrothermal technique was used because of its ability to produce a huge amount of good quality nanosheets.

Here in this work, the pristine MoS_2 nanosheets were synthesized by the facile hydrothermal process and investigated with different techniques. The hexamethyl pararosaniline chloride, popularly known as crystal violet (CV) dye or methyl violet 10B developed by the German chemist's Kern and Caro, is degraded through photocatalysis using MoS_2 nanosheets as catalyst or photocatalyst. The crystal violet dye has a vast range of medical, non-medical, and veterinary applications. Instead of its beneficial properties, the dye has been listed as unsafe for animal feed by the food and drug administration (FDA) in the United States, intended for human consumption. The continuous use of CV destroys the consumable water resources as they are dumped directly into rivers through sewage systems without the proper treatment. Therefore, the degradation of the waste dye makes the work more significant given for human and environmental benefit.

5.2. Materials and Method:

5.2.1. Materials used:

All the reagents were purchased from Sigma Aldrich and CDH chemicals of analytical (AR) grades. The ammonium heptamolybdate tetrahydrate ($(NH_4)_6Mo_7O_{24}.4H_2O$), the Mo source was purchased from Sigma Aldrich and the thiourea as sulfur (S) source was purchased from CDH chemicals. The citric acid from CDH chemicals was used as a reducing agent. The crystal violet dye has been purchased from CDH chemicals. The ultrapure de-ionized water (DI) has been used during the whole experiment with a resistivity of 18.2 MΩ cm.

5.2.2. Experimental Method:

A facile hydrothermal route has been opted to synthesize the MoS_2 nanosheets. Here, 1.0 g of ammonium hepta-molybdate tetrahydrate (AHM) and 0.5g of citric acid were dissolved in 60 ml of de-ionized (DI) water for 1 h in an argon atmosphere. The citric acid will aid the MoS_2 nanosheets to grow by reducing Mo (VI) to Mo (IV). Then, 1.2 g of thiourea is mixed into the

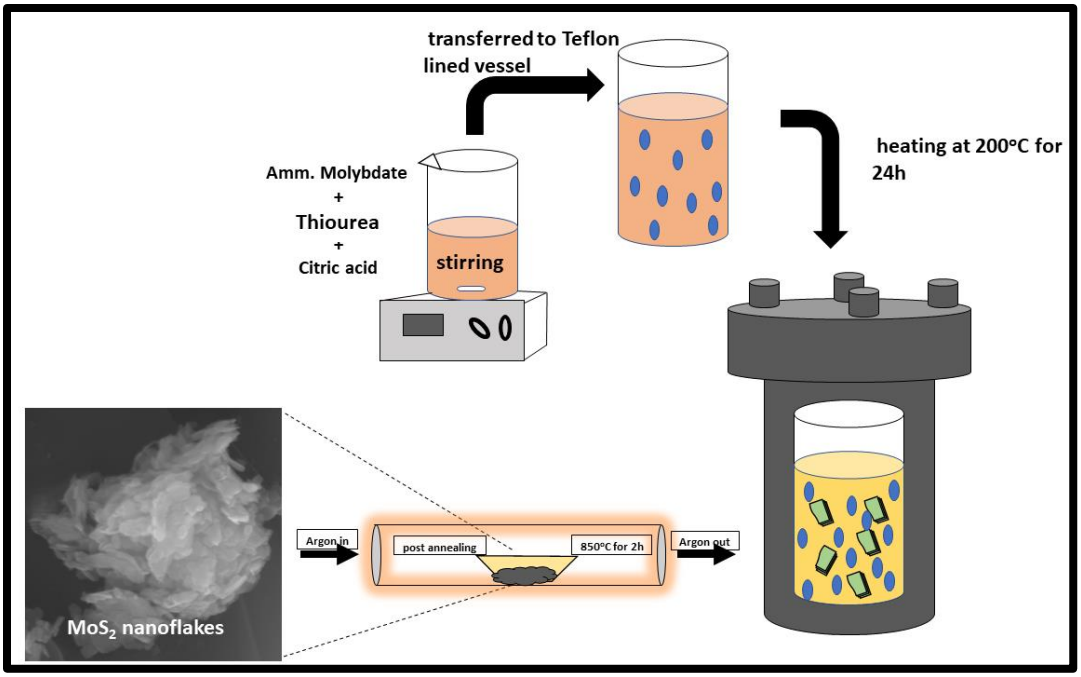

Figure 5.2. *Schematic representation of hydrothermal synthesis process of MoS_2 nanosheets.*

solution and the final solution are kept at 60 ^{o}C with stirring for another 1 h. After that, the solution is transferred to the Teflon-lined hydrothermal reactor (of capacity ~100 mL), treated at 200 ^{o}C for 24 h and allowed to cool down naturally to room temperature. The obtained black precipitates were centrifuged at 5000 rpm for 20 min few times with DI and ethanol to remove the excess chelating agent and the unreacted precursors. Then, the precipitates were dried at 60 ^{o}C for 12 h in a hot air oven. To achieve highly crystalline MoS_2 nanosheets, the finally obtained black powder was annealed under the inert environment in a tubular furnace at 850 ^{o}C for 2 h, as shown in Fig. 5.2. The reaction that occurred during the process is as follows [31]:

$$CH_4N_2S + 2H_2O = CO_2\uparrow + 2NH_3\uparrow + H_2S\uparrow \quad (5.1)$$

$$(NH_4)_6Mo_7O_{24}.4H_2O + 28H_2S + 8NH_3 = 7(NH_4)_2MoS_4 + 28H_2O \quad (5.2)$$

$$5O_2 + 2N_2 + 2C_6H_8O_7 + 2(NH_4)_2MoS_4 = 2MoS_2 + 12CO_2 + 4(NH_4)_2S \quad (5.3)$$

Eq. (5.1) describes the sulfurated reaction while Eq. (5.2) shows the formation of intermediate compound $(NH_4)_2MoS_4$, which is a rare compound and hard to find; therefore, the AHM is used as its inexpensive alternate. Then finally, the reduction process of $(NH_4)_2MoS_4$ takes place to form MoS_2. The sulfurization and reduction processes are vital for MoS_2 nanosheets without forming intermediate products like MoO_2 or MoO_3 [32,33].

5.3. Characterization technique

The powder XRD Ultima IV, Rigaku equipped with CuKα radiation (λ = 0.15406 nm) applied at 20 mA, was used to record the X-ray diffraction (XRD) pattern at an accelerating voltage of 35 kV. The synthesized nanosheet's surface morphology was recorded by the Zeiss EVO40 scanning electron microscopy (SEM) technique at an accelerating voltage of 0.1-30 kV. The TALOS, Thermo scientific instruments, used to record the high-resolution transmission

electron microscope (HR-TEM) images operated at an accelerating 200 kV. The spectrum (II) (Perkin Elmer) was used to record Fourier transform infrared spectroscopy (FT-IR) spectrum in the range from 450 cm^{-1} to 4000 cm^{-1}. The UV/VIS/NIR spectrometer by Lambda-750, Perkin-Elmer, was used to record the UV-visible absorption spectra for the overall measurements.

5.4. Results and discussion

5.4.1. X-ray diffraction (XRD) pattern

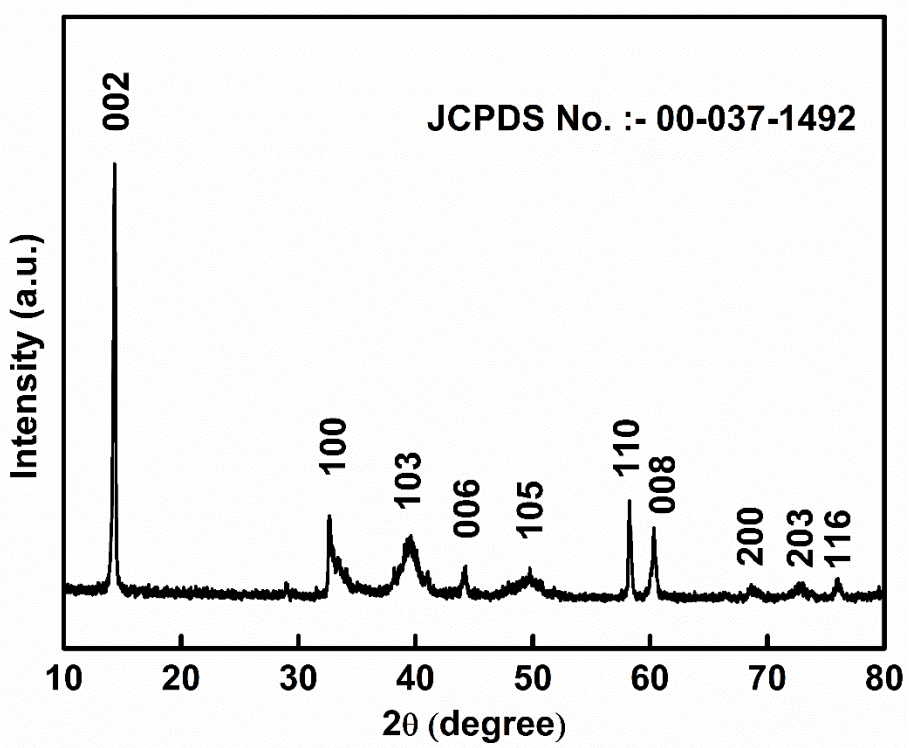

Figure 5.3. *The XRD pattern of the synthesized MoS_2 nanosheets.*

The XRD pattern of the as-synthesized MoS_2 NS was recorded by Cu Kα (λ = 1.54 Å) ranging from 10° to 80° with a given step size of 0.02° (2θ), as shown in Fig. 5.3. The observed XRD pattern showed the high crystallinity having hexagonal structure (2H-MoS_2) compared with the reference pattern of JCPDS card no. 0037-1492. The highly intensive peak (002) at 2θ =

14.28° depicts that the layered structure of MoS_2 has been stacked orderly along the plane with a d-spacing of 0.61 nm along a plane (002). Therefore, the peaks were observed at (002), (006) and (008) positioned at 2θ =14.28°, 44.21°, and 60.31° represents the layered structure of the material. The diffraction pattern indicates the absence of any impure phase in as-prepared MoS_2 nanosheets. The crystallite size of the MoS_2 nanosheets was calculated by employing Scherrer's formula, as given in Equation (5.4):

$$\boldsymbol{D = \frac{0.9\lambda}{\beta\ \mathrm{Cos}\theta}} \qquad (5.4)$$

where λ illustrates the x-ray source wavelength (CuKα, λ = 0.154 nm) and β represents the full width at half maximum (FWHM) of the high-intensity peak (Radian), θ is the Bragg's diffraction angle. Using Eq. (5.4), the crystallite size estimated was 33 nm (for 2θ = 14.28° and β = 0.240).

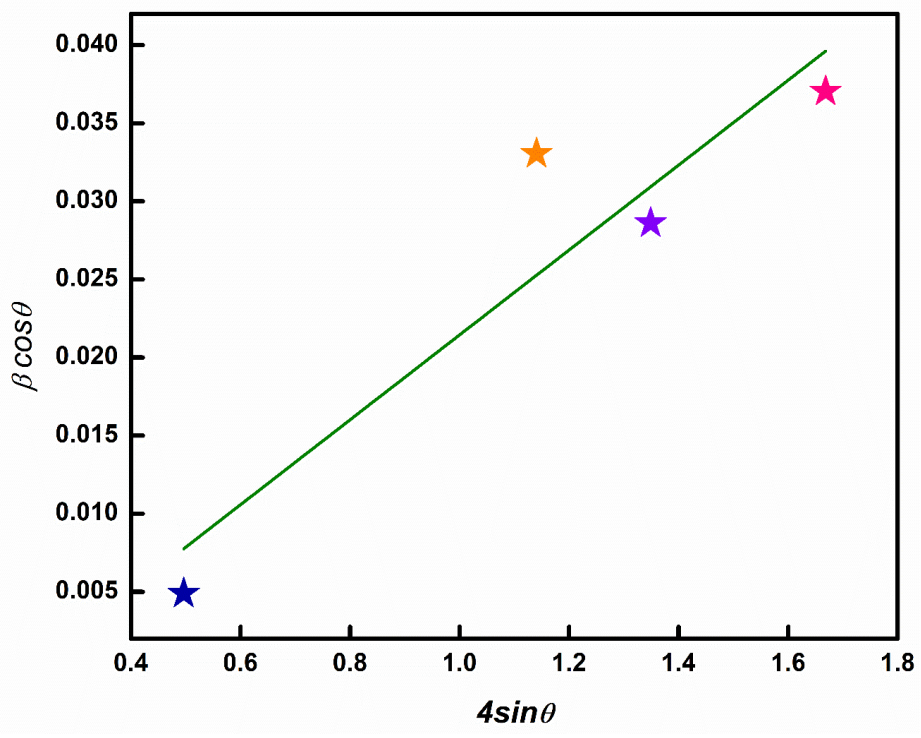

Figure 5.4. *The Williamson-Hall plot for the synthesized MoS_2 nanosheets.*

Fig. 5.4 represents the Williamson-Hall (W-H) plot between the $\beta cos\theta$ and $4sin\theta$ for the MoS_2 NSs to determine the average crystallite size and the micro-strain (ε) using the relation Eq (5.5).

$$\boldsymbol{\beta cos\theta = 4\varepsilon sin\theta + \frac{k\lambda}{D}} \quad (5.5)$$

where k illustrates the shape factor having a value be 0.9. The peaks at planes (002), (001), (103) and (100) were considered for calculating D and ε of MoS_2 NSs. The value of the microstrain of MoS_2 estimated from the linear fitted W-H plot is 0.027. Whereas the average crystallite size from the W-H plot was calculated to be ~ 24 nm.

5.4.2. Scanning electron microscope (SEM) images

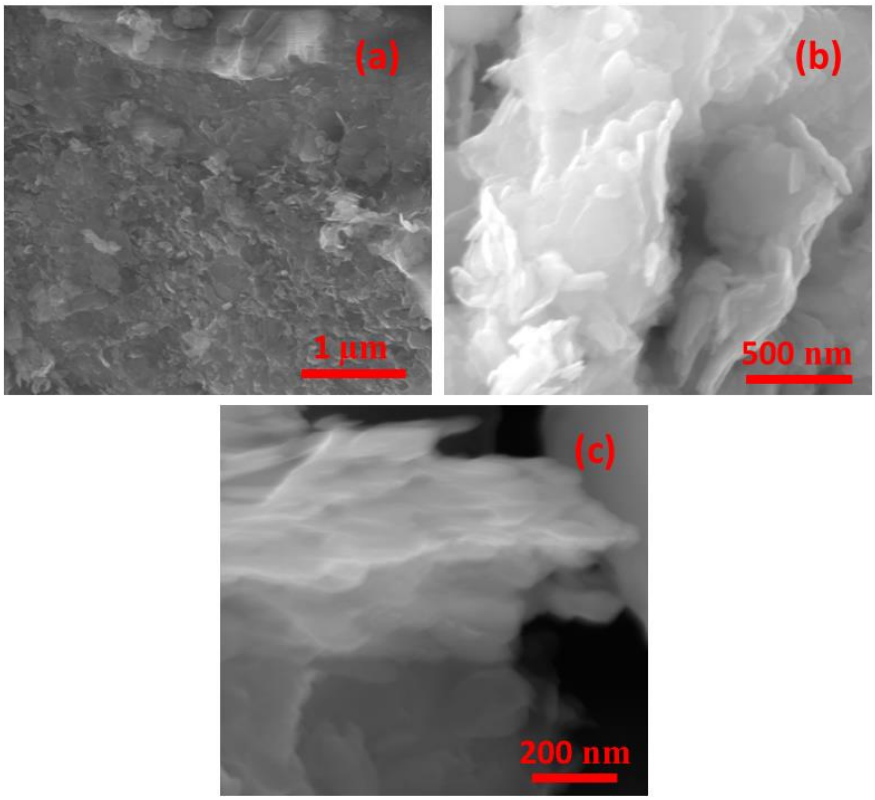

Figure 5.5. *The SEM images at the magnification (a) 50 k×, (b) 100 k× and (c) 200 k× of MoS_2 nanosheets.*

Fig. 4 represents the SEM images for the synthesized nanosheets formed in the presence of citric acid as a reducing agent. The images of Fig. 5.5 (a, b, and c) were recorded at 50, 100 and 200 k× magnifications, clearly show the presence of flakes-like structures. These structures were growing inconsistently in all directions, rendering to the rough surface morphology.

5.4.3. High-resolution transmission electron microscope (HRTEM) images

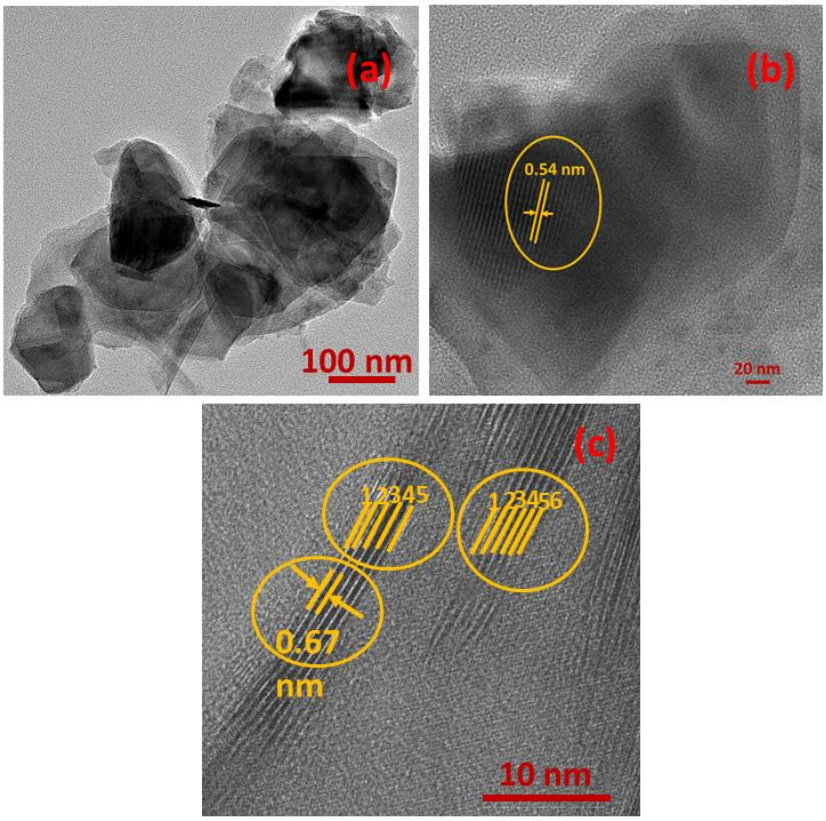

Figure 5.6. *The TEM image (a) and HR-TEM images (b and c) of MoS_2 nanosheets.*

The typical HR-TEM was carried out to record the highly magnified images of the MoS_2, as shown in Fig. 5. HR-TEM was recorded on copper TEM grids with carbon coating on which a drop of sample dispersed in DI was loaded. Fig. 5.6(a) demonstrates the number of nanosheets stacked over one another. Fig. 5.6(b) illustrates the crystalline structure of MoS_2, with its orderly patterned fringes, which confirms the crystalline structure. The 'd' is the inter-

planar spacing came out to be 0.54 nm, similar to the value calculated from the XRD pattern. Fig. 5.6(c) represents the presence of 5-6 layers in the synthesized nanosheets, which would lead to high adsorption and a greater surface-to-volume ratio.

5.4.4. Fourier transform infrared (FTIR) spectrum

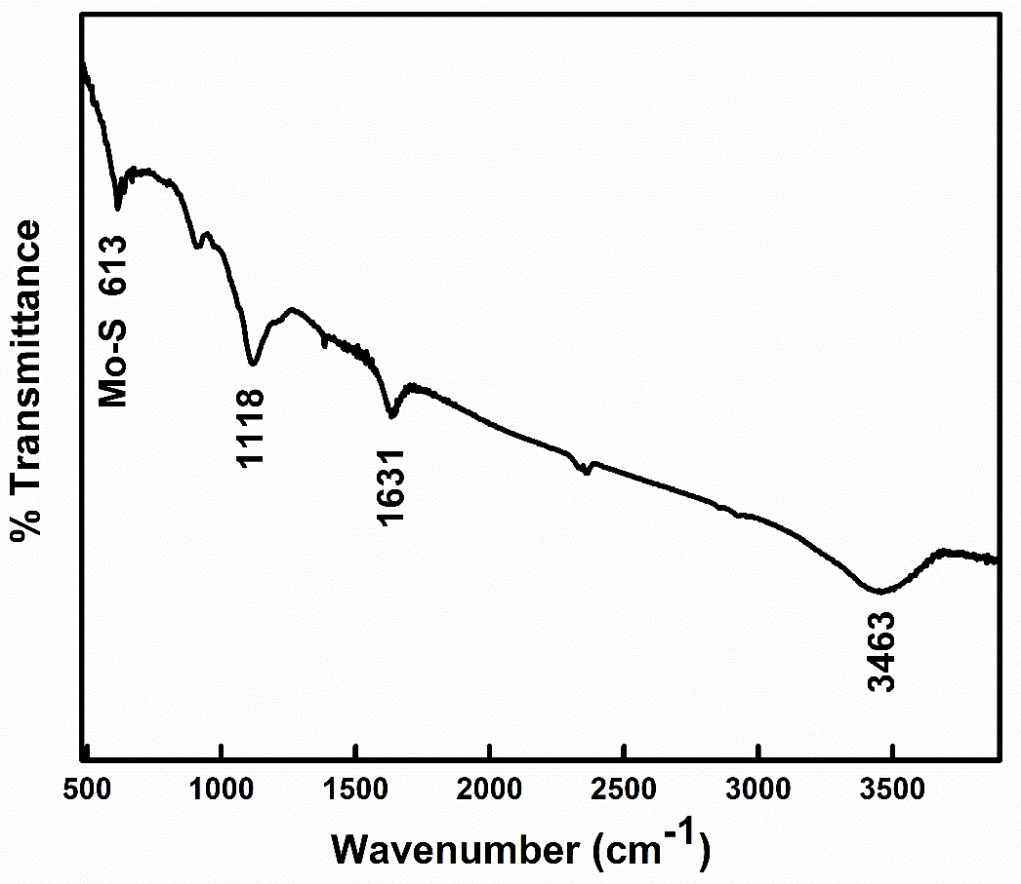

Figure 5.7. *The FT-IR spectrum of the MoS_2 nanosheets.*

Fig. 5.7 shows FTIR spectrum of as-synthesized MoS_2 layered structure. The spectrum describes the chemical characteristics of the material. The characteristic weak bands appeared at 1118 cm^{-1} and 613 cm^{-1} due to the S-S bonds and Mo-S bonds stretching vibrations, respectively. The vibrational bands observed at 3463 cm^{-1} and 1631 cm^{-1} attribute to the

stretching and the bending mode of vibrations of O-H bonds of water molecules absorbed on the surface due to the hygroscopic nature of KBr.

5.4.5. UV-visible absorption spectroscopy

UV-visible absorption spectroscopy is a vital measurement technique required to characterize the material's electronic band structures. Fig. 5.8 represents the UV-vis absorption spectrum of the as-synthesized MoS_2 NSs. Here in the absorption spectrum, the characteristic absorption bands of MoS_2, i.e., A, B, C and D, are visible at wavelength 678 nm, 624 nm, 458 nm and 406 nm, respectively. The absorption bands at the 678 nm and 624 nm are because of the excitonic transitions of the first and second Brillouin zones at the points K/K', while the absorption bands at 458 and 406 nm (C & D) are because of the electronic transitions from the valence to the conduction bands. The energy bandgap calculated to be 2.07 eV using the well-known Tauc's plot relation (as shown in the inset of Fig. 5.8) as given in Eq. (5.8):

$$Ahv = A(hv - E_g)^n \quad (5.8)$$

where A is a constant, Eg illustrates the bandgap of the material, hv is the photon energy incident on the specimen, n is the transition coefficient (n= ½ for Direct bandgap) depending on the nature of semiconductor material.

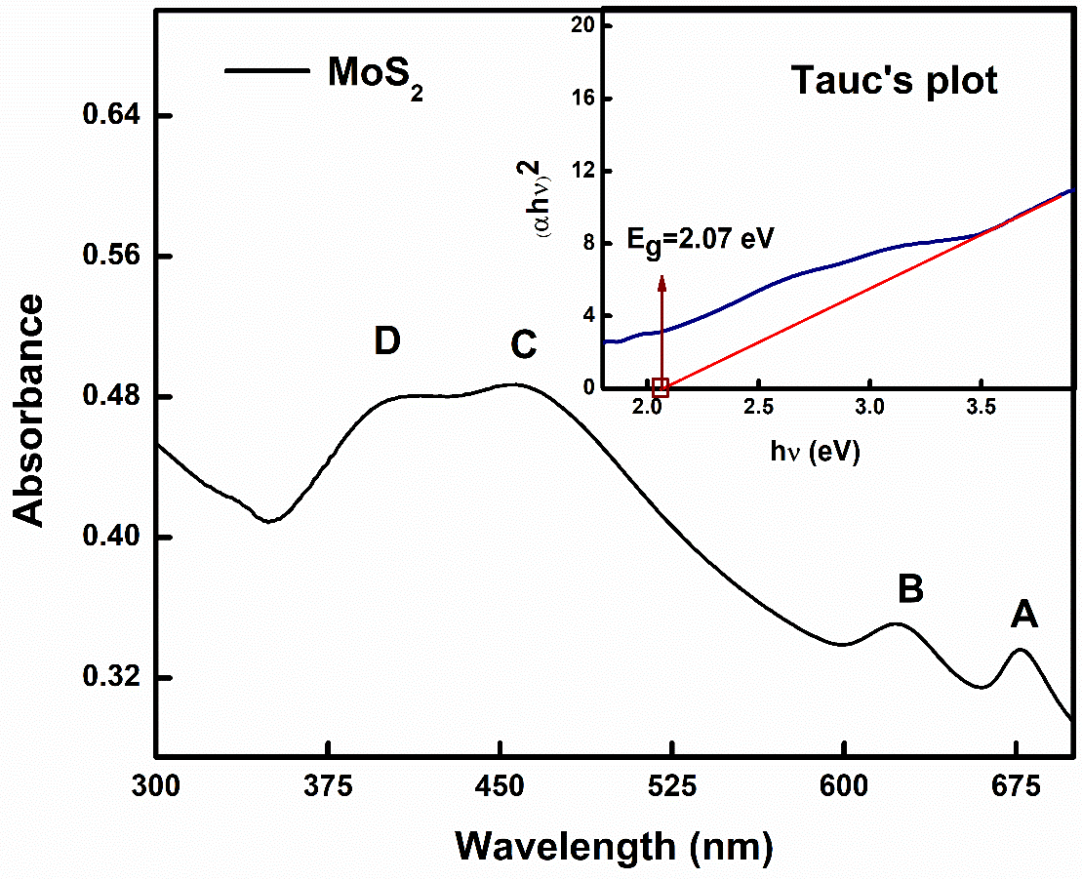

Figure 5.8. *The absorption spectrum of pristine MoS_2 nanosheets dispersed in water. The inset shows the corresponding Tauc's plot.*

5.5. Dye degradation activity of MoS_2

The dye degradation capabilities of MoS_2 nanosheets were performed with the crystal violet dye in sunlight irradiation. The intensity of the sunlight on the day of testing was recorded to be 38-48 kLux (Latitude 28° 37' 56.7444" N and Longitude 77° 13' 7.6368" E). The UV-visible absorption spectroscopy was used to record the degradation process by measuring the variation (decrement) in the absorbance of the dye. The initial concentration of dye was taken as 4.0×10^{-5} M having an absorption intensity of 0.73 (absorbance) at λ_{max} = 581 nm. The dye solution was tested for its photoactivity in the sunlight, where no change in the absorbance value was observed. Subsequently, the absorption spectra of dye were recorded in the presence of

synthesized MoS_2 nanosheets upon irradiation with a halogen lamp having the intensity of 30 kLux, UV illumination, and sunlight. The results of the degradation of dye under different conditions were compared.

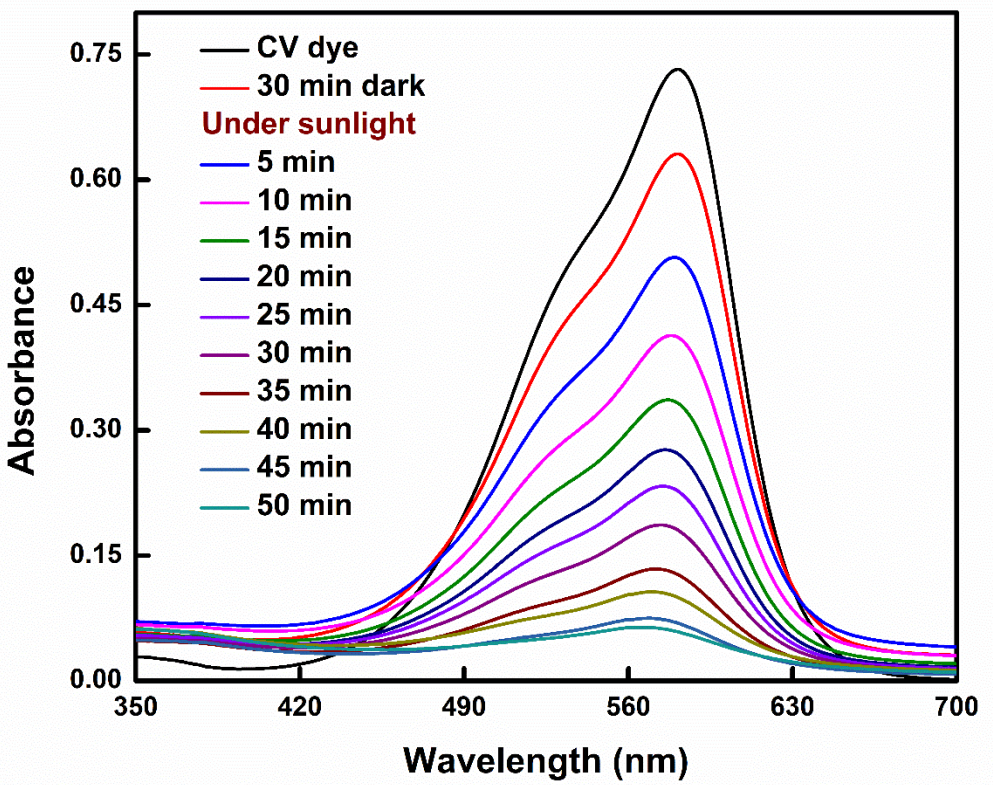

Figure 5.9. *The absorption spectra of CV dye in the presence of MoS_2 nanosheets under solar illumination.*

For photocatalytic activity (PCA) of NSs, the crystal violet dye solution was prepared and kept in a dark place. The absorption spectrum of the CV dye was recorded. Then 5 mg of MoS_2 nanosheets were added to the 50 ml of the CV dye solution and stirred homogeneously for 30 min in the dark surrounding to achieve adsorption/desorption equilibrium. Then, 10-12 mL of the mixture was extracted from the solution and centrifuged at 5000 rpm for 2 min to separate the large catalyst particles. After this, the absorption spectrum was again recorded to measure dye degradation because of adsorption/desorption isotherm. Then, an equal amount

of surfactant was kept under sunlight, halogen light and UV light to examine the effect of the natural and artificial light over the dye solution in the presence of the catalyst.

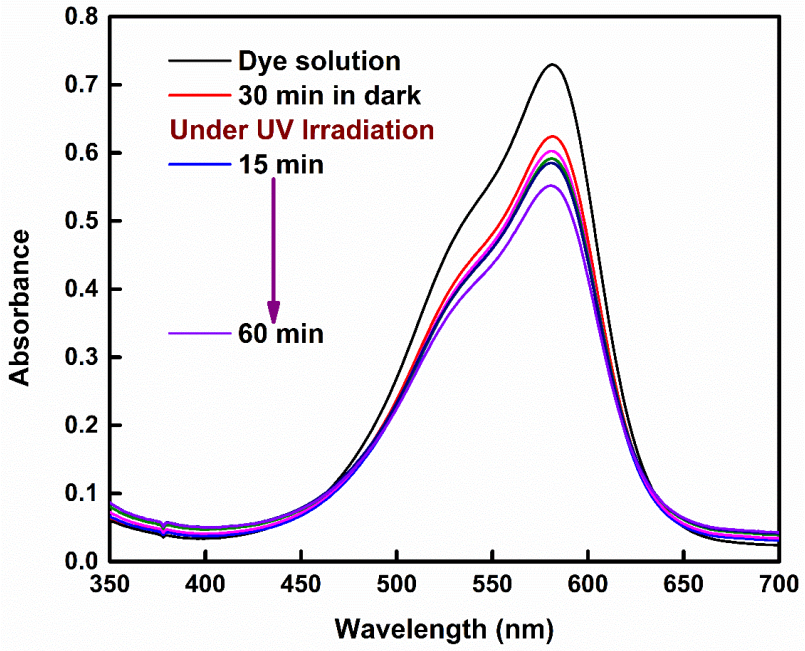

Figure 5.10. *The absorption spectra of dye in the presence of MoS_2 NSs under UV irradiation.*

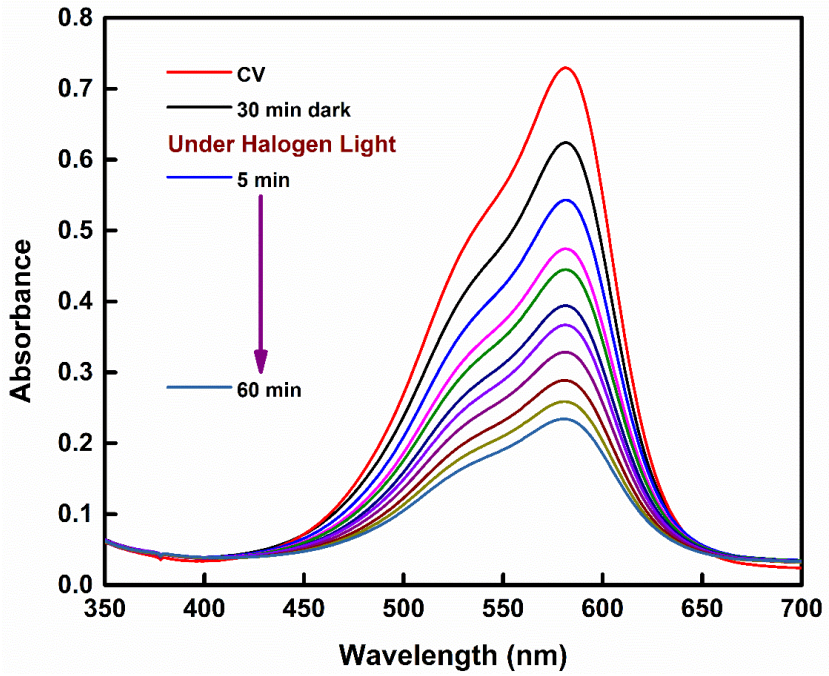

Figure 5.11. *The absorption spectra of the dye in the presence of MoS_2 NSs under halogen irradiation.*

Fig. 5.9 illustrates the absorption spectra of dye solution under solar irradiation in the presence of MoS_2 nanosheets. The dye degradation was observed as a decrease in absorbance of the dye with a time under the solar irradiation in the presence of MoS_2 NSs. It was observed that the dye degraded entirely in 50 min. Similarly, the other two samples were placed under halogen and UV light. Therefore, their absorption spectra were recorded, as shown in figures, Fig. 5.10 and 5.11. It was observed that the complete degradation occurred under natural light (sunlight). In contrast, the halogen and UV light caused some significant change in the absorption intensity of dye but could not degrade it entirely within 50 min, compared to the sunlight.

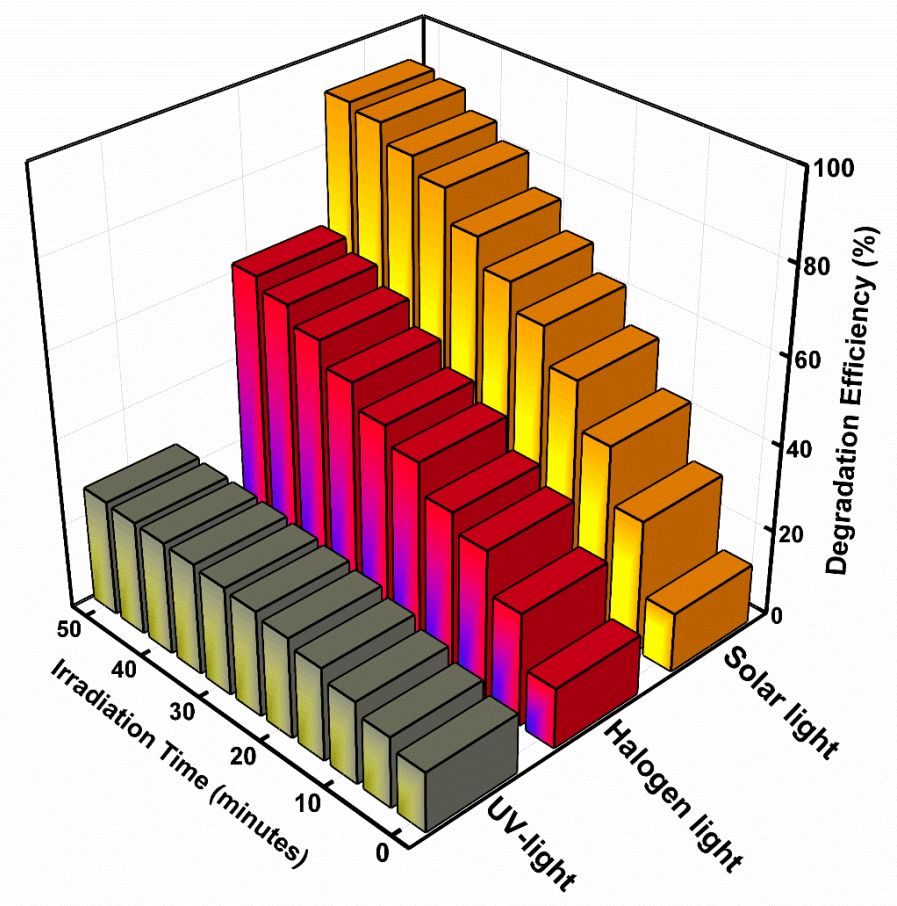

Figure 5.12. *The 3D plot of the degradation efficiency of the dye by catalyst under solar, halogen and UV irradiation.*

The degradation of the dye was observed in terms of degradation efficiency (%), as calculated by Eq. (5.9)

Degradation Efficiency (%) = $[(C_o-C)/C_o] \times 100$, (5.9)

where the C_o and C attribute the absorbance values at initial and the specified time illumination, respectively. The degradation efficiency (%) was calculated and represented in the 3-D plot, as shown in Fig. 5.12. It illustrates the comparison of degradation efficiency of the samples under solar, halogen and UV lights. The maximum 92% degradation was achieved within 50 min of solar illumination. In contrast, on the other side, under halogen and UV light, the degradation of dye was achieved upto the 68% and 27%, respectively, under the same temperature and pressure. The reaction kinetics for the degradation of the CV dye by MoS_2 NS was calculated by the pseudo-first-order kinetic model shown in Equation (5.10) [9]:

$\ln(C/C_o) = -kt$ (5.10)

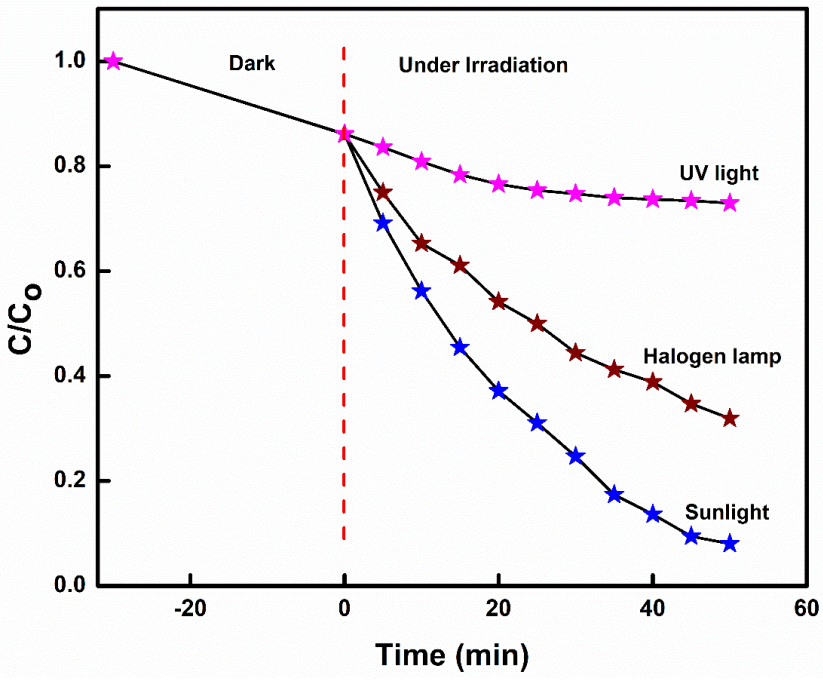

Figure 5.13. *The plot of absorbance ratio (C/C_o) of CV dye with the function of time in the presence of MoS_2.*

where C and C_0 are the time-dependent and initial concentrations, and *t* is the time at which the sample was exposed under sunlight. Fig. 5.13 attributes the plot between the ratio of concentrations (C/C_o) and the time period for the samples under solar illumination, halogen lamp, and UV light. Therefore, it showed that the fastest degradation was achieved from solar exposure to the dye sample.

The graph between the $\ln(C/C_o)$ and the irradiation time (Fig. 5.14) demonstrates the oxidation of CV dye by the MoS_2 nanosheets, which is well-fitted in a pseudo-first-order kinetic model. The rate constant was calculated to be 0.049 min^{-1} for the dye solution under the solar irradiation and proved to be the fastest degradation among the other light sources.

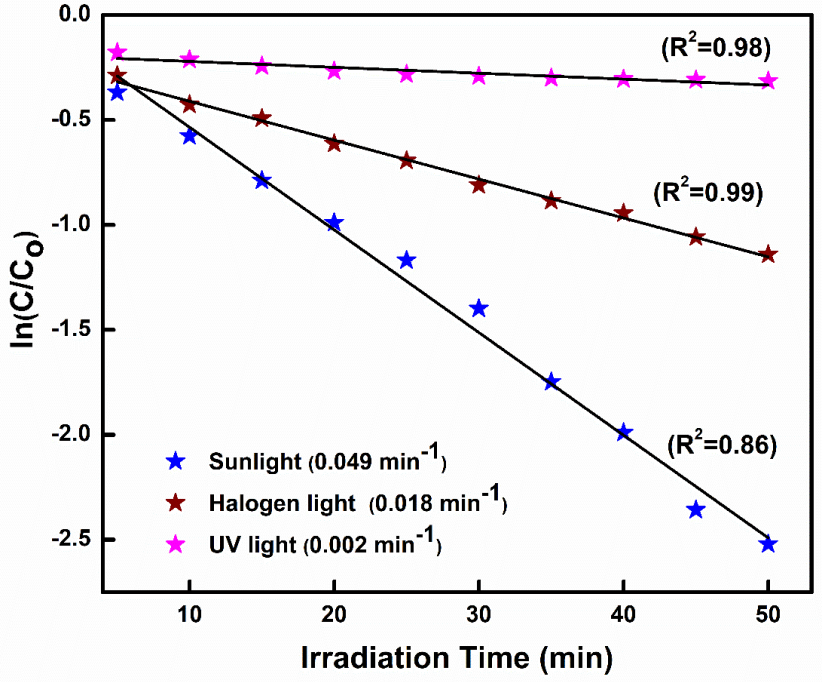

Figure 5.14. *The pseudo-first-order reaction rate constant (k) plot with a function of the irradiation time.*

The rate constant for dye degradation under halogen lamp and UV light was calculated to be 0.018 min^{-1} and 0.002 $min^{-1,}$ respectively, as shown in Fig. 5.14. The degradation of dye was also checked for different amounts of catalyst (MoS_2), varied from 0.05 g/L to 0.3 g/L. The absorption spectra were recorded for each catalyst dosage in the dye solution under no light irradiation, as shown in Fig. 5.15. The mixture was stirred for 10 min (fixed) and centrifuged afterward at 5000 rpm before recording its absorption spectra. The inset of Fig. 5.15 demonstrates the absorbance value of the dye solution with the increase in the amount of MoS_2 NSs.

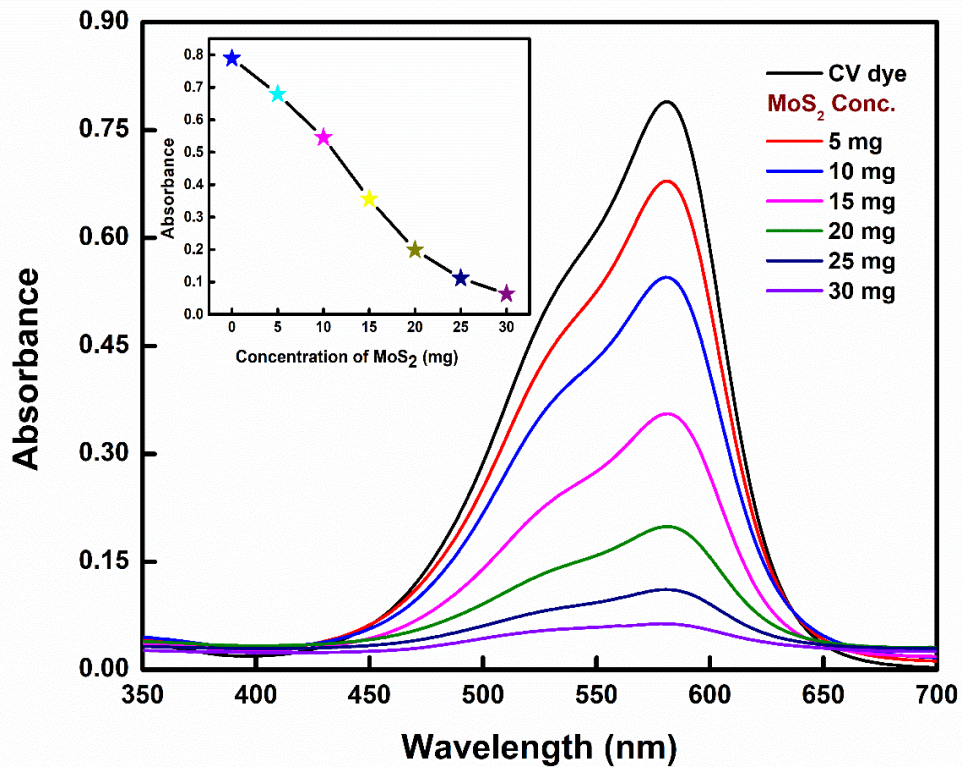

Figure 5.15. *The absorption spectra of dye for different catalyst concentrations. The inset shows the plot between the absorbance of dye vs. the catalyst concentration.*

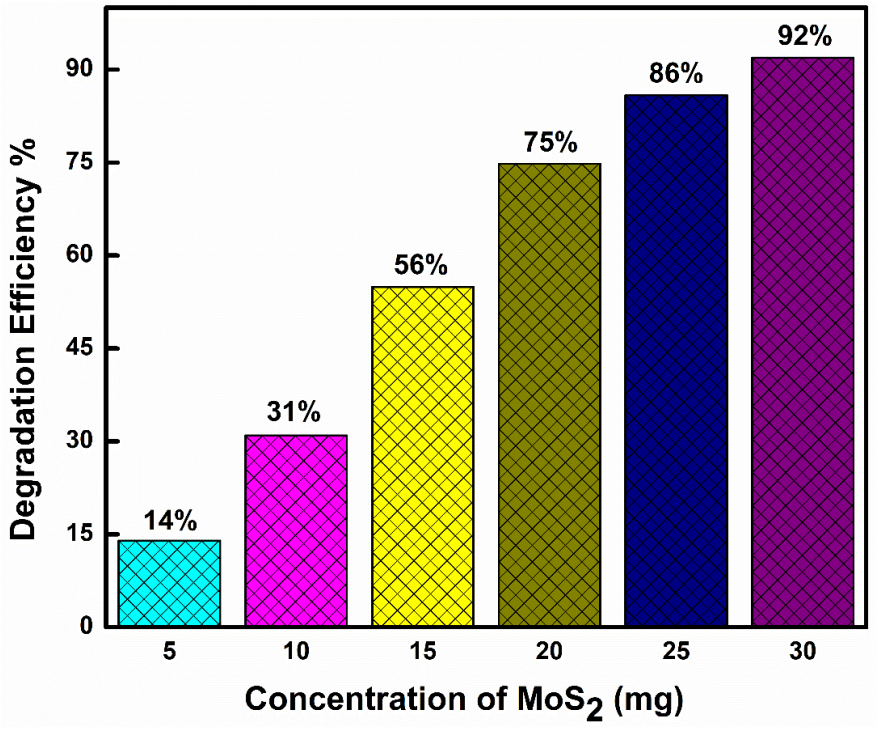

Figure 5.16. *The degradation efficiency of the CV dye with the MoS_2 NSs concentration.*

This illustrates the linear decomposition of dye due to an increase in adsorption/desorption isotherms. Fig. 5.16 showed the degradation efficiency of the catalyst at different amounts and it is noted that the dye solution was completely decomposed when 0.3 g/L catalyst was added. The comparison of the different catalysts for the degradation of the CV dye is given in Table 5.1.

Table 5.1. *The comparison of photocatalytic performance of various catalysts used to degrade 100 mL CV dye under solar irradiation.*

S. No.	Catalyst	Loading of catalyst (mg)	Conc. (μM)	Degradation (%)	Time (min)	Results
1	Sn@Cdots/ TiO_2	60	25	90	210	Ref. [34]
2	Mn/PVP/ZnO	25	24	91	180	Ref. [35]

	NPs					
3	$CaFe_2O_4$	100	94	90	100	Ref. [36]
4	ZnO flowers	100	24	86	80	Ref. [37]
5	Nano-anatase TiO_2	40	25	90	45	Ref. [38]
6	MoS_2 NSs	10	40	92	50	This work

The solar light-driven PCA of the CV dye by MoS_2 NSs was best described by the internal mechanism taking place during the process. In solar irradiation, the small bandgap energy of the MoS_2 NSs generates electron-hole pairs between conduction and valence bands. The electrons in the conduction band of the catalyst interact

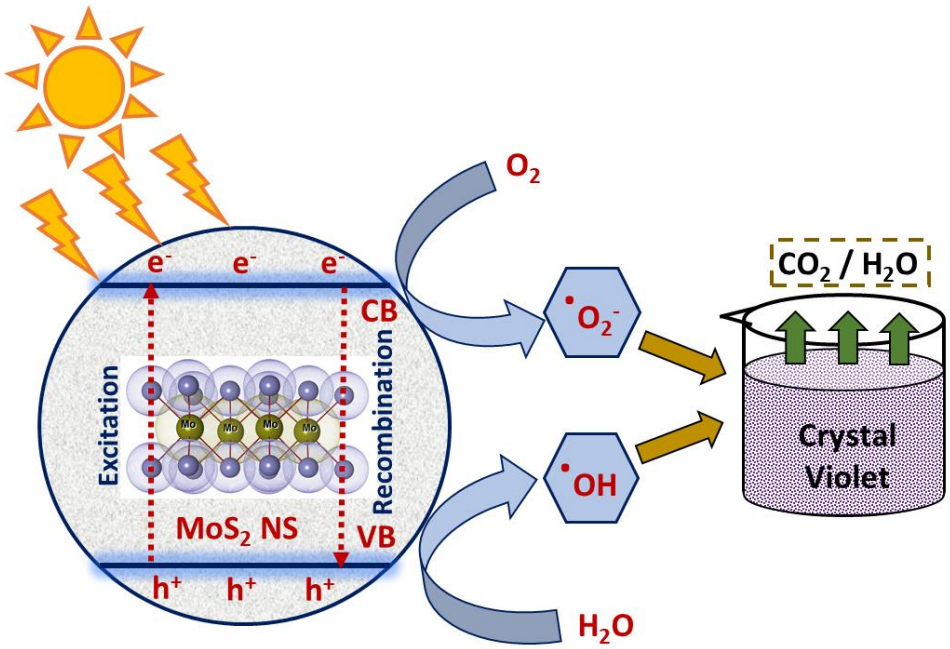

Figure 5.17. *The possible degradation mechanism of the CV dye in the presence of MoS_2 NSs under solar irradiation.*

with the oxygen atoms present in the system, which forms the superoxide ($^{\bullet}O_2^-$) radicals and afterward reacts with the H^+ ions to make H_2O_2, which lately decomposes to give hydroxyl radicals ($^{\bullet}OH$) [39]. Likewise, the holes present in the conduction band due to the formation of excitonic e-h pairs react with the water molecules present in the system to form $^{\bullet}OH$ radicals. The produced $^{\bullet}OH$ radicals interact with the dye adsorbed at the surface to release CO_2/H_2O to the environment, which is later used to produce acetic acid or used for other applications when produced at a considerable scale (illustrated in Fig. 5.17). The reaction mechanism is as follows [40].

$$MoS_2\ NS + CV \xrightarrow[10\ min]{Adsorption} \text{Dye adsorbed on } MoS_2\ NSs$$

$$MoS_2\ NSs \xrightarrow{Solar\ irradiation} MoS_2 \longrightarrow e^-\text{-}h^+ \text{ pair}$$

$$e^- + O_2 \longrightarrow {}^{\bullet}O_2^-$$

$$H_2O \longrightarrow H^+ + OH^-$$

$${}^{\bullet}O_2^- + H^+ \longrightarrow H_2O_2$$

$$H_2O_2 \longrightarrow {}^{\bullet}OH$$

$$h^+ + OH^- \longrightarrow {}^{\bullet}OH$$

$${}^{\bullet}OH + CV\ dye \longrightarrow CO_2/H_2O$$

5.6. Application of MoS_2 NSs in Li-ion Battery

The MoS_2 NSs were used as an alternative anode in the half cell with respect to the lithium metal sheet (chip) as counter electrode. The slurry for anodes were prepared by making homogeneous mixture of the active material i.e., MoS_2 NSs, carbon black as a conductive

material and PVDF (polyvinylidene difluoride) for binding in a weight ratio of 75:10:15, dissolved in NMP (N-methyl-2-pyrrolidinone) solvent tailed by the 12 h of stirring at room temperature. The slurry obtained was then coated through the doctor's blade on a copper foil. Afterward, the film was kept for drying in a vacuum oven at 75 ^{o}C for 12 h to evaporate the solvent from the film.

The circular electrodes were taken out by cutting the film into 19 mm disks. The CR2032 coin half-cells were accumulated in glove box (Abron Tech, O_2 and H_2O level were kept at ≤0.5 ppm) filled under inert atmosphere by filling it with the argon gas. The lithium disks were purchased from Sigma Aldrich (99.9%), which was employed as a reference and a counter electrode. The separator made of glass fiber filter (Advantec, GB-100R) was used whereas, 1 M $LiPF_6$ was used as an electrolyte. Then, the cyclic voltammetry (CV), rate performance and impedance spectra were measured.

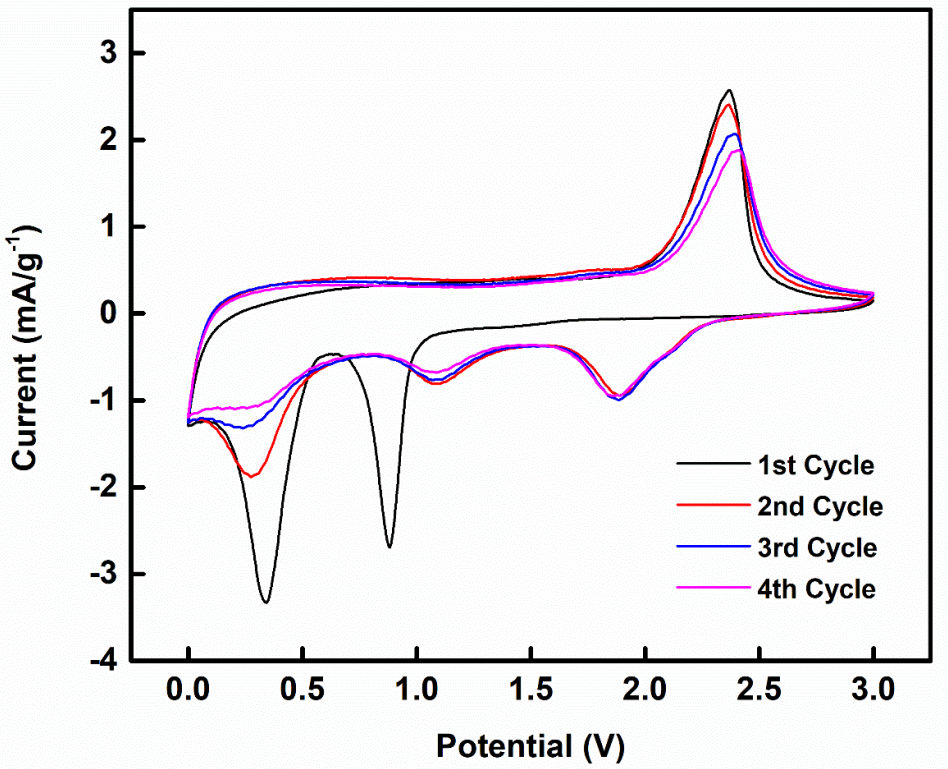

Figure 5.18. *The cyclic voltammograms of MoS_2 nanosheets at a scan rate of 0.05 mVs^{-1}.*

The cyclic voltammetry (CV) was measured for the MoS_2 electrode in the cell, as shown in Fig. (5.18). In the first cycle of CV, the two reduction peaks (at 0.33 V and 0.87 V) and one oxidation peak at 2.37 V were observed. Whereas the subsequent three cycles demonstrated the occurrence of three reduction bands at 0.28 V, 1.08 V, and 1.88 V, and one oxidation peak was observed at a voltage similar to the first cycle. Therefore, no significant variation is recorded in the potential of oxidation peak whereas, the reduction peaks were shifted from their initial positions. Here, in the first cycle, the lithiation process, i.e., intercalation of Li^+ ions with the layers of MoS_2 nanosheets, forms Li_xMoS_2 compounds. After the complete occupation of these sites, the Li^+ ions were intercalated into defect sites of MoS_2 nanosheets. Fig. (5.19) represents the stepwise rate performance of the MoS_2 nanosheets. The initial cycle shows the higher specific capacity whereas, with the increasing number of cycles, the cell performance could not stabilize much.

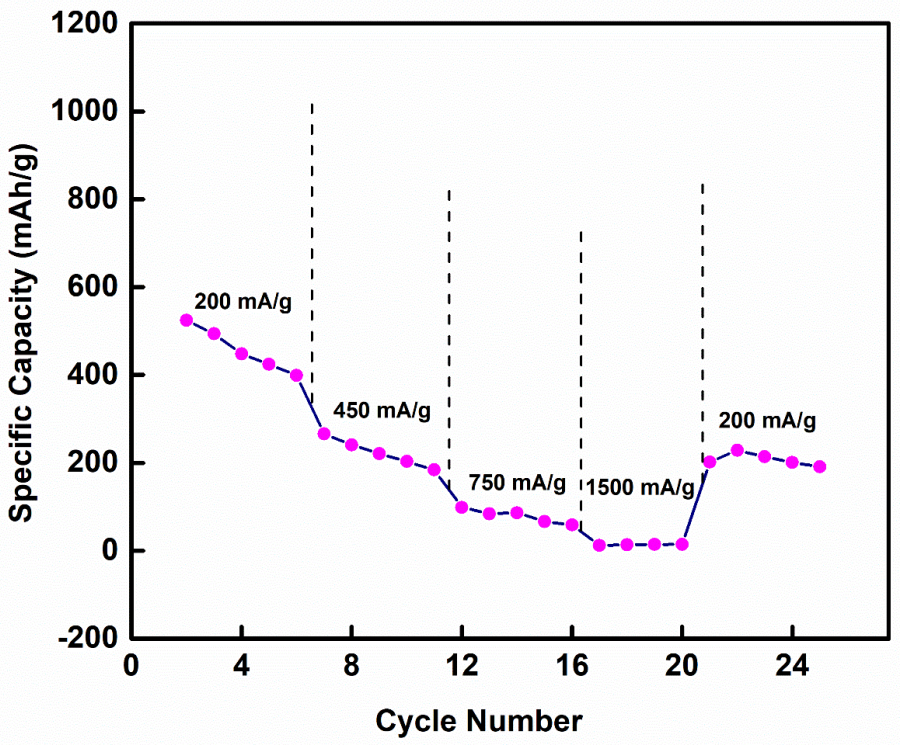

Figure 5.19. *The rate performance of MoS_2 nanosheets-based cell for number of cycles.*

Electrochemical impedance spectroscopy (EIS) was employed to the fresh cell and the impedance spectra of the prepared MoS_2 nanosheets were measured and are demonstrated in Fig. (5.20). The impedance spectra were recorded for MoS_2 nanosheets as an anode material within the range of 10 mHz to 10 kHz for an AC voltage of 5 mV. The semicircle in the curve falls in the region of high-frequency whereas, the straight line falls in the region of low-frequency. The ohmic resistance (R_s) was measured by the interception of the x-axis in the region of high-frequency, which shows the electrode and electrolyte resistance. In the middle-frequency range, the EIS test demonstrates the charge transfer resistance (R_{ct}). The inclination of the curve in the region of low-frequency by 45^o shows the Warburg impedance (Z_w), which defines the resistance due to Li-ion diffusion in the electrolyte solution. The diffusion coefficient (D) could be calculated through the equation (5.11):

$$D = \frac{0.5R^2T^2}{A^2C^2F^4\sigma^2} \quad (5.11)$$

Where R is the gas constant, A is electrode area, T is the absolute temperature, F is the Faraday constant, C is the Li^+ ion concentration and σ is the Warburg factor. Also, the real impedance can be explained by equation (5.12):

$$Z' = R_s + R_{ct} + \sigma\omega^{-0.5} \quad (5.12)$$

The plot slope obtained between the Z' vs. $\omega^{(-0.5)}$ gives the Warburg factor. The D calculated for the above EIS test came out to be 2.83×10^{-12} cm^2s^{-1}. This indicates that the prepared nanosheets deliver higher discharge capacity.

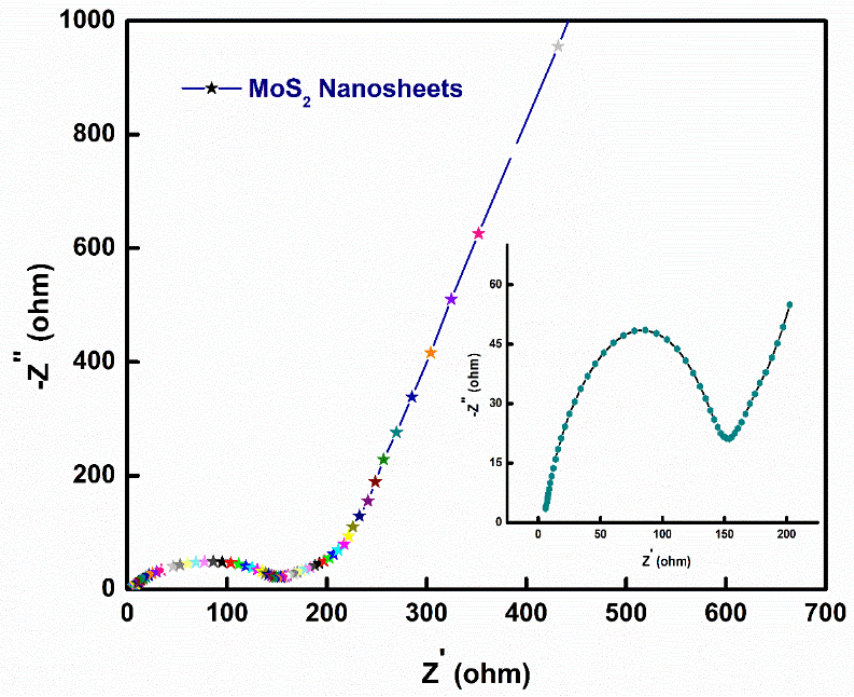

Figure 5.20. *The impedance spectra of prepared MoS_2 nanosheets recorded with AC pulse of 5 mV.*

5.7. Conclusions

MoS_2 NSs were synthesized by the facile hydrothermal technique and studied for their structural, morphological, compositional, electrochemical and optical properties. The XRD pattern confirms the formation of 2H structure of MoS_2 NSs with a crystallite size of 33 nm. The SEM images illustrate the formation of MoS_2 flakes-like structure. The HR-TEM images showed the synthesized MoS_2 nanosheets have 5-6 layers, and the distance between the layers was 0.67 nm. The orderly arranged fringes in the HR-TEM image confirmed the crystalline structure with the inter-planar spacing of 0.54 nm, which is approximately similar to the value calculated from the XRD pattern. The NSs exhibit well-defined absorption bands with a bandgap energy of 2.07 eV.

The synthesized MoS_2 nanosheets were used for the decomposition of the crystal violet dye as a catalyst. The chain of experiments demonstrated that the 0.1 g/L of the catalyst worked perfectly for the degradation of 4×10^{-5} M of the CV dye under solar irradiation within 50 min. The degradation efficiency and the kinetic rate constant for the above trials were 92% and 0.04 min^{-1}, respectively. Under halogen light, these values are 68% and 0.018 min^{-1}, respectively. Further, complete degradation of the dye can be achieved without irradiation by increasing the concentration of the catalyst (MoS_2 NSs) from 0.05g/L to 0.3g/L. The MoS_2 nanosheets as an anode in Li-ion battery showed a significant performance with the diffusion constant of 2.83 cm^2s^{-1}.

References

[1] Ritika, M. Kaur, A. Umar, S. Mehta, S. Singh, S. Kansal, H. Fouad, O. Alothman, Rapid solar-light driven superior photocatalytic degradation of methylene blue using MoS_2-ZnO heterostructure nanorods photocatalyst, materials (basel). 11 (2018) 2254.

[2] W. Guan, S. Tian, The modified chitosan for dyeing wastewater treatment via adsorption and flocculation, Sci. Adv. Mater. 9 (2017) 1603–1609.

[3] M. Namdeo, Magnetite Nanoparticles as effective adsorbent for water purification-a review, Namdeo, Adv. Recycling Waste Manag. 2 (2017) 1000135.

[4] A. Kaur, A. Umar, W.A. Anderson, S.K. Kansal, Facile synthesis of CdS/TiO_2 nanocomposite and their catalytic activity for ofloxacin degradation under visible illumination, J. Photochem. Photobiol. A Chem. 360 (2018) 34–43.

[5] P. Sharma, M.S. Mehata, Rapid sensing of lead metal ions in an aqueous medium by MoS_2 quantum dots fluorescence turn-off, Mater. Res. Bull. 131 (2020) 110978.

[6] V. Sharma, M.S. Mehata, Synthesis of photoactivated highly fluorescent Mn^{2+}-doped ZnSe quantum dots as effective lead sensor in drinking water, Mater. Res. Bull. 134 (2021) 111121.

[7] P. Sharma, M.S. Mehata, Colloidal MoS_2 quantum dots based optical sensor for detection of 2,4,6-TNP explosive in an aqueous medium, Opt. Mater. 100 (2020) 109646.

[8] M.K. Singh, M.S. Mehata, Enhanced photoinduced catalytic activity of transition metal ions incorporated TiO_2 nanoparticles for degradation of organic dye: Absorption and photoluminescence spectroscopy, Opt. Mater. 109 (2020) 110309.

[9] M.K. Singh, M.S. Mehata, Phase-dependent optical and photocatalytic performance of synthesized titanium dioxide (TiO_2) nanoparticles, Optik. 193 (2019) 163011.

[10] S. Bishnoi, B. Rajesh, G. Swati, V. Vikesh Jaiswal, M. Sahu, P. Singh, D. Haranath, Structural, morphological, photoluminescence and electrical characterization of aluminium doped ZnO phosphors for solar cell applications, Mater. Today Proc., Elsevier Ltd, 5 (2018) 610–619.

[11] L. Chen, Y. Feng, X. Zhou, Q. Zhang, W. Nie, W. Wang, Y. Zhang, C. He, One-Pot Synthesis of MoS_2 nanoflakes with desirable degradability for photothermal cancer therapy, ACS Appl. Mater. Interfaces. 9 (2017) 17347–17358.

[12] B.L. Li, M.I. Setyawati, L. Chen, J. Xie, K. Ariga, C.T. Lim, S. Garaj, D.T. Leong, Directing assembly and disassembly of 2D MoS_2 nanosheets with DNA for drug delivery, ACS Appl. Mater. Interfaces. 9 (2017) 15286–15296.

[13] X. Zong, H. Yan, G. Wu, G. Ma, F. Wen, L. Wang, C. Li, Enhancement of photocatalytic H_2 evolution on CdS by loading MoS_2 as cocatalyst under visible light irradiation, J. Am. Chem. Soc. 130 (2008) 7176–7177.

[14] J. Kibsgaard, Z. Chen, B.N. Reinecke, T.F. Jaramillo, Engineering the surface structure of MoS_2 to preferentially expose active edge sites for electrocatalysis, Nat. Mater. 11

(2012) 963–969.
[15] D. Voiry, M. Salehi, R. Silva, T. Fujita, M. Chen, T. Asefa, V.B. Shenoy, G. Eda, M. Chhowalla, Conducting MoS_2 nanosheets as catalysts for hydrogen evolution reaction, Nano Lett. 13 (2013) 6222–6227.
[16] J. Yu, X. Ma, W. Yin, Z. Gu, Synthesis of PVP-functionalized ultra-small MoS_2 nanoparticles with intrinsic peroxidase-like activity for H_2O_2 and glucose detection, RSC Adv. 6 (2016) 81174–81181.
[17] X. Yang, J. Li, T. Liang, C. Ma, Y. Zhang, H. Chen, N. Hanagata, H. Su, M. Xu, Antibacterial activity of two-dimensional MoS_2 sheets, Nanoscale. 6 (2014) 10126–10133.
[18] C. Ataca, S. Ciraci, Dissociation of H_2O at the vacancies of single-layer MoS_2, Phys. Rev. B. 85 (2012) 195410.
[19] M. Park, Y.J. Park, X. Chen, Y.-K. Park, M.-S. Kim, J.-H. Ahn, MoS_2 -based tactile sensor for electronic skin applications, Adv. Mater. 28 (2016) 2556–2562.
[20] M.A. Bissett, I.A. Kinloch, R.A.W. Dryfe, Characterization of MoS_2-graphene composites for high-performance coin cell supercapacitors, ACS Appl. Mater. Interfaces. 7 (2015) 17388–17398.
[21] Y. Teng, H. Zhao, Z. Zhang, Z. Li, Q. Xia, Y. Zhang, L. Zhao, X. Du, Z. Du, P. Lv, K. Świerczek, MoS_2 nanosheets vertically grown on graphene sheets for lithium-ion battery anodes, ACS Nano. 10 (2016) 8526–8535.
[22] L. David, R. Bhandavat, G. Singh, MoS_2/graphene composite paper for sodium-ion battery electrodes, ACS Nano. 8 (2014) 1759–1770.
[23] Y. Yoon, K. Ganapathi, S. Salahuddin, How good can monolayer MoS_2 transistors be?, Nano Lett. 11 (2011) 3768–3773.
[24] Y. Chen, X. Wang, P. Wang, H. Huang, G. Wu, B. Tian, Z. Hong, Y. Wang, S. Sun, H. Shen, J. Wang, W. Hu, J. Sun, X. Meng, J. Chu, Optoelectronic properties of few-layer MoS_2 fet gated by ferroelectric relaxor polymer, ACS Appl. Mater. Interfaces. 8 (2016) 32083–32088.
[25] H. Xie, B. Jiang, B. Liu, Q. Wang, J. Xu, F. Pan, An investigation on the tribological performances of the SiO_2/MoS_2 hybrid nanofluids for magnesium alloy-steel contacts, Nanoscale Res. Lett. 11 (2016) 329.
[26] L. Ye, D. Wang, S. Chen, Fabrication and enhanced photoelectrochemical performance of MoS_2/S-doped g-C_3N_4 heterojunction film, ACS Appl. Mater. Interfaces. 8 (2016) 5280–5289.
[27] D. Chiappe, E. Scalise, E. Cinquanta, C. Grazianetti, B. Van Den Broek, M. Fanciulli, M. Houssa, A. Molle, Two-dimensional Si nanosheets with local hexagonal structure on a MoS_2 surface, Adv. Mater. 26 (2014) 2096–2101.
[28] K.S. Novoselov, D. Jiang, F. Schedin, T.J. Booth, V. V. Khotkevich, S. V. Morozov, A.K. Geim, Two-dimensional atomic crystals, Proc. Natl. Acad. Sci. U. S. A. 102 (2005) 10451–10453.

[29] A. Splendiani, L. Sun, Y. Zhang, T. Li, J. Kim, C.Y. Chim, G. Galli, F. Wang, Emerging photoluminescence in monolayer MoS_2, Nano Lett. 10 (2010) 1271–1275.

[30] T. Li, G. Galli, Electronic properties of MoS_2 nanoparticles, J. Phys. Chem. C. 111 (2007) 16192–16196.

[31] G. Nagaraju, C.N. Tharamani, G.T. Chandrappa, J. Livage, Hydrothermal synthesis of amorphous MoS_2 nanofiber bundles via acidification of ammonium heptamolybdate tetrahydrate, Nanoscale Res. Lett. 2 (2007) 461–468.

[32] M.A.R. Anjum, H.Y. Jeong, M.H. Lee, H.S. Shin, J.S. Lee, Efficient hydrogen evolution reaction catalysis in alkaline media by all-in-one MoS_2 with multifunctional active sites, Adv. Mater. 30 (2018) 1707105.

[33] S. Su, W. Cao, W. Liu, Z. Lu, D. Zhu, J. Chao, L. Weng, L. Wang, C. Fan, L. Wang, Dual-mode electrochemical analysis of microRNA-21 using gold nanoparticle decorated
MoS_2 nanosheet, Biosens. Bioelectron. 94 (2017) 552–559.

[34] V.B. Kumar, N. Perkas, Z. Porat, A. Gedanken, Solar-light-driven photocatalytic activity of novel Sn@C-Dots-modified TiO_2 catalyst, ChemistrySelect. 2 (2017) 6683–6688.

[35] M. Mittal, M. Sharma, O.P. Pandey, Photocatalytic studies of crystal violet dye using Mn doped and PVP capped ZnO nanoparticles, J. Nanosci. Nanotechnol. 14 (2014) 2725–2733.

[36] W. Shi, Q. Li, S. An, T. Zhang, L. Zhang, Magnetic nanosized calcium ferrite particles for efficient degradation of crystal violet using a microwave-induced catalytic method: insight into the degradation pathway, J. Chem. Technol. Biotechnol. 91 (2016) 367–374.

[37] S. Ameen, M.S. Akhtar, M. Nazim, H.S. Shin, Rapid photocatalytic degradation of crystal violet dye over ZnO flower nanomaterials, Mater. Lett. 96 (2013) 228–232.

[38] S. Samira, A. Raja P, Photocatalytic degradation of crystal violet (C.I. basic violet 3) on nano TiO_2 containing anatase and rutile phases (3:1), J. Thermodyn. Catal. 03 (2012) 117-119.

[39] Y. Cao, Q. Li, W. Wang, Construction of a crossed-layer-structure MoS_2/g-C_3N_4 heterojunction with enhanced photocatalytic performance, RSC Adv. 7 (2017) 6131–6139.

[40] H.K. Sadhanala, S. Senapati, K.V. Harika, K.K. Nanda, A. Gedanken, Green synthesis of MoS_2 nanoflowers for efficient degradation of methylene blue and crystal violet dyes under natural sun light conditions, New J. Chem. 42 (2018) 14318–14324.

CHAPTER 6

2,4,6-TNP explosive sensing by WS_2 QDs

6.1. Introduction

The two-dimensional (2D) nanomaterials have always been fascinated the research community due to their extraordinary properties. The most extensively studied 2D material is graphene, possessing unique properties that could be exploited in many ways to sort various purposes for greater advancements in science and technology [1,2]. In the past few decades, the search for other 2D materials led the scientific community to a different class of transition metal dichalcogenides (TMDs) with a graphene-like structure and many other interesting properties [3–7]. One such TMD is the tungsten disulfide (WS_2), which has gained considerable attention due to its excellent optical and electronic properties [8]. The 2D structure of WS_2 is composed of the atomic layer of tungsten sandwiched between the two hexagonal layers of the sulfur atoms. The layers are interconnected by the weak van der Waals forces [9]. The reduction in layers causes the transition from the indirect bandgap to the direct bandgap by exfoliating the bulk WS_2 to its nanosheets [10,11]. This enlargement in the bandgap encouraged some outstanding properties, which makes it appropriate for applications in bioimaging [12], catalysis [13], energy storage devices [14,15], transistors [16] and optoelectronic devices [17].

Recently, a new class of nanomaterials known as the WS_2 quantum dots (QDs) has been developed by restricting the size of the nanosheets. It possesses distinct electrical and optical properties than nanosheets because of quantum effects, such as quantum confinement and edge effects [18–24]. This displays the large direct bandgap energy (3.2 eV) of the WS_2 QDs when compared to its monolayer (2.1 eV) and a bright blue emission is observed when

exposed to the ultraviolet (UV) light [25]. Photoluminescence (PL) properties of WS_2 QDs can be exploited for many-valued causes like electrodeless sensing studies, catalysis applications, electrical transportation, targeted drug delivery, etc. [26,27]. The PL-based sensing of WS_2 QDs was extensively studied and a lot of work has been pursued. WS2 QDs carried out the selective sensing of dopamine through its fluorescence turn-off mechanism [28]. The fungicide drug called nitrofurazone was detected by the quenching mechanism of the fluorescent WS_2 QDs through the Förster resonance energy transfer (FRET) mechanism [29].

The quantum dots have been preferred for the direct detection of toxic and dangerous compounds. One such compound is 2,4,6-trinitrophenol (TNP), popular as picric acid, which is an explosive compound with more explosive strength than the very famous explosive 2,4,6-trinitrotoluene (TNT) [30–35]. TNP is used deliberately in fireworks, dye, pharmaceuticals, rocket fuels, forensic research, and chemical laboratories [36]. The widely used compound finds its way into the ground and pollutes the soil and the water bodies by its highly acidic nature. TNP has many proven harmful effects on the aquatic ecosystem, the terrestrial lifeforms and can cause many health issues like damaging the respiratory system, affecting liver functioning, skin irritations, etc., in humans [37]. The high solubility and highly acidic nature make its detection significant and appealing.

Here in this work, the novel water-dispersible WS_2 QDs has been synthesized by facile hydrothermal technique. The synthesized QDs were employed to detect TNP in an aqueous medium by the quenching of PL intensity. The prepared QDs showed promising sensitivity and selectivity towards the highly acidic nitro explosive, which has a high-risk factor in humans and the environment. The Förster resonance energy transfer mechanism has also been

explained in this work. The primary detection of 2,4,6-TNP compound in water through WS_2 QDs holds great significance for the safety of human beings and the environment.

6.2. Materials and methods

6.2.1. Materials used

All the reagents used were of analytical (AR) grade and without further purification. The sodium tungstate was used as a tungsten source, purchased from CDH chemicals LTD. The sodium sulfide had been used as sulfur source, purchased from CDH chemicals LTD. The diaminobutane (DAB) is used as the capping agent, purchased from Sigma Aldrich. The nitro-explosive compounds, i.e., 2,4,6-trinitrophenol, 2,4-nitrotoluene, 2-nitrotoluene, 4-nitrotoluene and 2,4-dinitrobenzene were purchased from Sigma Aldrich. The ultrapure de-ionized (DI) water was used for the sample preparation and sensing application.

6.2.2. Experimental method

The WS_2 QDs were prepared through a novel facile hydrothermal method. Here, the 0.5 mM sodium tungstate and a certain amount of DAB are mixed in 30 ml of DI water in a round bottom flask under an inert environment. The 1.2 mM sodium sulfide was stirred separately to 20 ml DI water for 30 minutes and then transferred to the mixture above in a round bottom flask. After 10 min of rigorous stirring, the combination was moved to the stainless-steel hydrothermal chamber with Teflon lined vessel and kept in a pre-heated oven at 150 ºC for 8 h. The retrieved surfactant was dialyzed by a cellulose membrane of 1kda for 48 h, where water is changed every 2 h. The finally recovered colloidal solution consists of the fluorescent WS_2 QDs.

6.3. Instrumentation

The absorption spectra were recorded by the UV-visible double beam spectrophotometer (Lambda 750, Perkin Elmer). The photoluminescence (PL) spectra were recorded by the spectrofluorometer (Flourolog-3, Horiba Jobin Yvon Inc.) with an excitation source of a 450 W xenon lamp [38]. The sample cuvette made of quartz was used to record the steady-state measurements.

6.4. Results and Discussion

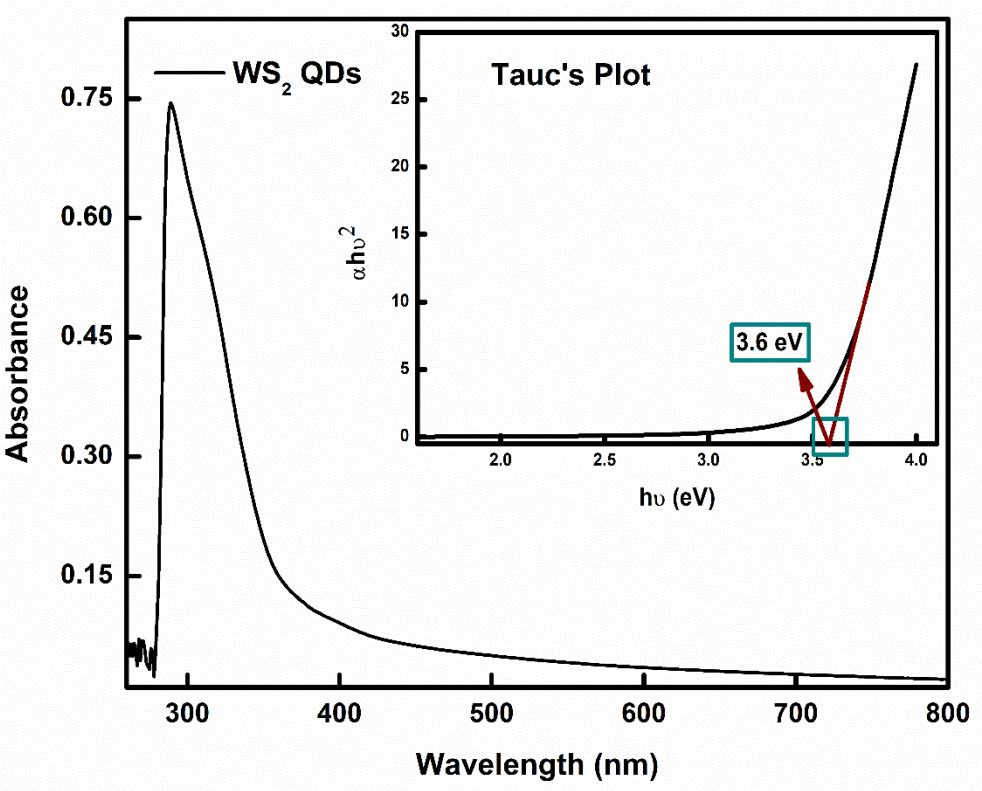

Figure 6.1. *The absorption spectrum of the WS_2 QDs. Inset illustrates the Tauc's plot for the measurement of the direct bandgap.*

UV-visible absorption spectroscopy is a very important diagnostic technique to record electronic transitions of the WS_2 QDs. Figure (6.1) demonstrates the absorption spectrum of the WS_2 QDs and a sharp band has been observed at a wavelength of 288 nm, illustrating the

excitonic behavior of the QDs. The inset of Fig. (6.1), represents the Tauc's plot of as-synthesized WS_2 QDs, to depict the optical bandgap energy (E_g) through the well-known Tauc′s equation (6.1):

$$\boldsymbol{\alpha h\nu = A(h\nu - E_g)^n} \qquad \textbf{(6.1)}$$

where *A* signifies the constant value known as band tailing parameter, α illustrates the absorption constant, *n* is the power factor of the transition mode and $h\nu$ describes the photon energy. The factor *n* varies for different electronic transitions and for the direct transitions, it is equal to ½.

For determining E_g, the Tauc′s plot was drawn between $(\alpha h\nu)^2$ vs. $h\nu$. The intercept of the x-axis ($h\nu$) by extrapolating the linear part of the Tauc′s plot provides the energy bandgap of WS_2 QDs. The optical bandgap for a direct transition of the prepared QDs was obtained to be ~3.6 eV, which is comparably larger than its bulk counterparts because of the quantum confinement effect.

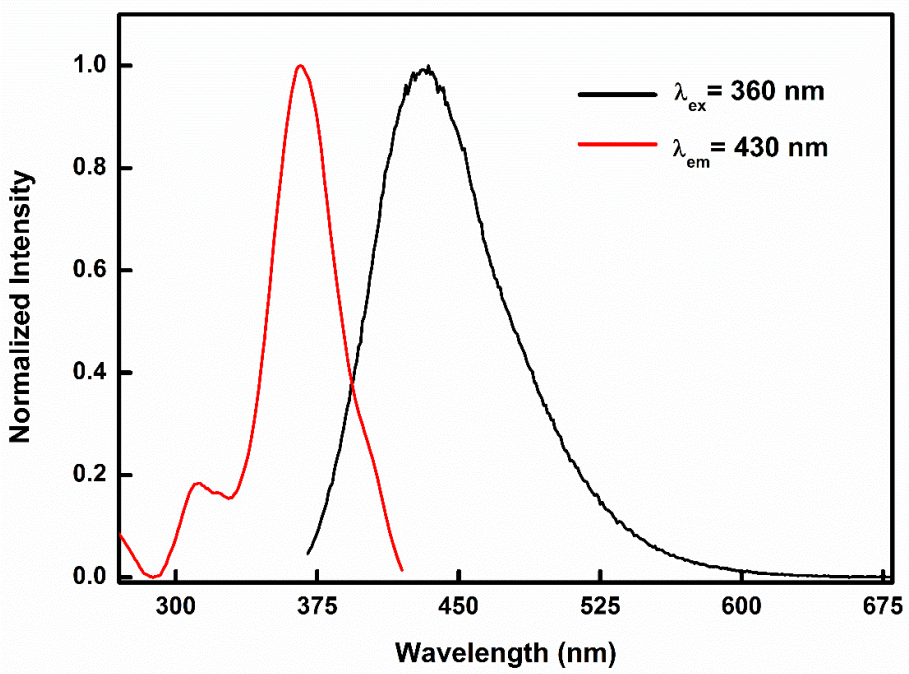

Figure 6.2. *Normalized PL and PL-excitation spectra of WS_2 QDs in water.*

Figure (6.2), illustrates the PL spectrum of the prepared WS_2 QDs, which shows a band at 432 nm when excited with the source wavelength of 360 nm. The PL-excitation spectrum shows peaks at 310 and 360 nm with an emission wavelength of 430 nm.

The absorption and excitation of the QDs do not overlay completely, which may occur due to the PL of WS_2 QDs, which comprises different species that may originate from various ground states. Accordingly, the PL of the QDs were measured at various excitation wavelengths ranging from 300 to 400 nm with an interval of 10 nm, as shown in Fig. (6.3). With the increase in the excitation wavelengths, the PL peak position shift towards the higher wavelengths region (from 420 to 460 nm), along with the change in peak intensity (Fig. (6.4)).

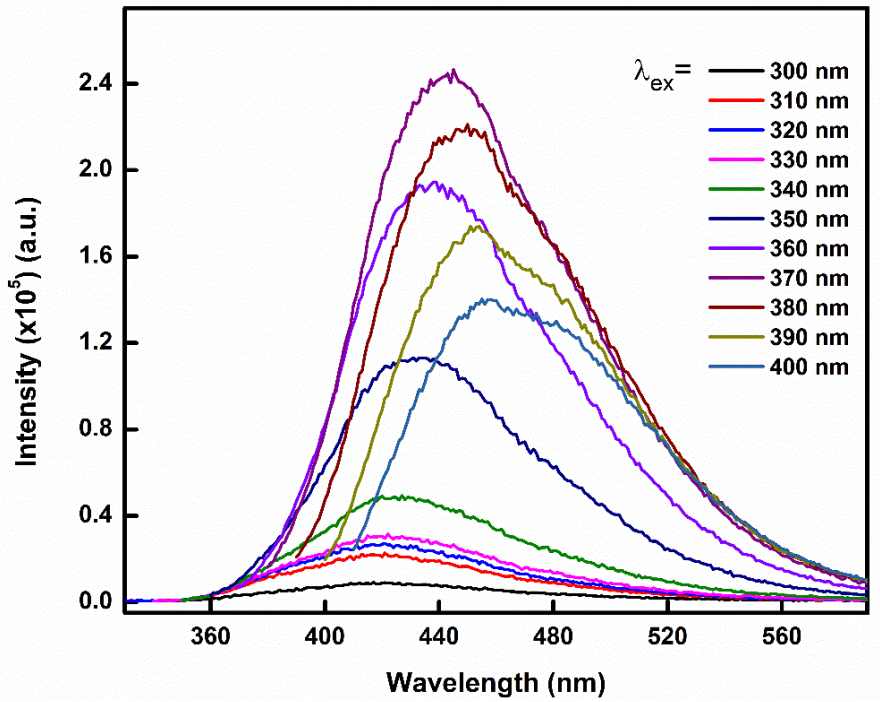

Figure 6.3. *The PL spectra of MoS_2 QDs in the water at different excitation wavelengths.*

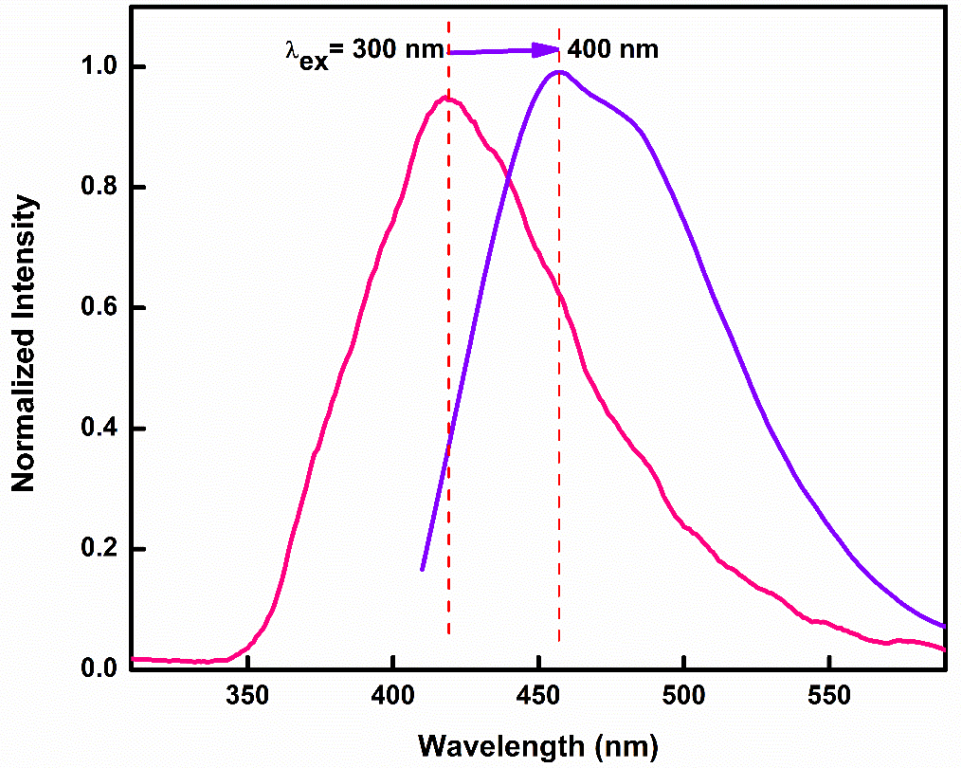

Figure 6.4. *Peak normalized PL spectra of WS_2 QDs dispersed in water with varying the excitation wavelength from 300 to 400 nm.*

These changes may have occurred due to the formation of electron-hole pairs at different energy levels, which took place due to the inhomogeneous distribution of the particle size in the aqueous medium and the surface functionalization of the WS_2 QDs. The corresponding blue shift occurred in the PL excitation spectrum with changing emission wavelength, as shown in Fig. (6.5).

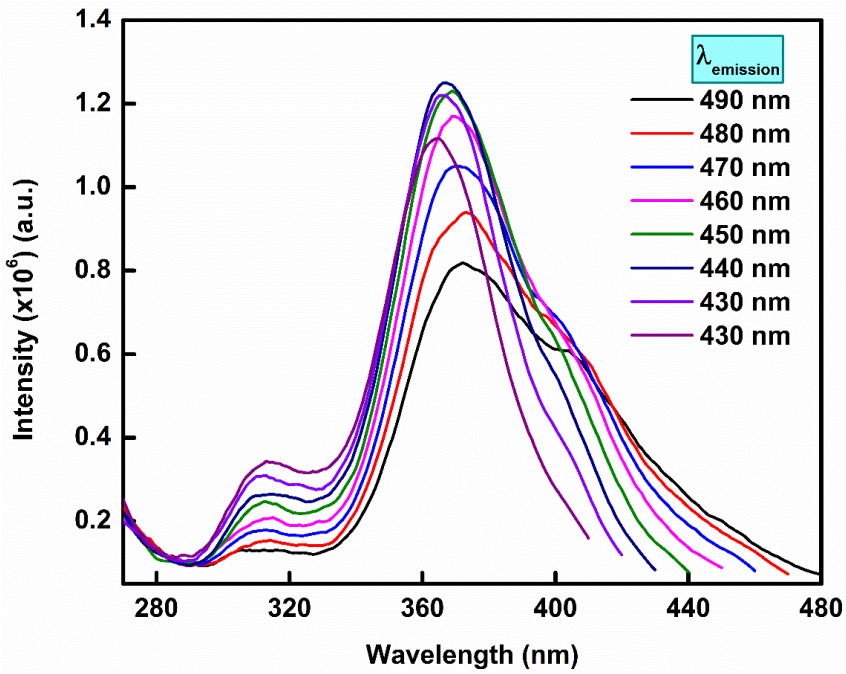

Figure 6.5. *PL-excitation spectra at different PL wavelengths of MoS_2 QDs dispersed in water.*

6.5. Detection of Nitro explosives

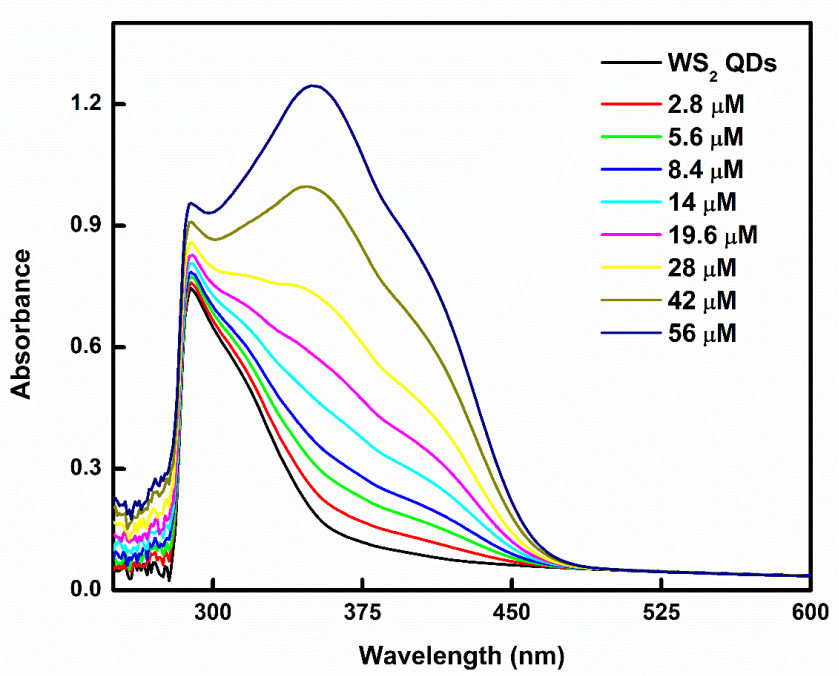

Figure 6.6. *The absorption spectra of WS_2 QDs with different concentrations of TNP in water.*

Figure (6.6) demonstrates the change in the absorption spectrum of the prepared WS_2 QDs with an increase in the concentration of TNP. The addition of TNP (2.8 µM) increased the absorbance of the QDs, accompanied by the origination of a new absorption band at around 350 nm from TNP. Upon increasing the concentration of TNP from 2.8 to 56 µM, the absorbance of the WS_2 QDs increases from 0.74 to 0.95. Fig. (6.7) shows the linear relationship between the absorbance of WS_2 QDs and the concentration of TNP. The observed linear relationship exhibits that WS_2 QDs can be employed as a sensing probe to detect TNP in water.

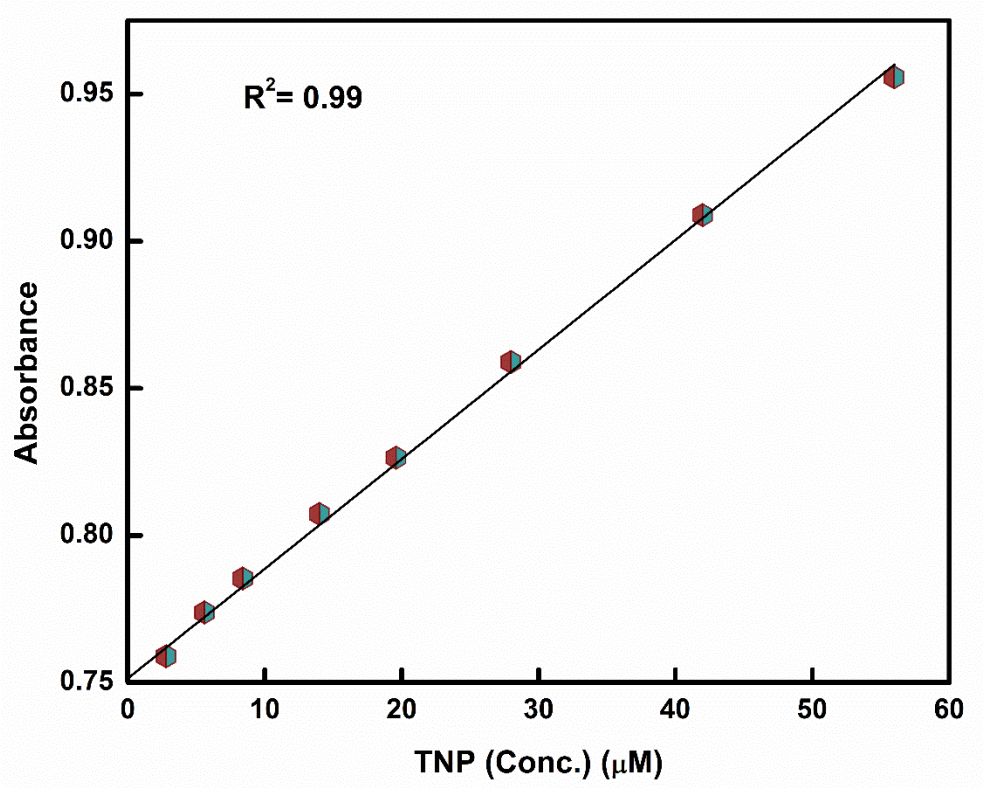

Figure 6.7. *A plot between the absorbance of the WS_2 QDs and the concentration of TNP.*

WS_2 QDs have been preferred as a fluorescent probe for detecting nitro compounds due to their size-dependent bandgap tuning. Therefore, the PL titration experiments of the WS_2 QDs were conducted for various nitro compounds (10^{-3} M) to observed their impact on PL spectrum and intensity. The experiment was withheld by taking QDs (3.5 ml) in a 10 mm wide

quartz cuvette as a fluorescent probe. Afterward, different concentrations of the nitro explosive compounds were added in an incremental order from 0.28 µM to 160 µM. The PL spectra were recorded at each concentration for different nitro explosive compounds at the exciting wavelength of 360 nm.

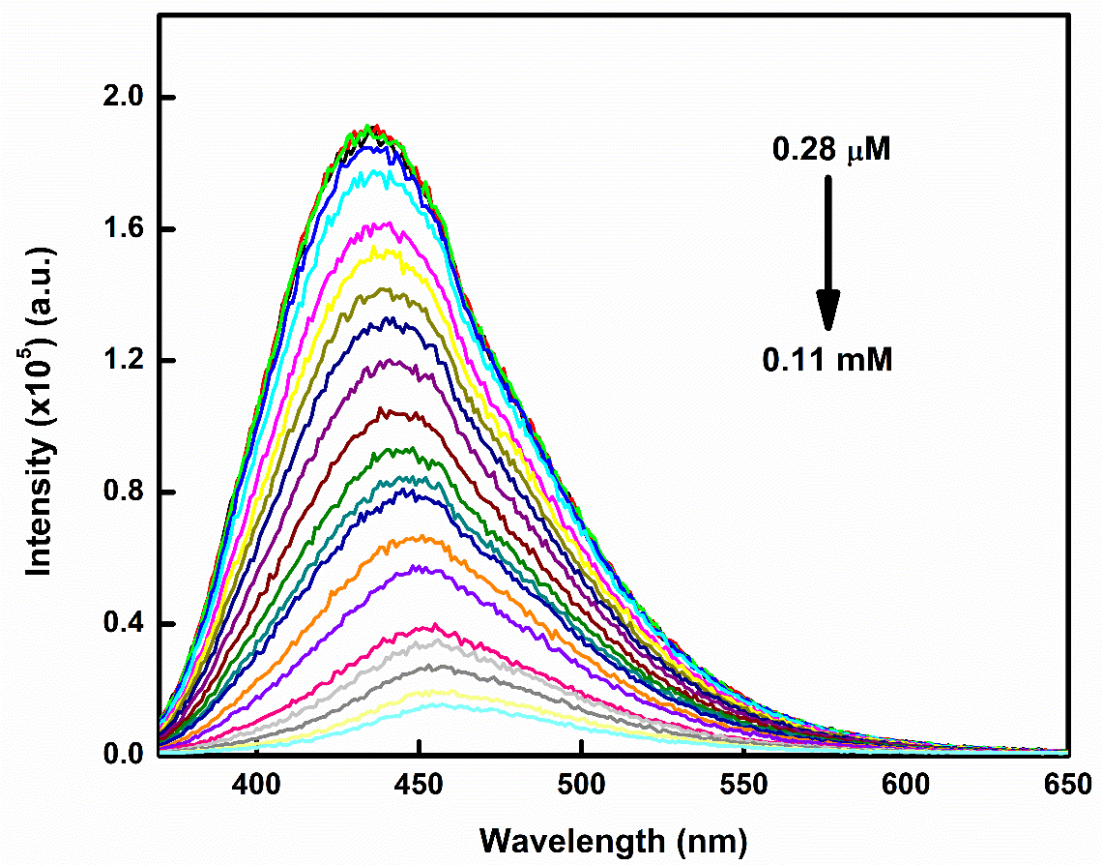

Figure 6.8. *The PL spectra of WS_2 QDs with the incremental concentration of TNP in water with 360 nm excitation of wavelength.*

The PL intensity recorded at excitation wavelength 360 nm of the WS_2 QDs were gradually quenched with increasing concentration of the TNP compound, as shown in Fig. (6.8). Fig. (6.8) shows that the very small concentration of TNP (1.4 µM) caused significant quenching in the PL intensity of the WS_2 QDs. The initial PL intensity of the QDs reduced to

half by adding 17 µM concentration of TNP. The initial PL intensity of the QDs quenches to ~99% by raising the concentration of TNP to 1.6 mM. Also, the blue fluorescent WS_2 QDs turn non-fluorescent under UV illumination.

The substantial decrease in the PL intensity of the WS_2 QDs were signified using the well-known Stern-Volmer (S-V) equation (6.2):

$$I_0/I = K_{S\text{-}V}\,[\text{TNP}] + 1, \qquad (6.2)$$

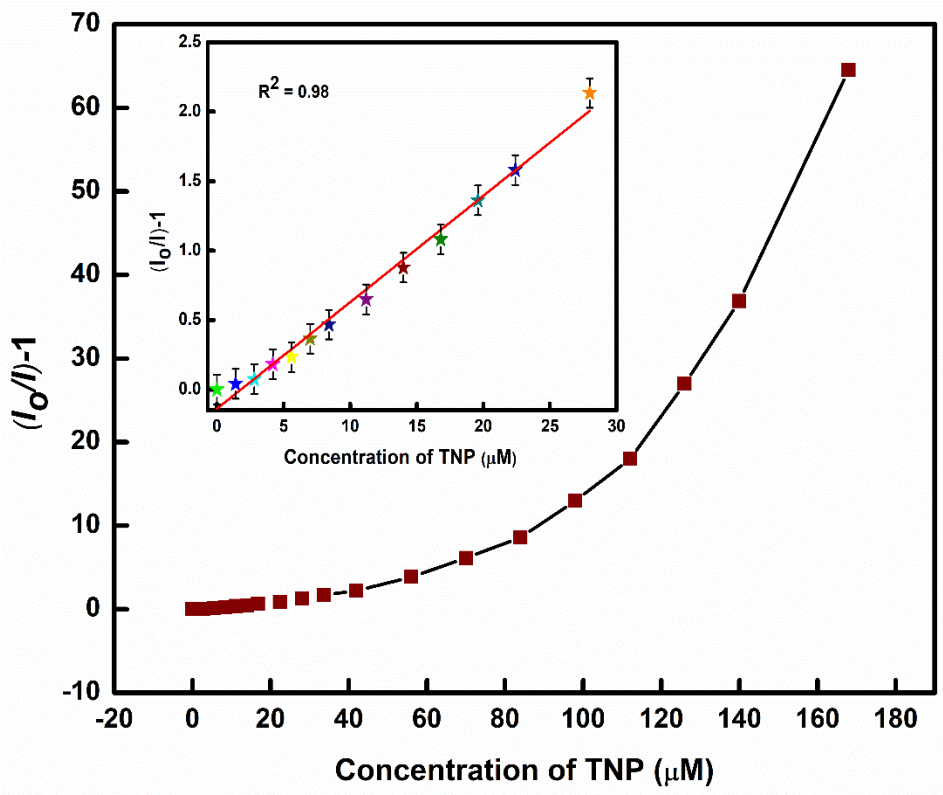

Figure 6.9. *The SV plot between relative PL intensity of QDs vs. the TNP concentration. The inset of the figure shows the linear region of SV plot at low concentrations of TNP.*

where I_0 and I denote the initial and positional (with different concentrations of TNP) PL intensities of the WS_2 QDs, respectively [TNP] and $K_{S\text{-}V}$ denotes the quenching constant (M^{-1}). Fig. (6.9) illustrates the non-linear SV plot for higher concentrations of TNP, whereas a

linear SV plot has been obtained for the lower concentrations of TNP (inset of Fig. 6.9). The quenching constant ($K_{S\text{-}V}$) was calculated to be 0.76×10^5 M^{-1}. The limit of detection (LOD) calculated for the above titration using $3\sigma/K_{S\text{-}V}$, where σ illustrates the standard deviation of the blank and $K_{S\text{-}V}$ is the slope of the SV plot to be 0.2 µM, for the dynamic range of TNP concentration from 0.28 to 85 µM.

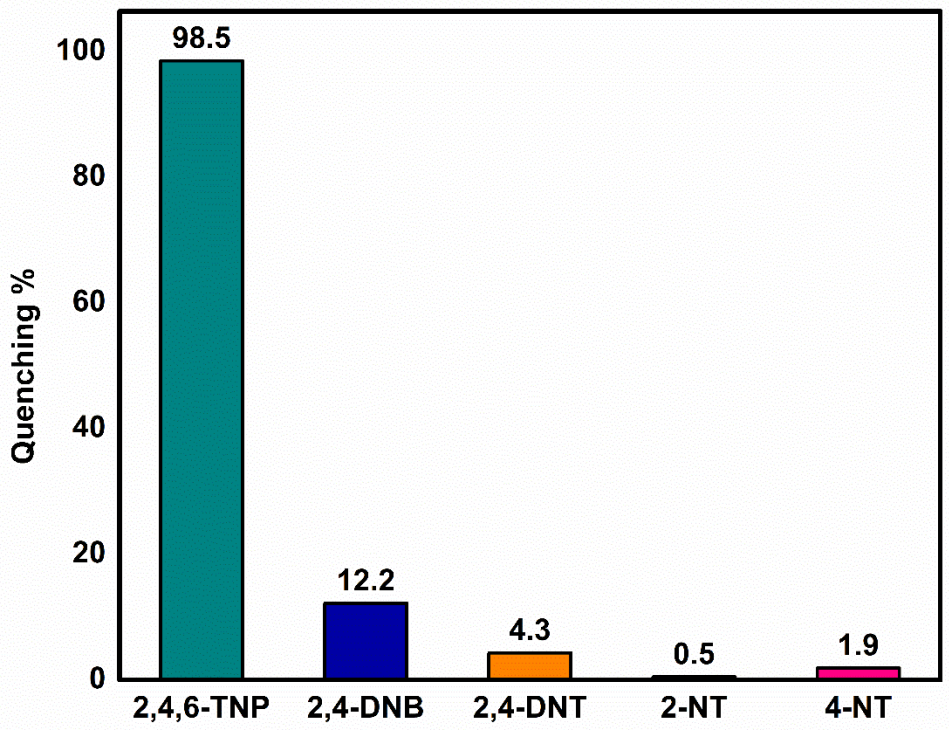

Figure 6.10. *Bar plot for the PL quenching (in %) of WS_2 QDs with different nitro explosive compounds in water.*

The selectivity test was conducted for the selective detection of TNP by performing titration experiments with several nitro explosive compounds like 2-nitrotoluene (2-NT), 4-nitrotoluene (4-NT), 2,4-dinitrobenzene (DNB) and 2,4-dinitrotoluene (DNT). The comparison between the PL % of quenching is shown in Fig. (6.10), which shows that the PL quenching by TNP is many times larger than other nitro explosives. Thus, WS_2 QDs could be an efficient probe sensing TNP selectively in water. Also, the interference of other nitro

explosives was tested in TNP sensing. For that, an equivalent concentration of other nitro compounds was added to QDs as the TNP. Then, the PL spectra of QDs were recorded in the presence of all the compounds. The bar graph (Fig. 6.11) showed the interference effect on the TNP sensing. The quenching percentage for all interference results is nearly the same because of the presence of TNP compound.

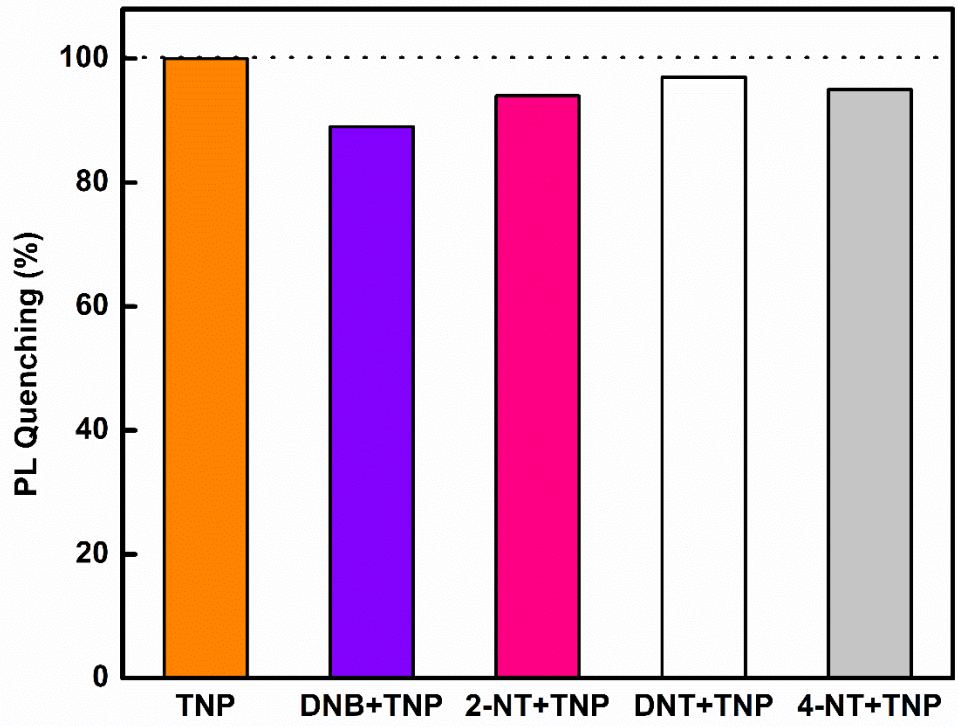

Figure 6.11. *Interference bar plot for the PL quenching (in %) of WS_2 QDs with different nitro explosive compounds at certain TNP concentrations.*

6.6. Conclusions

The WS_2 QDs were prepared through a novel facile hydrothermal technique. The prepared QDs were characterized through absorption spectroscopy to measure their optical bandgap energy. The UV-visible absorption spectrum showed a sharp absorption band at 288 nm whereas, the bandgap energy is calculated to be 3.6 eV with Tauc's plot. The PL and PL-excitation spectra were also measured for the synthesized WS_2 QDs. The absorption and

excitation spectrum of the QDs do not overlap because the PL of WS_2 QDs comprises different species that might originate from different ground states. The excitation-dependent PL occurred due to the evolution of electron-hole pairs at different energy levels, which took place due to the inhomogeneous distribution of the particle size in the aqueous medium and the surface functionalization of the WS_2 QDs.

The prepared QDs were employed for the detection of highly acidic and explosive compound 2,4,6-trinitrophenol. The QDs senses the TNP efficiently and selectively with a detection limit of 0.2 µM for the dynamic range of TNP concentration of 0.28-85 µM. We feel that the primary detection of a commonly used pollutant in the environment using QDs is quite significant for humanity.

References

[1] K. S. Novoselov, A.K. Geims, V. Morozov, D. Jiang, Y. Zhang, S.V. Dubonos, I. V. Grigorieva, A. A. Firsov, Electric field effect in atomically thin carbon films, Science. 306 (2004) 666–669.

[2] K. S. Novoselov, A.K. Geims, V. Morozov, D. Jiang, M. I. Katsnelson, I. V. Grigorieva, S. V. Dubonos, A. A. Firsov, Two-dimensional gas of massless Dirac fermions in graphene, Nature. 438 (2005) 197–200.

[3] A. Allain, J. Kang, K. Banerjee, A. Kis, Electrical contacts to two-dimensional semiconductors, Nat. Mater. 2015 1412. 14 (2015) 1195–1205.

[4] G. Fiori, F. Bonaccorso, G. Iannaccone, T. Palacios, D. Neumaier, A. Seabaugh, S.K. Banerjee, L. Colombo, Electronics based on two-dimensional materials, Nat. Nanotechnol. 2014 910. 9 (2014) 768–779.

[5] M. Xu, T. Liang, M. Shi, H. Chen, Graphene-like two-dimensional materials, Chem. Rev. 113 (2013) 3766–3798.

[6] S.Z. Butler, S.M. Hollen, L. Cao, Y. Cui, J.A. Gupta, H.R. Gutiérrez, T.F. Heinz, S.S. Hong, J. Huang, A.F. Ismach, E. Johnston-Halperin, M. Kuno, V. V. Plashnitsa, R.D. Robinson, R.S. Ruoff, S. Salahuddin, J. Shan, L. Shi, M.G. Spencer, M. Terrones, W. Windl, J.E. Goldberger, Progress, challenges, and opportunities in two-dimensional materials beyond graphene, ACS Nano. 7 (2013) 2898–2926.

[7] D. Golberg, Y. Bando, Y. Huang, T. Terao, M. Mitome, C. Tang, C. Zhi, Boron Nitride nanotubes and nanosheets, ACS Nano. 4 (2010) 2979–2993.

[8] C. M, S. HS, E. G, L. LJ, L. KP, Z. H, The chemistry of two-dimensional layered transition metal dichalcogenide nanosheets, Nat. Chem. 5 (2013) 263–275.

[9] A. Molina-Sánchez, L. Wirtz, Phonons in single-layer and few-layer MoS_2 and WS_2, Phys. Rev. B. 84 (2011) 155413.

[10] H.R. Gutiérrez, N. Perea-López, A.L. Elías, A. Berkdemir, B. Wang, R. Lv, F. López-Urías, V.H. Crespi, H. Terrones, M. Terrones, Extraordinary room-temperature photoluminescence in triangular WS_2 monolayers, Nano Lett. 13 (2012) 3447–3454.

[11] H. Jiang, Electronic band structures of molybdenum and tungsten dichalcogenides by the GW approach, J. Phys. Chem. C. 116 (2012) 7664–7671.

[12] L. Cheng, J. Liu, X. Gu, H. Gong, X. Shi, T. Liu, C. Wang, X. Wang, G. Liu, H. Xing, W. Bu, B. Sun, Z. Liu, PEGylated WS_2 nanosheets as a multifunctional theranostic agent for in vivo dual-modal CT/photoacoustic imaging guided photothermal therapy, Adv. Mater. 26 (2014) 1886–1893.

[13] S. Xu, D. Li, P. Wu, One-pot, facile, and versatile synthesis of monolayer MoS_2/WS_2 quantum dots as bioimaging probes and efficient electrocatalysts for hydrogen evolution reaction, Adv. Funct. Mater. 25 (2015) 1127–1136.

[14] S.A. Shah, X. Shen, M. Xie, G. Zhu, Z. Ji, H. Zhou, K. Xu, X. Yue, A. Yuan, J. Zhu, Y. Chen, Nickel@nitrogen-doped carbon@MoS_2 nanosheets: an efficient electrocatalyst for hydrogen evolution reaction, Small. 15 (2019) 1804545.

[15] H.S.S. Ramakrishna Matte, A. Gomathi, A.K. Manna, D.J. Late, R. Datta, S.K. Pati, C.N.R. Rao, MoS_2 and WS_2 analogues of graphene, Angew. Chemie - Int. Ed. 49 (2010) 4059–4062.

[16] Y. Cui, R. Xin, Z. Yu,Y. Pan, Z.Y. Ong, X. Wei, J. Wang, H. Na, et al., High-performance monolayer WS_2 field-effect transistors on high-κ dielectrics, Adv. Mater. 27 (2015) 5230–5234.

[17] Q. Zhang, H. Ying, X. Li, R. Xiang, Y. Zheng, H. Wang, J. Su, M. Xu, X. Zheng, S. Maruyama, X. Zhang, Controlled doping engineering in 2D MoS_2 crystals toward performance augmentation of optoelectronic devices, ACS Appl. Mater. Interfaces. 13 (2021) 31861–31869.

[18] P. Sharma, M.S. Mehata, Rapid sensing of lead metal ions in an aqueous medium by MoS_2 quantum dots fluorescence turn-off, Mater. Res. Bull. 131 (2020) 110978.

[19] Y. Yang, J. Cui, M. Zheng, C. Hu, S. Tan, Y. Xiao, Q. Yang, Y. Liu, One-step synthesis of amino-functionalized fluorescent carbon nanoparticles by hydrothermal carbonization of chitosan, Chem. Commun. 48 (2011) 380–382.

[20] Z.-C. Yang, M. Wang, A.M. Yong, S.Y. Wong, X.-H. Zhang, H. Tan, A.Y. Chang, X. Li, J. Wang, Intrinsically fluorescent carbon dots with tunable emission derived from hydrothermal treatment of glucose in the presence of monopotassium phosphate, Chem. Commun. 47 (2011) 11615–11617.

[21] D. Gopalakrishnan, D. Damien, M.M. Shaijumon, MoS_2 Quantum Dot-Interspersed Exfoliated MoS_2 Nanosheets, ACS Nano. 8 (2014) 5297–5303.

[22] V. Sharma, M.S. Mehata, Rapid optical sensor for recognition of explosive 2,4,6-TNP traces in water through fluorescent ZnSe quantum dots, Spectrochim. Acta Part A Mol. Biomol. Spectrosc. 260 (2021) 119937.

[23] V. Sharma, M.S. Mehata, Synthesis of photoactivated highly fluorescent Mn^{2+}-doped ZnSe quantum dots as effective lead sensor in drinking water, Mater. Res. Bull. 134 (2021) 111121.

[24] P. Sharma, M.S. Mehata, Colloidal MoS_2 quantum dots based optical sensor for detection of 2,4,6-TNP explosive in an aqueous medium, Opt. Mater. (Amst). 100 (2020) 109646.

[25] L. Lin, Y. Xu, S. Zhang, I.M. Ross, A.C.M. Ong, D.A. Allwood, Fabrication of luminescent monolayered tungsten dichalcogenides quantum dots with giant spin-valley coupling, ACS Nano. 7 (2013) 8214–8223.

[26] B.H. Kim, M.J. Hackett, J. Park, T. Hyeon, Synthesis, characterization, and application of ultrasmall nanoparticles, Chem. Mater. 26 (2013) 59–71.

[27] G. Konstantatos, I. Howard, A. Fischer, S. Hoogland, J. Clifford, E. Klem, L. Levina, E.H. Sargent, Ultrasensitive solution-cast quantum dot photodetectors, Nat. 2006 4427099. 442 (2006) 180–183.

[28] H. Liu, Q. Li, S. Zhang, R. Yin, X. Liu, Y. He, K. Dai, C. Shan, J. Guo, C. Liu, C. Shen, X. Wang, N. Wang, Z. Wang, R. Wei, Z. Guo, Electrically conductive polymer

composites for smart flexible strain sensors: a critical review, J. Mater. Chem. C. 6 (2018) 12121–12141.

[29] S. Velmurugan, T. C.-K. Yang, J. Ching Juan, J.N. Chen, Preparation of novel nanostructured $WO_3/CuMnO_2$ p-n heterojunction nanocomposite for photoelectrochemical detection of nitrofurazone, J. Colloid Interface Sci. 596 (2021) 108–118.

[30] S. Das, L. Ngashangva, P. Goswami, Carbon dots: an emerging smart material for analytical applications, Micromachines, 12 (2021) 84.

[31] N. Jiang, G. Li, W. Che, D. Zhu, Z. Su, M.R. Bryce, Polyurethane derivatives for highly sensitive and selective fluorescence detection of 2,4,6-trinitrophenol (TNP), J. Mater. Chem. C. 6 (2018) 11287–11291.

[32] Y. Ma, H. Li, S. Peng, L. Wang, Highly selective and sensitive fluorescent paper sensor for nitroaromatic explosive detection, Anal. Chem. 84 (2012) 8415–8421.

[33] S. Thapa, E. Hettiarachchi, D.A. Dickie, G. Rubasinghege, Y. Qin, A charge-separated diamondoid metal–organic framework, Chem. Commun. 54 (2018) 12654–12657.

[34] L. Lin, M. Rong, S. Lu, X. Song, Y. Zhong, J. Yan, Y. Wang, X. Chen, A facile synthesis of highly luminescent nitrogen-doped graphene quantum dots for the detection of 2,4,6-trinitrophenol in aqueous solution, Nanoscale. 7 (2015) 1872–1878.

[35] M. Dong, Y.W. Wang, A.J. Zhang, Y. Peng, Colorimetric and fluorescent chemosensors for the detection of 2,4,6-trinitrophenol and investigation of their co-crystal structures, Chem. Asian J. 8 (2013) 1321–1330.

[36] J.-W. Liu, Y.-M. Wang, L. Xu, L.-Y. Duan, H. Tang, R.-Q. Yu, J.-H. Jiang, Melanin-like nanoquencher on graphitic carbon nitride nanosheets for tyrosinase activity and inhibitor assay, Anal. Chem. 88 (2016) 8355–8358.

[37] Y. Wang, Y. Ni, Molybdenum disulfide quantum dots as a photoluminescence sensing platform for 2,4,6-trinitrophenol detection, Anal. Chem. 86 (2014) 7463–7470.

[38] M.K. Singh, M.S. Mehata, Phase-dependent optical and photocatalytic performance of synthesized titanium dioxide (TiO_2) nanoparticles, Optik (Stuttg). 193 (2019).

CHAPTER 7

Summary and Scope of Future Work

7.1. Summary

The objectives of the current thesis entitled "*Growth of molybdenum disulfide (MoS_2) nanostructures and their applications*" disclosed the structural, morphological, electrical, compositional and optical properties of MoS_2 nanostructures and discussed their utility for sensing and photocatalytic applications. The MoS_2 has gained a great attention because of its structural similarity with graphene [1]. The layers tuned bandgap of MoS_2 possesses magnificent optical and electronic properties which exhibit a wide range of applications, i.e., catalysis, transistors, batteries, photodetectors, gas sensing, and as well as optoelectronic devices [2-16]. When the layered MoS_2 nanosheets are reduced to the zero-dimensional (0D) quantum dots (QDs) then the entirely different photo-physical properties of MoS_2 arises because of its quantum confinement and edge effects [17–19]. MoS_2 QDs have been extensively studied due to its low toxicity, high stability, abundance availability and excellent optical properties. The production of novel and advance MoS_2 nanostructures, is the fundamental step towards their implications to the numerous applications in various divisions. This thesis holds synthesis of different MoS_2 nanostructures by adopting the facile hydrothermal route. The hydrothermal/solvothermal method to synthesize MoS_2 was opted, due to its ability to form nanostructures at high pressure and temperatures, ease in handling, uniform production of nanomaterials and high yield [20–22]. The MoS_2 nanosheets and their quantum dots were prepared by altering the size of the particles and confining them in one or all axis to explore their properties comprehensively. The optical properties of MoS_2

nanostructures (like absorption, photoluminescence and time-resolved photoluminescence) along with the different sensing and photocatalytic applications have also been discussed in detail.

7.2. Important findings of the research work

The MoS_2 nanostructures were hydrothermally synthesized and their constituent phase, phase purity and the crystallite size were analysed from the XRD and compared with the respective JCPDS files. The results were then confirmed by analysing HR-TEM images, for particle size and structure. The orderly patterned fringes confirmed the formation of crystalline structure of MoS_2. The optical investigations through UV-visible absorption spectroscopy, PL spectroscopy and FTIR spectroscopy had been carried out for the prepared nanostructures to recorded their optical performances.

The synthesized MoS_2 QDs were then employed to detect the very explosive compound, 2,4,6-trinitrophenol (TNP), which has greater explosive strength than the very well-known explosive, trinitrotoluene (TNT). The TNP or picric acid is very acidic in nature and has been used in various industries, whose waste can cause severe health-related issues and destroy the soil and water resources. The primary detection of TNP of concentration as low as 5 μM, could be recorded through this sensing probe.

The highest quantum yield (QY) of the prepared quantum dots i.e., 17% had been achieved among previously reported QDs through the same hydrothermal route. Then, the absorption and PL spectra were recorded of the MoS_2 QDs and used to detect the lead metal ions (Pb^{2+}) in water bodies. The Pb^{2+} ions can cause severe damage to the human brain and could be a preliminary cause of cancer. The detection of Pb^{2+} ions in water holds great significance for the sustainability of humanity. The detection of the Pb^{2+} ions was pursued the

greater sensitivity and larger selectivity among other metal ions in water. Therefore, certain experiments were carried out and the data has been represented wisely to demonstrate the MoS_2 QDs as an efficient Pb^{2+} ion sensor. The detection of Pb^{2+} of concentration as low as 50 μM is possible through this probe.

The synthesized nanosheets were then employed for the photodegradation of the organic pollutant, i.e., crystal violet (CV) dye in water. The photodegradation of CV dye was performed because of the bandgap of the nanosheets, which lies in the visible region and supports the environment by using the abundant solar energy for the decomposition of an organic pollutant. The presence of the CV dye in water is a severe threat to the environment and aquatic life. Therefore, its degradation holds great significance for the upliftment of a sustainable environment.

The other transition metal dichalcogenides were also synthesized. The synthesis and characterization of tungsten disulfide (WS_2) QDs were carried out. The bright blue fluorescence was observed when exposed to ultraviolet light (365 nm). The prepared QDs were then employed to detect the TNP compound in water. The sensitivity and selectivity of the WS_2 QDs based sensor were calculated. The primary detection of TNP of concentration as low as 0.2 μM, could be recorded through this sensing probe.

7.3. Future scope of the work

1. Preparation of modified MoS_2 nanosheets by doping or forming heterostructures to enhance its photo/electro-catalytic performance.
2. Implementation of the prepared MoS_2 nanosheets as an anode in Li-ion batteries.
3. Preparation of modified fluorescent TMD QDs with enhanced optical performances.
4. Electro-absorption/emission properties of the fluorescent TMD QDs.

References

[1] J.N. Coleman, M. Lotya, A. O'Neill, S.D. Bergin, P.J. King, U. Khan, K. Young, A. Gaucher, S. De, R.J. Smith, I. V. Shvets, S.K. Arora, G. Stanton, H.Y. Kim, K. Lee, G.T. Kim, G.S. Duesberg, T. Hallam, J.J. Boland, J.J. Wang, J.F. Donegan, J.C. Grunlan, G. Moriarty, A. Shmeliov, R.J. Nicholls, J.M. Perkins, E.M. Grieveson, K. Theuwissen, D.W. McComb, P.D. Nellist, V. Nicolosi, Two-dimensional nanosheets produced by liquid exfoliation of layered materials, Science 331 (2011) 568–571.

[2] H. Xie, B. Jiang, B. Liu, Q. Wang, J. Xu, F. Pan, An investigation on the tribological performances of the SiO_2/MoS_2 hybrid nanofluids for magnesium alloy-steel contacts, Nanoscale Res. Lett. 11 (2016) 329.

[3] Y. Chen, X. Wang, P. Wang, H. Huang, G. Wu, B. Tian, Z. Hong, Y. Wang, S. Sun, H. Shen, J. Wang, W. Hu, J. Sun, X. Meng, J. Chu, Optoelectronic properties of few-layer MoS_2 FET gated by ferroelectric relaxor polymer, ACS Appl. Mater. Interfaces. 8 (2016) 32083–32088.

[4] Y. Yoon, K. Ganapathi, S. Salahuddin, How good can monolayer MoS_2 transistors be?, Nano Lett. 11 (2011) 3768–3773.

[5] Y. Teng, H. Zhao, Z. Zhang, Z. Li, Q. Xia, Y. Zhang, L. Zhao, X. Du, Z. Du, P. Lv, K. Świerczek, MoS_2 nanosheets vertically grown on graphene sheets for lithium-ion battery anodes, ACS Nano. 10 (2016) 8526–8535.

[6] M.A. Bissett, I.A. Kinloch, R.A.W. Dryfe, Characterization of MoS_2-graphene composites for high-performance coin cell supercapacitors, ACS Appl. Mater. Interfaces. 7 (2015) 17388–17398.

[7] M. Park, Y.J. Park, X. Chen, Y.-K. Park, M.-S. Kim, J.-H. Ahn, MoS_2 -based tactile sensor for electronic skin applications, Adv. Mater. 28 (2016) 2556–2562.

[8] C. Ataca, S. Ciraci, Dissociation of H_2O at the vacancies of single-layer MoS_2, Phys. Rev. B - Condens. Matter Mater. Phys. 85 (2012) 195410.

[9] X. Yang, J. Li, T. Liang, C. Ma, Y. Zhang, H. Chen, N. Hanagata, H. Su, M. Xu, Antibacterial activity of two-dimensional MoS_2 sheets, Nanoscale. 6 (2014) 10126–10133.

[10] J. Yu, X. Ma, W. Yin, Z. Gu, Synthesis of PVP-functionalized ultra-small MoS_2 nanoparticles with intrinsic peroxidase-like activity for H_2O_2 and glucose detection, RSC Adv. 6 (2016) 81174–81181.

[11] D. Voiry, M. Salehi, R. Silva, T. Fujita, M. Chen, T. Asefa, V.B. Shenoy, G. Eda, M. Chhowalla, Conducting MoS_2 nanosheets as catalysts for hydrogen evolution reaction, Nano Lett. 13 (2013) 6222–6227.

[12] J. Kibsgaard, Z. Chen, B.N. Reinecke, T.F. Jaramillo, Engineering the surface structure of MoS_2 to preferentially expose active edge sites for electrocatalysis, Nat. Mater. 11 (2012) 963–969.

[13] X. Zong, H. Yan, G. Wu, G. Ma, F. Wen, L. Wang, C. Li, Enhancement of

photocatalytic H_2 evolution on CdS by loading MoS_2 as cocatalyst under visible light irradiation, J. Am. Chem. Soc. 130 (2008) 7176–7177.

[14] B.L. Li, M.I. Setyawati, L. Chen, J. Xie, K. Ariga, C.T. Lim, S. Garaj, D.T. Leong, Directing assembly and disassembly of 2D MoS_2 Nanosheets with DNA for drug delivery, ACS Appl. Mater. Interfaces. 9 (2017) 15286–15296.

[15] L. Chen, Y. Feng, X. Zhou, Q. Zhang, W. Nie, W. Wang, Y. Zhang, C. He, One-Pot synthesis of MoS_2 nanoflakes with desirable degradability for photothermal cancer therapy, ACS Appl. Mater. Interfaces. 9 (2017) 17347–17358.

[16] M. Bruchez, M. Moronne, P. Gin, S. Weiss, A.P. Alivisatos, Semiconductor nanocrystals as fluorescent biological labels, Science. 281 (1998) 2013–2016.

[17] J. Li, J.J. Zhu, Quantum dots for fluorescent biosensing and bio-imaging applications, Analyst. 138 (2013) 2506–2515.

[18] H.D. Ha, D.J. Han, J.S. Choi, M. Park, T.S. Seo, Dual role of blue luminescent MoS_2 quantum dots in fluorescence resonance energy transfer phenomenon, Small. 10 (2014) 3858–3862.

[19] G.U. Siddiqui, J. Ali, K.H. Choi, Y. Jang, K. Lee, Fabrication of blue luminescent MoS_2 quantum dots by wet grinding assisted co-solvent sonication, J. Lumin. 169 (2016) 342–347.

[20] S. Feng, R. Xu, New materials in hydrothermal synthesis, Acc. Chem. Res. 34 (2001) 239–247.

[21] W. Shi, S. Song, H. Zhang, Hydrothermal synthetic strategies of inorganic semiconducting nanostructures, Chem. Soc. Rev. 42 (2013) 5714–5743.

[22] R.L. Penn, J.F. Banfield, Morphology development and crystal growth in nanocrystalline aggregates under hydrothermal conditions: Insights from titania, Geochim. Cosmochim. Acta. 63 (1999) 1549–1557.